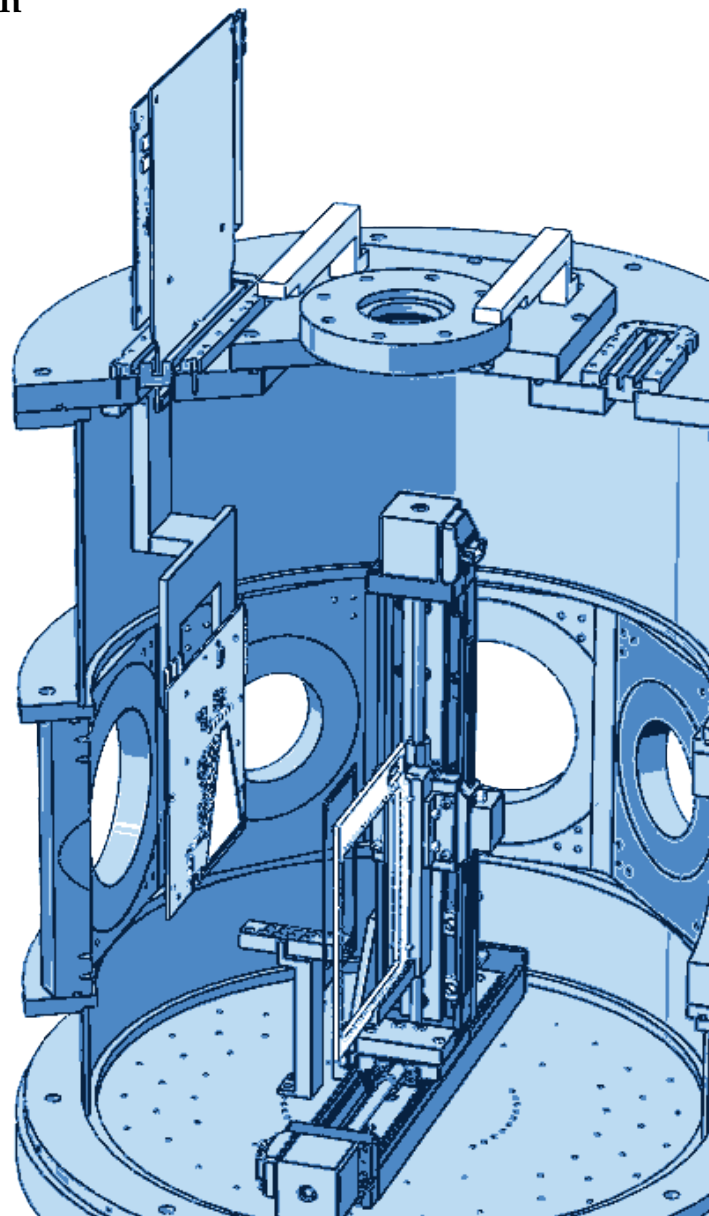# Position Resolved Neutron Depth Profiling with the N4DP Instrument

Robert Neagu

Dissertation

TUM

TECHNISCHE UNIVERSITÄT MÜNCHEN

TUM School of Natural Sciences

Position Resolved Neutron Depth Profiling with the N4DP Instrument

Robert Neagu

Vollständiger Abdruck der von der TUM School of Natural Sciences der Technischen Universität München zur Erlangung eines

Doktors der Naturwissenschaften (Dr. rer. nat.) genehmigten

Dissertation.

Vorsitz:	Prof. Dr. Björn Garbrecht
Prüfende der Dissertation:	1. Prof. Dr. Bastian Märkisch
	2. Prof. Dr. Susanne Mertens

Die Dissertation wurde am 04.11.2024 bei der Technischen Universität München eingereicht und durch die TUM School of Natural Sciences am 02.12.2024 angenommen.

Zusammenfassung

Die Neutronen-Tiefenprofilanalyse (engl. neutron depth profiling - NDP) ist eine nuklearanalytische Methode zur hochpräzisen Bestimmung von Konzentrationsprofilen bestimmter Nuklide in oberflächennahen Schichten. Die Methode basiert auf der Neutroneneinfangreaktion mit darauffolgender Emission geladener Teilchen bekannter kinetischer Energie. Aus deren Energieverlust und Entstehungsrate lassen sich die Konzentrationsprofile der Mutterisotope bestimmen. Lithium und Bor sind zwei der NDP-spezifischen Elemente, die aufgrund ihrer Verwendung bei der Entwicklung neuartiger Materialien von großem Forschungsinteresse sind. Beispielsweise ist es von großem Interesse, die Bewegung der Li-Wolke während der (Ent-)Ladung in Li-Ionen-Batterien mit hoher Genauigkeit zu beobachten. Inhomogenitäten in solchen elektrochemischen Prozessen erfordern eine gute räumliche Auflösung, um das Li in der Batterie zu lokalisieren.

Das N4DP-Instrument am FRM II-Forschungsreaktor in Garching, Deutschland, verwendet einen kalten Neutronenstrahl mit einem Fluss von bis zu $5 \times 10^{10}\,\mathrm{cm}^{-2}\mathrm{s}^{-1}$. Um eine optimale Tiefenauflösung zu erreichen, müssen besonders rauscharme Detektoren und Elektronik eingesetzt werden. Für die NDP wurden bisher fast ausschließlich unsegmentierte Detektoren auf Si-Basis, z.B. Oberflächensperrschichtdetektoren, verwendet. Um dieses Verfahren auf eine 3D-Profilierung zu erweitern, wurde ein Detektorsystem basierend auf doppelseitigen Silizium-Streifen-Detektoren (DSSSD) mit einer ultradünnen und homogenen Totschicht entwickelt und charakterisiert. Die Kombination der ortssensitiven Detektoren mit einer maßgeschneiderten, auf anwendungsspezifischen integrierten Schaltkreisen (ASIC) basierenden Elektronik ermöglicht die Profilerstellung in 3+1 Dimensionen bei höchsten Raten.

In dieser Arbeit wird ein solches 3+1D-System für das N4DP-Instrument als weltweit einzigartige Instrumentierung vorgestellt. Ein hochsegmentierter DSSSD mit 32×266-Streifen, wurde zunächst serienreif entwickelt, in großen Stückzahlen gefertigt und in maßgeschneiderten Hybridleiterplatten mit integrierter selbsttriggernder Elektronik für den Vakuumbetrieb eingesetzt. Die Detektoren bilden zusammen mit der SKIROC-basierten Elektronik vollständige Frontend-Detektormodule, die für die Aufrüstung des N4DP-Instruments zur hochauflösenden vierdimensionalen Profilanalyse zur Verfügung stehen.

Die Detektormodule wurden im Labor mittels künstlich erzeugten Signalen und einer α-Quelle erfolgreich erprobt und die Totschichten der einzelnen Detektoren mit hoher Präzision charakterisiert. Parallel dazu wurde auch die Analysesoftware für die automatische Kalibrierung aller 160-Kanäle entwickelt, so dass eine einzige Messung für eine vollständige Kalibration ausreicht. Die Detektormodule wurden zusammen mit einem Synchronisationsboard zu einem Multidetektorsystem weiterentwickelt und erstmals in einem Proton-Proton Streuexperiment auf Koinzidenz getestet. Dabei zeigte sich, dass die energieabhängige Effizienz des Systems stark von den Parametern der Elektronik und den Teilchenraten abhängt.

In einem NDP-Experiment am Reactor Institute Delft (RID) wurde unter Verwendung eines Dualdetektoraufbaus in einer *Camera obscura*-Geometrie die Abbildung und Rekonstruktion von Li-haltigen Targets über einen weiten Parameterbereich erreicht, d.h. von einer räumlichen Auflösung bis hinunter zu $\sim 100\,\mu\text{m} \times 200\,\mu\text{m}$ und einer Bildwiederholrate in der Größenordnung von Sekunden, mit ausreichender Statistik zur Überwachung lokaler Variationen der Li-Konzentration. Hierbei konnte durch Optimierung in der Ansteuerung der rauscharmen Elektronik und sorgfältige Filterung der erfassten Korrelationsdaten ein nahezu untergrundfreies Signal selektiert werden. Die wichtigsten Ergebnisse dieser Studie wurden in einer wissenschaftlichen Veröffentlichung zusammengefasst.

Abstract

Neutron depth profiling (NDP) is a nuclear analytical method for the high-precision determination of concentration profiles of specific nuclides in near-surface layers. The method is based on the neutron capture reaction with a subsequent emission of charged particles of well-defined kinetic energy. The concentration profiles of the parent isotopes can be determined from their energy loss and formation rate. Lithium and boron are two NDP-specific nuclides that are of great research interest due to their influence in the development of novel materials. For example, it is of great interest to observe the movement of the Li cloud during (dis-)charging in Li-ion batteries with high precision. Inhomogeneities in such electrochemical processes require good spatial resolution to localize the Li in the battery.

The N4DP instrument at the FRM II research reactor in Garching, Germany, uses a cold neutron beam with a flux of up to $5 \times 10^{10}\,\mathrm{cm^{-2}s^{-1}}$. In order to achieve optimum depth resolution, particularly low-noise detectors and electronics must be used. So far, almost exclusively unsegmented Si-based detectors, *e.g.* surface barrier detectors, have been used for NDP. In order to extend this method to 3D profiling, a detector system based on double-sided silicon strip detectors (DSSSD) with an ultra-thin and homogeneous dead layer was developed and characterized. The combination of the position-sensitive detectors with customized electronics based on application-specific integrated circuits (ASIC) enables profiling in 3+1 dimensions at the highest rates.

This work presents such a 3+1D system for the N4DP instrument as a globally unique instrumentation. A highly segmented DSSSD with 32×266 strips was initially developed ready for series production, manufactured in large quantities, and implemented in customized hybrid printed circuit boards with integrated self-triggering electronics for vacuum operation. Together with the SKIROC-based electronics, the detectors form complete front-end detector modules that are available for upgrading the N4DP instrument to a high-resolution four-dimensional profile analysis instrument.

The detector modules were successfully tested in the laboratory using artificially generated signals and an α source, and the dead layers of the individual detectors were characterized with high precision. At the same time, the analysis software for the automatic calibration of all 160 channels was developed so that a single measurement is sufficient for a complete calibration. Together with a synchronization board, the detector modules were used to create a multi-detector system, which was tested for coincidence for the first time in a proton-proton scattering experiment. This experiment showed that the energy-dependent efficiency of the system is strongly dependent on the parameters of the electronics and the particle rates.

In an NDP experiment at the Reactor Institute Delft (RID), the imaging and reconstruction of Li-containing targets was achieved over a wide parameter range using a dual detector setup in a *camera obscura*-geometry, *i.e.* from a spatial resolution down to $\sim 100\,\mu\mathrm{m} \times 200\,\mu\mathrm{m}$ and a frame rate in the order of seconds, with sufficient statistics to monitor local variations in Li concentration. By optimizing the control of the low-noise

electronics and carefully filtering the acquired correlation data, it was possible to select an almost background-free signal. The most important results of this study were summarised in a scientific publication.

Contents

Acronyms

AC	Alternating/capacitive Coupling.
ADC	Analog-to-Digital Converter.
ASIC	Application Specific Integrated Circuit.
COG	Center Of Gravity.
CoMPASS	CAEN Multi-PArameter Spectroscopy Software.
DAQ	Data AcQuisition.
DC	Direct Coupling.
DHCP	Dynamic Host Configuration Protocol.
DPP	Digital Pulse Processing.
DSSSD	Double Sided Silicon Strip Detector.
EMCAL	Electro Magnetic CALorimeter.
ENC	Equivalent Noise Charge.
FAIR	Facility for Antiproton and Ion Research.
FFC	Flexible Flat Cables.
FPGA	Field Programmable Gate Array.
FRM II	Forschungs-Neutronenquelle Heinz Maier-Leibnitz.
FWHM	Full Width at Half Maximum.
GEAR	GEneric Asic Readout.
HADES	High Acceptance DiElectron Spectrometer.
HV	High Voltage.
ILC	International Linear Collider.
LHC	Large Hadron Collider.
MARaBOU	MBS And ROOT Based Online/Offline Utility.
MBS	Multi Branch System.
MC	Monte-Carlo.
N4DP	Neutron Four Depth Profiling.
NAA	Neutron Activation Analysis.
NDP	Neutron Depth Profiling.
NIM	Nuclear Instrumentation Module.

NPD   Neutron Powder Diffraction.

PCB   Printed Circuit Board.
PGAA   Prompt Gamma Activation Analysis.
PGAI-NT   Prompt Gamma-ray Activation Imaging and Neutron Tomography.
PHA   Pulse Height Analysis.

QFS   Quasi-Free-Scattering.

R&D   Research and Development.
RID   Reactor Institute Delft.
RTA   Rapid Thermal Annealing.

SANS   Small-Angle Neutron Scattering.
SCA   Switching Capacitor Array.
SEI   Solid Electrolyte Interphase.
SIMS   Secondary-Ion Mass Spectrometry.
SKIROC   Silicon Kalorimeter Integrated ReadOut Chip.
SMD   Surface Mounted Devices.
SNR   Signal-to-Noise Ratio.
SRIM   Stopping and Range of Ions in Matter.
SSB   Silicon Surface Barrier.
SVD   Singular Value Decomposition.

TAC   Time-to-Amplitude Converter.
TDC   Time-to-Digital Converter.
ToA   Time-of-Arrival.
TOF   Time-Of-Flight.
ToT   Time-over-Threshold.
TREX   Transfer Reactions EXperiments.

UDP   User Datagram Protocol.

VME   Versa Module Europa.

ZTL   Zentrales Technologie Labor.

Introduction

Equipped with our five senses, along with telescopes and microscopes and mass spectrometers and seismographs and magnetometers and particle accelerators and detectors across the electromagnetic spectrum, we explore the universe around us and call the adventure science. - Neil DeGrasse Tyson's respectful update of a quote by Edwin P. Hubble in 1954.

The commercialization of the lithium-ion battery in the early 1990s has revolutionized many areas of our lives [1]. Thanks to its extremely high efficiency and high energy density, it enables electromobility and is crucial for consumer electronics, such as mobile and medical applications [2]. Especially for electric cars, lithium-ion batteries are interesting due to their high efficiency. Compared to the battery of an electric car, fuel cells require around three times as much primary energy for the same distance, e-fuels even five times as much [3, 4]. In order to obtain an electrically useful voltage in a battery, a potential difference is created between two electrodes, the anode and the cathode. By closing the battery with an external circuit, the ions move from one electrode to the other, allowing for electrons to flow in the external circuit. In lithium-ion batteries, lithium ions play this role. In neutron science, especially in Neutron Depth Profiling (NDP), ^{6}Li, with its high abundance of $\sim 7.6\%$ in natural lithium, has a very high cross section for thermal neutron capture. This unique property makes the element highly visible, especially when using colder neutron beams, which allows for neutron facilities with high fluxes to study any dynamic processes within such battery systems. Especially the anode material of the lithium-ion battery offers considerable potential for optimization with regard to the capacity, weight, and performance [5]. Graphite is the standard for the anode material that enables lithium to be deposited in the interlayers of the carbon lattice - a process known as intercalation. The specific capacity of batteries with graphite-based anode materials is roughly one order of magnitude lower when compared with other anode materials such as Si or pure Li [6]. A great advantage of graphite is that its structure changes only slightly during the intercalation (roughly 10% expansion), whereas for Si, the expansion is roughly 300% [7]. Between the two electrodes, there is the electrolyte, which allows the transport of lithium between them. The initial cycle of a battery plays an important role since a very thin (in the order of nanometers) interphase between the anode and electrolyte, the so-called Solid Electrolyte Interphase (SEI), is formed. It is due to this SEI that the operation of lithium-ion batteries is possible in the first place since it slows down the degrading of the electrolyte by reducing the electron transport through the interphase [8]. At the same time, due to the large area of the anode, the SEI also leads to a considerable loss of usable lithium and, therefore, capacity loss. Many of these dynamic processes are

not yet fully understood and can be studied using NDP.

The main focus of this thesis is the development, implementation, and characterization of highly segmented silicon detectors to resolve bulk element distributions, such as lithium, in three spatial and one temporal dimensions using the NDP technique. In this chapter, we first discuss some of the methods used to determine material properties, such as neutron-based experiments. We then motivate the implementation of position-resolving detectors in NDP-type experiments based on open questions in different research fields, highlighting already established methods of this technique and some limitations. Then, we lay down all the parameters needed to be optimized in a detector system to achieve the best possible NDP instrument. Finally, at the end of this chapter, we introduce the structure of the thesis.

1.1   Spectroscopic Quality Measurements of Particle Energies

Since their first postulation in 1920 by Ernest Rutherford [9] and their first discovery in 1932 by the physicist James Chadwick [10] (which led to a Nobel Prize in 1935), neutrons have become increasingly popular for various research purposes due to their magnetic properties. Their high penetration, nuclide-specific sensitivity, and non-destructive nature allow samples to be characterized in a unique way, complementing other techniques such as X-ray-based methods [11, 12] and Secondary-Ion Mass Spectrometry (SIMS) [13, 14]. Some of the neutron sensitive methods are mentioned in the following: the Neutron Powder Diffraction (NPD) method exploits the wave nature of neutrons, using neutron scattering to determine the atomic and magnetic structure of a material [15]. The Small-Angle Neutron Scattering (SANS) technique allows the study and quantification of dynamic structural changes in bulk materials [16], while neutron reflectometry allows kinematic studies at near-surface levels [17, 18]. Inelastic neutron scattering experiments, such as Time-Of-Flight (TOF), triple-axis spectroscopy, and spin-echo, are commonly used to study motion and field excitations at the atomic and molecular levels [19]. Other applications of neutrons are tomography and radiography, which allow non-destructive imaging of large objects [20], Neutron Activation Analysis (NAA), which is used to determine element concentrations with high sensitivity (down to ppb) [21], and neutron depth profiling, which is mainly used to determine depth profiles of certain elements [22]. The latter, NDP, has the great advantage of being non-destructive, allowing for *operando* type measurements.

1.2   Motivation for 4D NDP Experiments

One of the most interesting applications for the NDP method is the study of lithium distribution in battery systems, see *e.g.* [23–26]. The method allows for quantitative analysis of Li homogeneity over the depth of the batteries. However, the intercalation of lithium in newly developed electrode materials and the characterization of the interphases between the electrolyte and the electrode, the SEI, require new detection systems to provide information on their lateral, depth, and temporal variation.

To resolve the lithium in such a thin battery system laterally, one can use a narrow, collimated neutron beam and a pinhole aperture to scan the surface, as shown in [27]. This type of measurement requires long data collection times from each sample point to

obtain a meaningful volume profile. Position-sensitive detectors can be used to reduce this to a single measurement.

High-resolution 2D visualization can be achieved using multi-pixel detectors arranged in a tight sandwich geometry, as shown by Tomandl *et al.* [28]. In this setup, the image is reconstructed from the back-to-back reactions. However, the compact geometry also exposes the sensors to the neutron beam, which damages them over time and introduces significant background noise, especially at higher neutron fluxes. Lichtinger *et al.* [29], and others [30, 31] have shown that position-sensitive NDP measurements can be performed using commercially available monolithic position-sensitive diodes [32]. However, due to pile-up effects and slow detector response, these detectors are not suitable for the high rates required for *operando* measurements, such as those involving battery charging and discharging during the measurement process [33].

1.3   Detector Parameters

All neutron experiments are highly dependent on the individual properties of the detection system and the sample environment, as these determine the accuracy and sensitivity of the measurements. Especially in NDP, the detector system is the most crucial part of the method. The energy resolution of a detector is closely related to the depth resolution, so a higher energy resolution allows for a more accurate determination of element concentrations at varying depths. To achieve high 2D spatial resolution, the detector segmentation must be optimized, as its granularity directly influences the resolution. Furthermore, the efficiency or acceptance of the detector system plays a critical role, as it influences the concentration limits that can be measured, as well as the temporal resolution that can be achieved in dynamic studies. At the same time, these detectors must be able to cope with higher reaction rates and withstand certain irradiation levels. Such developments are particularly needed for large experimental facilities such as the Large Hadron Collider (LHC) experiments [34] and Facility for Antiproton and Ion Research (FAIR) [35]. In this thesis, we present detectors used in NDP-type experiments, where ions with energies up to 3 MeV are detected with high spectroscopic energy resolution to extract the depth information of NDP-specific neutron capture reactions. The main objective of this work was to develop a detector system with depth sensitivity close to the achievable limits, as well as position sensitivity with low background influence. The advantage of NDP is that low-energy charged particles undergo a large specific energy loss in the matter, but it also massively limits the method by the environment. Therefore, the system must be operated under vacuum conditions, with as little surrounding material as possible. This also imposes a constraint on the electronics, which must be operated close to the detector in the vacuum. The high granularity of a segmented detector means that many electronic channels are needed, which can lead to high power consumption and also heat dissipation, potentially compromising the resolution. Therefore, the selection of suitable electronics for such applications is of great interest.

There are several NDP instruments worldwide, of which the Munich N4DP system (N4DP - Neutron Four Depth Profiling) makes use of the highest cold neutron flux densities (see Tab. 1.1). This high flux enables the best conditions for time-resolved

measurements of dynamic systems. A certain number of events must be collected to obtain a statistically significant depth profile. These instruments typically use Silicon Surface Barrier (SSB) or similarly designed detectors to determine depth profiles. The main characteristics of a well-designed neutron depth profiling detector must be adapted to the detection of charged particles such as protons, α particles, and tritons. Since these ions lose more energy in thin layers than β and γ particles, high-resolution detectors for these applications require thin and very homogeneous dead layers [22]. A thin dead layer is favorable for detecting ions, as shown in [22, 36, 37]. Furthermore, to avoid β at low energies (below 500 keV), it is important to keep the active thickness of the detectors as small as possible. Berner *et al.* [38] show the importance of this layer thickness and the contribution of the β particles at different thicknesses, recommending thinner bulks for lower backgrounds.

Table 1.1.: List of NDP instruments worldwide. These instruments are sorted by their thermal equivalent neutron flux density.

Instrument / Institution	Location	Neutron Flux Density [$\frac{1}{cm^2s}$]	Reference
N4DP / TUM, MLZ	Garching, Germany	5×10^{10}	[36]
NIST NCNR	Gaithersburg, USA	1.2×10^9	[22]
MARIA / JCNS, MLZ	Garching, Germany	0.7×10^9	[39]
CARR	Beijing, China	4.8×10^8	[40]
KAERI / HANARO	Daejeon, Korea	1.8×10^8	[41]
RID	Delft, Netherlands	1.0×10^7	[26]

In 1981, Biersack *et al.* [37] were one of the first ones to use segmented detectors to measure the position and depth of light elements, such as lithium, by means of (n, α) reactions. They used two position-sensitive detectors from Philips[1] [42] with thicknesses of 300 μm, and even then, they understood the disadvantage of the large depletion depth of the detectors in picking up background radiation.

While standard depth profiling is a very well-established method, volume profiling at high count rates (4D) still requires some development. By using modern Si wafer processing technologies, it is possible to create a detector system capable of detecting low-energy charged particles with high-quality measurement parameters such as energy, position, and time. A detector with a thin and homogeneous entrance window, in combination with close-by low-noise electronics with high acceptance, allows us to achieve such a goal.

1.4 Thesis Organization

Within the scope of this thesis, major developments of the N4DP instrument were achieved, including the development of a new detector, allowing for a new state-of-the-art four-dimensional neutron depth profiling.

---

[1]Philips "Checkerboard" BPY 75-300

In Chap. 2, we lay the necessary theoretical groundwork for neutron-based reactions as well as for the detection of ions using silicon detectors, and finally review some methods that can be used for 3D profiling. In Chap. 3, we present the newly developed silicon detector with its electronics. In Chap. 4, the N4DP instrument and its upgrade with the developed detector board are reviewed. The first characterizations of the detectors and the development of the multi-detector correlation are described in Chap. 5. An actual ^{6}Li neutron-induced NDP reaction experiment is then described in Chap. 6, which was performed at the Reactor Institute in Delft. Here, we benchmark our detector, considering its capabilities in all four dimensions. Finally, in Chap. 7 we present a summary and an outlook for future work.

Methodology

This chapter covers the methodological foundations of neutron depth profiling. In Sec. 2.1, the principles of neutron capture are explained, including its mechanisms and importance in neutron-based experiments, especially in NDP. Then the energy loss of ions in matter is reviewed, which is crucial for understanding the depth profiles obtained in NDP. In Sec. 2.2, we provide an overview of some of the existing detector technologies, highlighting their function, capabilities, and limitations that necessitate further developments in the field. Then, Sec. 2.3 covers two main 2D imaging methods. The implementation of these methods into the N4DP instrument is described at the end of Chap. 4, while the first results and discussion from using these methods in an NDP experiment are presented in Chap. 6.

2.1 Principles of Neutron Depth Profiling

NDP is a non-destructive nuclear analytical technique for determining the concentration profile of specific elements in various substrates in the near-surface layer [22]. Neutron-induced particles lose energy as they pass through matter. The energy loss can be correlated to the emission depth. NDP was invented in 1972 by Ziegler *et al.* to determine low amounts (ppm) of boron particles in silicon substrates [43, 44] and has gained popularity in recent years due to its application in the study of Li-containing samples such as Li-ion batteries [24, 25, 33, 45–48].

2.1.1 Neutron Capture

When a specific nuclide ^{A}Z with energy levels near or above the vacuum level interacts with neutrons of certain energies (thermal or sub-thermal), it can capture these neutrons, resulting in the formation of a highly excited compound nucleus, which we denote as $^{A+1}$Z*. This nucleus can then de-excite by emitting prompt gamma rays, charged particles, or both. The energies of the emitted gamma rays are characteristic and form the basis of Prompt Gamma Activation Analysis (PGAA) [49]. The probability for a particular neutron-caption reaction is defined by the microscopic neutron capture cross section σ [50]. For neutron depth profiling, we are interested in the neutron capture reaction with the subsequent emission of two monoenergetic charged particles. The few stable, typically light nuclides that exhibit this property are listed in Tab. 2.1. Due to their high cross section, natural isotopic abundance, and application potentials in material science, ^{6}Li, and ^{10}B are the most studied nuclides in NDP. The de-exitation of ^{10}B* is followed by emission of a 477.59 keV γ-ray. There are also some radioactive nuclides such as ^{7}Be, ^{22}Na, ^{37}Ar, and ^{59}Ni with high cross sections, which could be detectable in NDP.

Table 2.1.: Stable isotopes with charged-particle emission after neutron capture. Data obtained from [51].

Isotope	Reaction	σ_{th} [barns]	Natural Isotopic Abundance [%]	Recoil Mass Energy [keV]	Emitted Particle Energy [keV]
^{3}He	$(n,^1H)^3H$	5322.73	0.00013	191.29	572.46
^{6}Li	$(n,^3H)^4He$	939.09	7.59	2055.55	2727.92
^{10}B*	$(n,^4He)^7Li$	3600.53	18.65	839.97	1472.35
^{10}B	$(n,^4He)^7Li$	241.32	1.25	1013.46	1776.45
^{14}N	$(n,^1H)^{14}C$	1.86	99.64	42.02	583.85
^{17}O	$(n,^4He)^{14}C$	0.24	0.038	404.07	1413.67
^{33}S	$(n,^4He)^{30}Si$	0.18	0.75	411.55	3081.95
^{35}Cl	$(n,^1H)^{35}S$	0.48	75.76	17.23	597.80
^{40}K	$(n,^1H)^{40}Ar$	4.33	0.012	56.25	2230.50

For neutrons at energies below resonance levels (below epithermal regions - few eV to keV), the neutron capture cross section follows the $1/v$ law or as a function of energy [52]:

$$\sigma(E) = \sigma_{th}\sqrt{\frac{E_{th}}{E}}, \tag{2.1}$$

where $E_{th} = k_B T \approx 25\,\text{meV}$ is the average kinetic energy of thermal neutrons. The N4DP instrument uses a white cold beam with an average energy of $E = 1.83\,\text{meV}$ [53], resulting in an increase in the neutron capture cross section of a factor of approximately 3.7 compared to a thermal neutron beam.

In neutron depth profiling, we usually want to know how many particles hit a detector in unit time. The detector count rate R is given by

$$R = N \cdot \Phi_c \cdot \sigma_{th} \cdot \epsilon, \tag{2.2}$$

where Φ_c is the thermal equivalent neutron flux (also "capture" flux), σ_{th} is the thermal cross section of the reaction, N is the number of target nuclides, and $\epsilon \approx \frac{\Omega_d}{4\pi r^2}\epsilon_d$ is the efficiency, which depends on the solid angle Ω_d covered by the detector, its distance r to the target and its detection efficiency ϵ_d (which can be regarded as ≈ 1 for solid-state detectors [54]).

At low energies ($\lesssim 200\,\text{keV}$), the particle energy deposited in the detectors usually overlaps with the electronic noise, making it nearly impossible to detect useful counts. This reduces the maximum depth from which particles can be identified. To avoid the disturbance from the huge baseline, an electronic threshold needs to be set above this level (in many measurements, it was set to $300\,\text{keV}$). For a known density ρ of a sample, we can calculate the number of target atoms N:

$$N = \rho \cdot d \cdot A, \tag{2.3}$$

with d being the thickness of the sample and A the irradiated area.

Mass Thickness

A commonly used metric to express the thickness of absorber materials is known as surface density or mass thickness (in an electrochemical context, this is sometimes called mass loading). It is given by:

$$m_{\text{area}} = \rho \cdot d \, , \tag{2.4}$$

where ρ is the mass density and d is the thickness, and yields the dimensions of mass per area, *e.g.* $[m_{\text{area}}] = \frac{\text{g}}{\text{cm}^2}$. When discussing the interaction of radiation in matter, units of mass thickness are shown to be more practical than length units since they are more related to the frequency of interaction points within the material, making it easier to compare materials with various mass densities [55].

2.1.2   Energy Loss of Charged Particles in Matter

The mean free path of neutrons in the sample is typically shorter than that for charged particles. Hence, the sample in the examined depth can be regarded as uniformly exposed to neutrons. Once a neutron is captured, the emitted charged particles travel through the sample in (nearly) straight paths, losing energy mainly through inelastic collisions with the electrons and atoms, leading to ionization and excitation. We can describe this energy loss as the stopping power $S(E)$, given in energy loss per unit length (usually in the order of $\frac{\text{keV}}{\mu\text{m}}$):

$$S(E) = -\frac{\text{d}E}{\text{d}x}\Big|_{\text{e,n}} , \tag{2.5}$$

where $\text{d}E$ is the energy loss while passing the pathlength $\text{d}x$ from the electronic (index e) and nuclear (index n) interactions. The electronic stopping power is more significant for light particles (low z) at high energies (in the keV range). It corresponds to many collisions of the charged particle with relatively small energy losses per collision (on the level of eV) and minimal changes in direction, resulting in a mostly straight trajectory [56]. At lower particle energies (low-to-sub keV range) and for particles of high atomic number Z, the nuclear scattering becomes dominant, leading to notable changes in the trajectory of the particle and to significant discrete energy losses [57]. In the typical energy range of NDP, the electronic stopping power is dominant.
Empirically, in the region $0.1 \lesssim \beta\gamma \lesssim 1000$, where $\beta = v/c$ (with v the velocity of the particle and c speed of light) and γ is the Lorentz factor, the mean electronic stopping power can be described by the Bethe-Bloch formula [56–59]:

$$-\left\langle \frac{\text{d}E}{\text{d}x} \right\rangle\Big|_{\text{e}} = \frac{4\pi e^4}{m_{\text{e}}c^2} \cdot n_{\text{e}} \cdot \frac{z^2}{\beta^2} \left[\ln\left(\frac{2m_{\text{e}}c^2\beta^2}{I(1-\beta^2)} \right) - \beta^2 - \frac{C}{Z} - \frac{\delta}{2} \right] , \tag{2.6}$$

where

$$n_{\text{e}} = \frac{N_{\text{A}}Z\rho}{AM_{\text{u}}} \tag{2.7}$$

is the electron density in the host material [57, 58, 60], with N_A being the Avogadro constant, ρ the bulk density, A the atomic mass number, and M_u the molar mass constant defined as one-twelfth of the molar mass of ^{12}C [61]. The effective mean excitation potential, I, describes the quantum mechanical energy levels available in a host material. These levels vary depending on the atomic structure of each material, making I different for different substances [57]. The excitation potential can generally be approximated as $I \approx 10Z$ eV, where Z is the atomic number of the host substance [58, 60]. $\frac{C}{Z}$ is a shell correction term, which takes into account the velocity of host materials electrons at lower particle energies. The density correction term, denoted as $\frac{\delta}{2}$, adjusts for the dielectric polarization at higher particle energies, especially as they approach relativistic speeds [59]. If $\beta\gamma > 1000$ (relativistic velocities), radiative effects begin to dominate, which are not described here since NDP particles are low energetic (as shown in Fig. 2.1). The Eq. 2.6 is only applicable to "heavy" ions, where the mass of the ion $m_{ion} \gg m_e$. This criterion is met by all charged particles that are emitted following neutron capture.
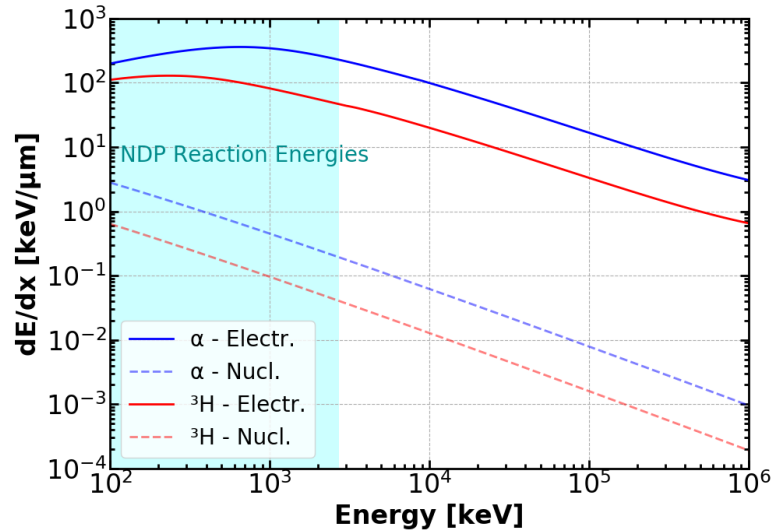
Figure 2.1.: Stopping power of ^{3}H and α particles in SiO$_2$. In the shown energy region, the dominant energy loss is due to electronic interaction. The cyan-colored area marks typical NDP energies. The curves were created with the data from the SRIM software [59].

The energy loss in a detector must be distinguished from the stopping power given by Eq. 2.6. The deposited energy is usually measured via the ionization of the medium, but there also exist atomic excitations with possible emission of low-energy photons which are not taken into account, contributing to the overall stopping power[1]. In a thin detector layer, it is also possible that energetic secondary electrons, so-called δ-electrons, leave the detector before their total energy is deposited, therefore reducing the mean

---

[1]Depending on the dielectric properties of the medium, the atomic excitations can lead to coherent radiation phenomena such as de-excitation radiation. The **P**hoto **A**bsorption **I**onisation (PAI) model, *e.g.*, provides a consistent description of the energy loss [62].

observed energy [63].

2.1.3 Depth Profiles

Charged particles created at a depth d with sufficient energy E_0 penetrate the bulk, emerging from its surface, where their residual energy can be detected. From the energy loss, the emission depth can be determined:

$$d = \int_{E_d}^{E_0} \frac{1}{S(E)} dE \,, \tag{2.8}$$

where E_d is the residual energy after leaving the sample. Typical NDP experiments are performed under a vacuum to prevent energy loss after the particles leave the sample. For the N4DP instrument, we typically use a threshold around 300 keV (at the electronic noise), limiting the maximum penetration depth.
Due to individual stopping power, each particle has a specific penetration range. To estimate a depth resolution for each ion, we assume that the emitted particles start at a depth d with an energy E_0 in the direction of a detector at an angle θ to the surface normal. The average range is given by

$$x = d / \cos \theta \tag{2.9}$$

through the sample, losing an average energy $\Delta E = x \cdot S(E)$ before reaching the detector [64]. This measured energy loss determines the path x with Eq. 2.8 and Eq. 2.9. Every sample matrix has a unique stopping power, affecting the resolution and depth of profiling. Furthermore, different particles created in NDP reactions have different energy loss profiles, resulting in different resolutions and depth ranges. On the one hand, the Li particle generated from the boron reaction has a higher charge than the α particle, resulting in faster energy loss and better profile resolution. On the other hand, α particles have a larger range, allowing for deeper profiles (usually on the μm level) [22]. In Fig. 2.2a, the range of α particles in different host materials was simulated. In Fig. 2.2b, different ions from Tab. 2.1 were simulated in a SiO_2 matrix to highlight the different ranges they can achieve. The data were obtained by using the Stopping and Range of Ions in Matter (SRIM) software [59].
In NDP, there are four inherent noise contributions resulting in signal broadening: intrinsic electronic and detector noise with standard deviation σ_{int}, energy straggling with σ_{stragg}, multiple small-angle scattering with σ_{scatt}, and uncertainty of the geometric acceptance with σ_{geom}. The energy straggling arises from the statistical fluctuations in both the number of collisions and the amount of energy transferred in each collision. The contribution of multiple small-angle scattering comes from elastic scattering on the nuclei. The uncertainty of geometric acceptance originates from the varying angle between the sample and detector [64, 65]. The particles can occasionally interact with air molecules in the chamber. However, the uncertainty arising from this is negligible if the vacuum is better than 10^{-3} mbar (for the N4DP chamber, it is typically $< 10^{-5}$ mbar). Figs. 2.3a,b show the signal broadening in longitudinal (depth) and lateral direction
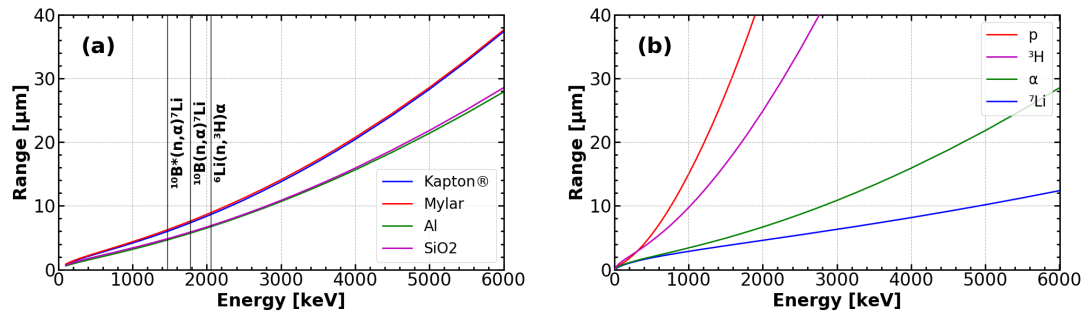
Figure 2.2.: (a) Range of α particles in different host materials. The original energies of the α particles in ^{7}Li and ^{10}B reactions for typical NDP experiments are marked with vertical lines. So, a ~ 7.5-μm-thin Kapton® foil stops a 2 MeV α particle. **(b)** Range of different particles in SiO$_2$. Due to the lower atomic number Z, light particles such as protons have a larger range than heavier ones. The curves were created using data from the SRIM software [59].

due to straggling and scattering in a SiO$_2$ matrix. The resolution decreases (increasing σ) for lower residual energies, as is usual for thicker samples.
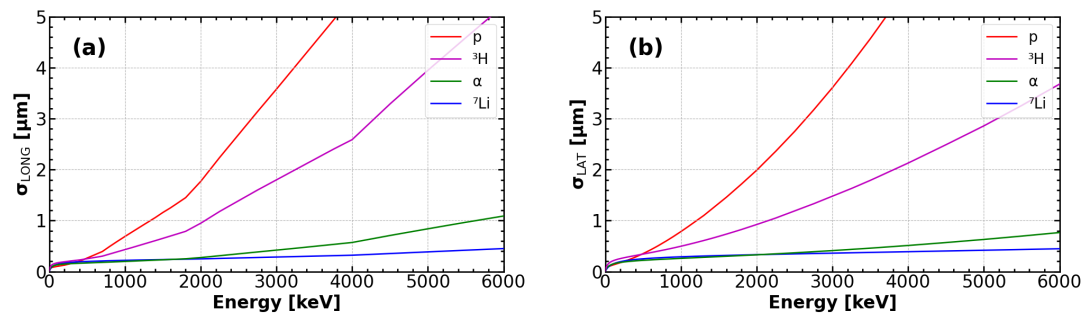
Figure 2.3.: (a) Longitudinal (depth) and **(b)** lateral resolution of different charged particles in SiO$_2$ host material versus their residual energies. The main contributions to the resolution σ are energy straggling and multiple small-angle scattering. The best resolution is given by the heaviest particle closest to the surface (highest residual energy). The graphs were created using data from the SRIM software [59].

The intrinsic signal broadening component is defined as $\sigma_{\text{int}} = \sqrt{\sigma_{\text{det}} + \sigma_{\text{elec}}}$. The detector component σ_{det} is discussed in Sec. 2.2.2 and the electronic component σ_{elec} is dependent on the electronics. Typically, one can determine the latter by using a well-known pulse signal as a test input and measuring its energy resolution. The energy spread σ_{geom} due to the possible range of acceptance angle between detector and sample is much smaller than all the other contributions [65] and is therefore neglected here.

2.2 Tracking-Detector Technologies

In particle physics, tracking detectors are essential for detecting not only the presence and energy of particles but also their trajectories. From them, the origin of the particle, the flight direction, and even more parameters, such as the particle momentum, can be deduced [66]. For these, several detection technologies are available. The most important tracking detectors are various types of gas-filled, scintillator, and semiconductor detectors, such as silicon detectors. The intrinsic capabilities of each of these types are compared in Tab. 2.2. Fundamentally, all detector types operate on a similar basic principle: a particle passes through the detector, interacts with it, and deposits some or all of its energy, producing an electric signal. The electronics then convert this signal into a useful form, which we can further analyze.

Table 2.2.: Typical resolution and deadtime of common charged particle tracking-detectors. The dead time is mainly limited by the amplifying electronics [67]. Summarized from [68].

Detector Type	Intrinsic Spatial Resolution	Time Resolution	Dead Time Per Cnt
Gas-filled detectors	$10 - 150 \, \mu m$	$5 - 10 \, ns$	$2 - 200 \, ns$
Scintillation trackers	$\sim 100 \, \mu m$	$100 \, ps/n^2$	$10 \, ns$
Silicon strips/pixels	$\lesssim 10 \, \mu m$	few ns	$\lesssim 50 \, ns$

In typical experiments, such as at the LHC [69, 70], it is crucial to minimize the energy loss and scattering of the impinging particle within the tracking detector material. Here, silicon strip detectors are increasingly being used as vertex detectors due to their unsurpassed spatial resolution at high count rates [71, 72].

Contrary to that, for energy spectroscopy or depth profiling, the stopping power in the detector should be maximized, as it is in the case of semiconductors. The advantages of semiconductor material properties can best be appreciated by comparing them with the most widely used radiation detectors based on gas ionization (values for silicon are used in this comparison; properties of other semiconductor materials are given in Tab. 2.3.) [73]:

- The narrow band gap (1.12 eV at room temperature) results in a higher number of charge carriers for the energy deposited. The mean energy required to create an electron-hole pair (3.6 eV) is an order of magnitude lower than the ionization energy of gases (typically ~ 30 eV);

- The condensed state with the density $2.33 \, g/cm^3$ results in significant energy loss per unit length. This characteristic enables the construction of thin detectors capable of generating sufficiently strong signals for our measurements. Therefore, the short range of δ electrons results in small shifts of the center of gravity of the

---

^{2}n ... index of refraction.

primary ionization from the track. Consequently, it allows for highly accurate position measurements, with accuracy down to a few μm;

- Electrons and holes can move almost freely in a semiconductor. The mobility of electrons ($\mu_e = 1450\,\text{cm}^2/\text{Vs}$) and holes ($\mu_h = 450\,\text{cm}^2/\text{Vs}$) at room temperature is only slightly affected by doping, allowing for fast charge collection (in the order of 10 ns). This rapid response enables using these detectors in environments with high count rates;

- The mechanical strength of the material allows the construction of self-sustaining systems;

- Using different mask dopings on a semiconductor wafer, complex field configurations can be established;

- Since both detectors and electronics can be built from silicon, it is possible to integrate them into a unified device.

In NDP experiments, semiconductor-based detectors are also favored for their high precision, good resolution, and compactness, which are crucial for analyzing low-energy particles. In particular, silicon strip detectors excel in energy and position determination. In thin detectors (typically $100 - 300\,\mu$m), the sensitivity to unwanted background signals, such as β^- and γ signals, is low, yielding a high Signal-to-Noise Ratio (SNR).

2.2.1 Semiconductor Detectors

Semiconductor detectors are commonly *p-n* junctions operated in reverse bias. This configuration creates a depletion zone empty of mobile charges and establishes an electric field that accelerates the charges generated by the radiation to the electrodes. The movements of both electrons and holes play a role in generating a signal at an electrode. The characteristics of the signal, like its widths and shape, depend on the velocity of the charge carriers $\vec{v}(\vec{x}) = \mu\vec{E}(\vec{x})$ and the geometry of the electrodes. These factors determine the induced current $i_S(t)$ as outlined by the Shockley-Ramo theorem [74, 75]

$$i_S(t) = Ne\vec{E}_w(\vec{x}) \cdot \vec{v}(\vec{x}(t)) \,, \tag{2.10}$$

where Ne is the sum of N elementary charges in the moving charge cloud, $\vec{E}_w(\vec{x})$ represents the "weighting field", which accounts for the coupling of the charge to a specific electrode, and $\vec{v}$ is the drift velocity. Integrating this current on the electrode results in the collected charge [68], which is done by the amplifier, yielding in the signal strength which is proportional to the deposited energy.

As the charge cloud moves within a detector, it expands due to diffusion (typically in the order of μm), leading to a phenomenon known as "charge sharing", where multiple electrodes collect charges from the same event. This effect can be used to improve the resolution of position detection (see Sec. 2.2.2).

Table 2.3.: Some intrinsic characteristics of semiconductor materials at $T = 300\,\mathrm{K}$ relevant to detector applications. From [63] and references therein.

Property	Si	Ge	GaAs	Diamond
Atomic number (Z)	14	32	31/33	6
Density $\rho\,[\mathrm{g/cm^3}]$	2.33	5.33	5.32	3.51
Bandgap E_G [eV]	1.12	0.66	1.42	5.50
e^- mobility $[\mathrm{cm^2/Vs}]$	1450	3900	8500	≈ 1800[3]
h^+ mobility $[\mathrm{cm^2/Vs}]$	500	1800	400	≈ 2300[3]
Average energy E_i for e/h creation [eV]	3.65	2.96	4.35	13.10

The charge collection time decreases with the bias voltage. Therefore, we can lower the collection time by "overbiasing" the detector. Here, overbias refers to a voltage higher than needed to fully deplete the detector, introducing a constant electric field component throughout the detector [68]. In typical fully-depleted Si detectors of $100 - 300\,\mu\mathrm{m}$ thickness, electron and hole collection times are in the order of $10\,\mathrm{ns}$. This fast charge collection is crucial for the efficient operation of high-speed and high-resolution applications.

Semiconductor detectors are usually designed with an asymmetric structure, *i.e.*, a heavily doped *p*-type (in the order of $10^{15}\,\mathrm{cm^{-3}}$) electrode paired with a minimally doped *n*-type volume (in the order of $10^{10}\,\mathrm{cm^{-3}}$) or the other way around. This design ensures that the depletion zone primarily expands into the volume with lighter doping, which is usually the bulk volume. The thickness of the depleted region is given by

$$d = \sqrt{2\rho\mu\epsilon U}\,, \tag{2.11}$$

with ρ being the resistivity (typically $1 - 10\,\mathrm{k\Omega cm}$), e the elementary charge, μ mobility of the carrier [76, 77] (see Tab. 2.3), ϵ the dielectric constant ($\approx 11.9\,\epsilon_0$ for Si), and $U = U_{\mathrm{ext}} + U_{\mathrm{bt}}$ the voltage applied to the system. U_{ext} is the external voltage, and U_{bt} is the "built-in" voltage, which is $0.1\,\mathrm{V}$. Together, the *p* and *n* regions form a capacitor with capacitance

$$C = \frac{\epsilon}{d}\,. \tag{2.12}$$

In strip detectors, the capacitance is largely influenced by the fringing capacitance to adjacent electrodes because the distance between them is typically much smaller than the detector thickness. For instance, the fringing capacitance between silicon strips is approximately $1 - 1.5\,\mathrm{pF}$ per centimeter of strip length, given a strip spacing of $25 - 50\,\mu\mathrm{m}$. A detailed study on this effect was done in [78, 79].

Finally, let us describe the influence of the temperature on the leakage current. Ideally, the reverse bias would eliminate all mobile charge carriers within the junction volume,

---

[3]Approximate averages. Values vary in the literature.

preventing any current flow. Nevertheless, thermal excitation may cause electrons to move across the bandgap, leading to current flow even without radiation exposure, known as the "dark current". Additionally, the probability of electrons crossing the bandgap significantly rises with the presence of impurities. These impurities create intermediate energy levels within the gap, acting as "stepping stones" for the electrons [67]. The reverse bias current depends exponentially on the temperature T, following the Fermi-Dirac distribution law [68, 80, 81]

$$I_R \propto T^2 \exp{-\frac{E_G}{2k_B T}}, \tag{2.13}$$

with E_G being the bandgap energy (see Tab.2.3) and k_B the Boltzmann constant. Thus, cooling the detector can significantly reduce the leakage current. For example, cooling a detector at room temperature by $\sim 20°C$ reduces the leakage current by a factor of 6 [67].

2.2.2 Semiconductor Detector Limitations

Modern detectors are essentially electrical in nature, *i.e.*, at some point along the way, the information from the detector is transformed into electrical pulses which can be treated by electronic means [55]. Its sensitivity, or capability of producing a usable signal after radiation or ionization, is given by the minimum amount of signal slightly larger than the average noise level. Since semiconductor detectors typically have low noise, their performance depends crucially on low-noise electronics, so the sensitivity is mainly determined by signal strength and input capacity [68]. In this subsection, some intrinsic limitations of Si semiconductor detectors are described.

Energy Resolution

The signal formed in the detector fluctuates in its amplitude, even for fixed energy absorption. In a semiconductor detector, energy is deposited by generating a number of electron-hole pairs. The absorbed energy divided by excitation energy gives the average number of signal quanta $N = \frac{E}{E_i}$, with $E_i = 3.6\,eV$ for Si [67]. This number fluctuates statistically, so the relative resolution is

$$\frac{\Delta E}{E} = \frac{\Delta N}{N} = \frac{\sqrt{FN}}{N} = \sqrt{\frac{FE_i}{E}}, \tag{2.14}$$

with $F \approx 0.1$ being the Fano factor [82, 83], which takes into account different excitation mechanisms, such as electron-hole pair formation, lattice vibrations - quantized as phonons - and other excitation, all reducing the statistical fluctuation of the signal. If $F = 1$, the events are independent, and they follow Poisson statistics. A detailed description of the Fano factor is discussed in [84, 85]. As can be seen in Eq. 2.14, the resolution is proportional to the square root of the energy. The limiting detector resolution is given by

$$\sigma_{det} = \sqrt{FE_i}. \tag{2.15}$$

We calculate the intrinsic energy resolution of a semiconductor detector given by the Full Width at Half Maximum (FWHM):

$$\Delta E_{\text{FWHM}} \approx 2.35 \cdot \sqrt{E} \cdot \sigma_{\text{det}} . \tag{2.16}$$

For a Si detector, α particles with an energy of about $5.5\,\text{MeV}$ yield an intrinsic energy resolution of $\Delta E_{\text{FWHM}} \approx 3.3\,\text{keV}$. A smaller bandgap (for example, by using Ge instead of Si) produces a larger signal and improves energy resolution ($\Delta E_{\text{FWHM}} \approx 3.0\,\text{keV}$ for Ge), but also exponentially increases the probability of thermal excitations. To avoid the high leakage currents encountered at room temperature, Ge detectors are usually cooled by liquid nitrogen.

Position Resolution in Strip Detectors

Typically, in silicon strip detectors, measuring the lateral position results in the binary information of a signal triggered by the impinging particle on a strip or over several strips with 1 = hit (over the threshold), 0 = no hit. The spatial resolution is a function of the strip pitch compared to the size of the charge cloud and the SNR. A more comprehensive description can be found in [86, 87]. In the one-dimensional case, where the width of the generated signal is small in comparison to the pitch width, we have no charge sharing. When only one strip has a hit, we can calculate the positional resolution in terms of standard deviation with the assumption that the particles uniformly illuminate the strip:

$$\sigma_x^2 = \frac{1}{p} \int_{-p/2}^{p/2} x^2 dx = \frac{p^2}{12} \;\Rightarrow\; \sigma_x = \frac{p}{\sqrt{12}} \approx 29\% \, p \,, \tag{2.17}$$

with p being the pitch width. Now, if we suppose that the detector response also contains information on the detected charge (signal height), we can determine a Center Of Gravity (COG) of the charge cloud. Here, this weighted position is a better estimate of the position than using a single strip. Additionally, a system noise signal with variance σ_n^2 can superimpose the signal, worsening the resolution. If we assume that the noise in the strips is smaller than the signal, and not correlated, and have the same value, we obtain for the standard deviation [88]

$$\sigma_x^2 = \sigma_n^2 \left[\left(\sum_{i=1}^{N} x_i^2 \right) + N \langle x^2 \rangle \right] + \mathcal{O}(\sigma_n^3) \,, \tag{2.18}$$

with N being the number of strips hit, and $\langle x^2 \rangle$ the variance of the hit position. For a common SNR of 10 ($\sigma_n = 0.1$) and two hit strips, we obtain a positional resolution of $\sigma_x \approx 8\% \, p$, which is ~ 3.6 times better resolution for the COG method when comparing to single strip resolution.

Timing Resolution in Si Detectors

Precise timing relies on a steep signal rise and small electronic noise. To meet these criteria, it is necessary to use thin detectors with high electric fields and amplifiers with quick rise times, which ensure a short collection duration and fast signal amplification [68]. We can estimate the variance of the time as follows

$$\sigma_t^2 = \sigma_{\text{Landau}}^2 + \sigma_{\text{jitt}}^2 + \sigma_{\text{arrival}}^2 + \sigma_{\text{dist}}^2 + \sigma_{\text{TDC}}^2 . \qquad (2.19)$$

The first term is described by Landau fluctuations, which correspond to fluctuations in the number of particles and energy transfer during the energy loss process [63]. We can minimize this term by applying corrections based on the amplitude information. The second term, noise jitter, is defined by the rise time t_r divided by the SNR. Having a high SNR reduces this term. The third term is the intrinsic jitter in the arrival time for semiconductor materials with internal amplification. It stems from the fluctuations in non-uniform charge deposition along the particle's trajectory, making it less impactful for thinner detectors. The fourth term describes signal distortions caused by non-uniform weighting field regions and fluctuations in (non-saturated) drift velocities. Lastly, the final term indicates time variations arising from uncertainties in digitization, which can be minimized using a GHz Time-to-Digital Converter (TDC) [68]. A more in-depth analysis of the timing resolution in silicon detectors can be found in [89].

2.3   Methods for Particle Imaging

Two primary techniques are utilized to project the lateral particle distribution within a sample using a Double Sided Silicon Strip Detector (DSSSD): camera obscura and coincidence. Both methods are shown schematically in Fig. 2.4.
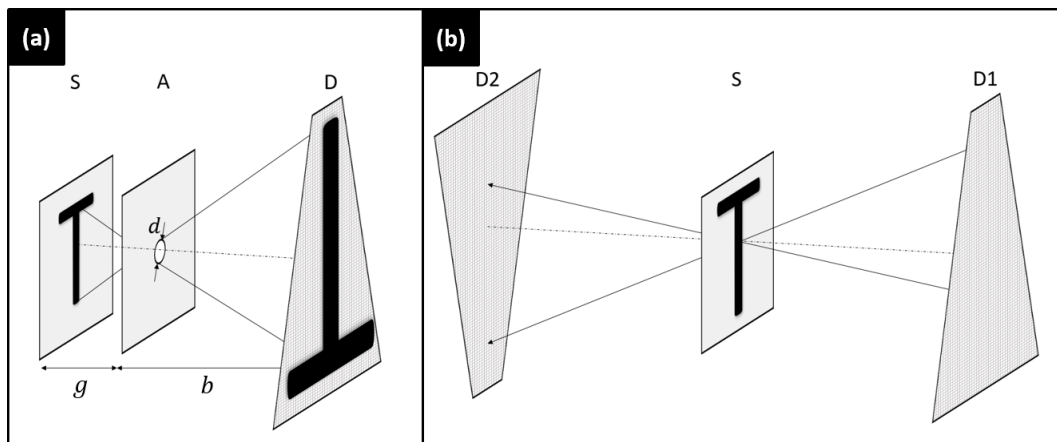
Figure 2.4.: Schemes of the **(a)** camera obscura- and **(b)** coincidence method for 2D imaging. The camera-obscura method uses an aperture (A) to create an inverse, magnified image of the sample (S) on the detector (D). In the coincidence method, event vertices of the sample are recreated using the back-to-back reaction events on both detectors (D1 and D2). Modified image from [90].

2.3.1 Camera-Obscura Method

This method uses a pinhole with a diameter d in front of the sample, creating a camera obscura-like setup. We denote the distance from the sample (S) to the aperture (A) as g and the distance from the aperture to the detector (D) as b. The aperture stops most particles created within the sample. Only those going through the pinhole reach the detector, creating an inverse, magnified image, as shown schematically in Fig. 2.4a. The magnification factor is given by $M = \frac{b}{g}$. Given d, g, b and the pitch width p, which is the pixel size, we can calculate the minimum height x_{min} between two points on the target plane that are still distinguishable. A sketch describing the camera obscura principle with x_{min} is shown in Fig. 2.5.

The minimal height on the sample plane x_{min} can be determined by considering two rays x_1 and x_2 that hit the detector one pitch width p apart. From the intercept theorem [91], we can deduce some geometrical relationships

$$\frac{x_{min}}{p} = \frac{g + z}{b - z} \text{ and}$$

$$\frac{d}{p} = \frac{z}{b - z} \ ,$$

with z being the distance from the pinhole aperture to the intersection point of the two rays. Using these relationships, we obtain

$$x_{min} = \frac{(g + b)d + gp}{b} \ . \tag{2.20}$$
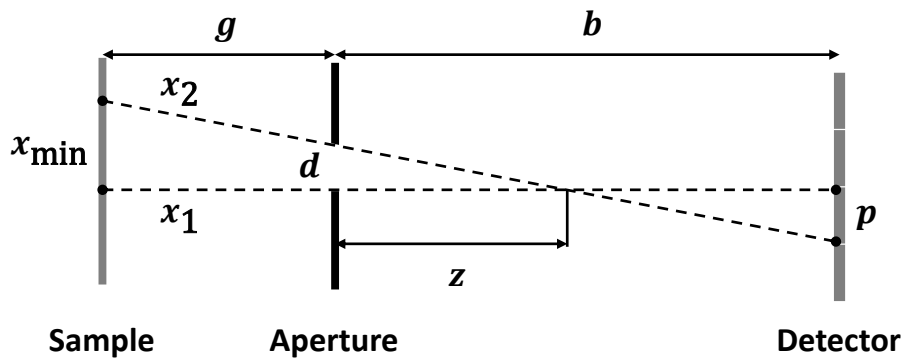
Figure 2.5.: Sketch of the geometric condition for the absolute resolution (x_{min}) of the camera obscura. The straight trajectories x_1 and x_2 of two points on a sample plane hit the detector at the height of p, which is the pixel size. z is the distance between the aperture and the intersection point of the two trajectories.
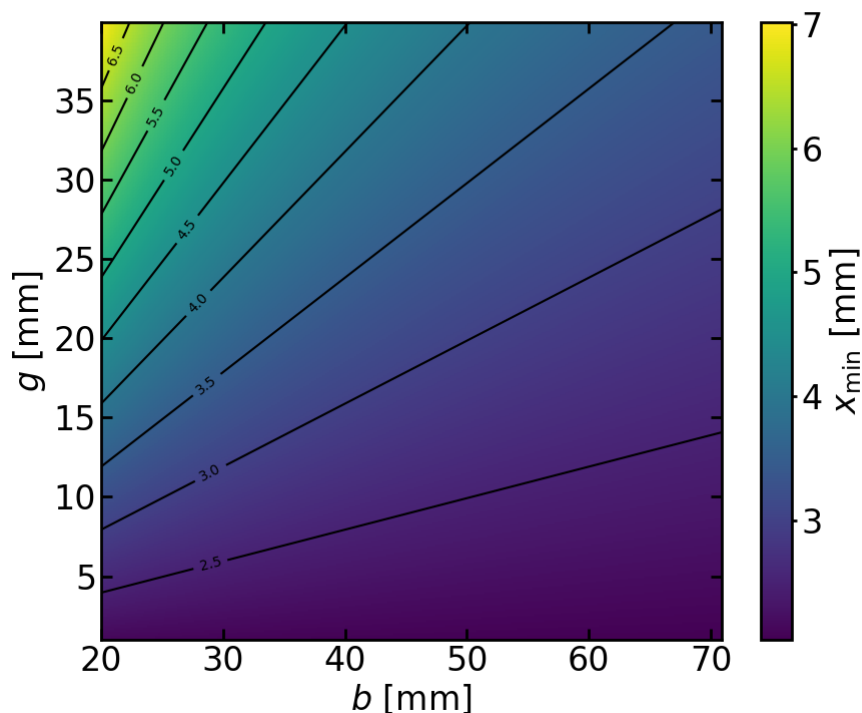
Figure 2.6.: Absolute resolution ($x_{\min}$) map with respect to the distance g between sample and aperture and the distance b between aperture and detector. For large magnification factors $M = b/g$, the absolute resolution $x_{\min}$ converges to the pinhole diameter $d = 2\,\text{mm}$.

In Fig. 2.6, $x_{\min}$ is plotted for different values of g and b, with $p = 0.52\,\text{mm}$ and $d = 2\,\text{mm}$. These values correspond to the pitch width of the strip detectors we used in this work and to typical pinhole diameters. On the one hand, if we put the aperture closer to the detector ($b \to 0$), $x_{\min}$ diverges because the rays x_1 and x_2 do not intersect anymore, and we cannot distinguish between the two points on the sample plane. If the detector is far away from the aperture ($b \to \infty$) or $b \gg g$, we obtain $x_{\min} \approx d$. On the other hand, if we put the aperture close to the sample ($g \to 0$), we again obtain $b \gg g$, and $x_{\min} \approx d$. Therefore, to obtain a good absolute resolution (small $x_{\min}$), a large magnification M is needed. We can also see from Eq. 2.20 that having a small pinhole diameter d and pitch widths p result in a better absolute resolution.

Let us now deduce the standard deviation of an image point on the detector. For this, we assume that each point on the sample plane radiates isotropically. A single point on the sample plane appears on the detector as a uniform distribution of the pinhole with the smeared size $m = \frac{b+g}{g} \cdot d = (\frac{b}{g}+1) \cdot d = (M+1) \cdot d$. The standard deviation is the convolution of two uniform distributions: one from the pinhole and the other from the pitch. The convolution of two uniform distributions results in a trapezoidal distribution. If $p = m/2$, then we obtain the triangular distribution [92]. In typical camera obscura experiments, the pinhole diameter d and pitch size p are small

Table 2.4.: Maximum depth for camera obscura and maximum thickness for coincidence for different materials. The camera-obscura depth gives the theoretical maximum penetration depth, which one can obtain from the lighter particles of the reaction. In contrast, the coincidence thickness gives a value for the theoretical maximum thickness of the sample to reconstruct the target from both reaction particles, which is given by double the maximum penetration depth of the heavier ion. These values do not take into consideration the electronic pedestal offset (energy cutoff) or further energy loss-inducing volumes, such as Kapton tape, which acts as a separation foil (used, *e.g.,* in [24] to block the α particles). Table recreated from [90].

Host material composition	Reaction of interest	Max. camera obscura depth [μm]	Max. coincidence thickness [μm]
Mylar-foil with LiF	$^6\text{Li}(n,^3\text{H})^4\text{He}$	50.4	16.8
SiG Electrodes (20% Si) [25]	$^6\text{Li}(n,^3\text{H})^4\text{He}$	90.5	30.4
CoRe Targets [95]	$^{10}\text{B}(n,^4\text{He})^7\text{Li}$	3.5	2.6

compared to the distances g and b. Therefore, we can approximate the trapezoidal distribution as symmetric and isosceles. The standard deviation σ is then given by [93, 94]

$$\sigma = \sqrt{\frac{2p^2 + 2p \cdot (m - 2p) + (m - 2p)^2}{12}} \,. \tag{2.21}$$

Lastly, it is to be mentioned that this method has the disadvantage of reducing the signal strength significantly due to the small solid angle Ω_d given by the small pinhole instead of the whole detector. Using a pinhole with a diameter of $d = 2\,\text{mm}$ at a distance of about $g \approx 33\,\text{mm}$ from the sample (for $M = 2$ at the N4DP instrument), we calculate the geometric efficiency to be $\epsilon_{\text{geom}} \approx 0.092\,\%$, which means a reduction by a factor of ~ 5.3 compared to the same setup without the pinhole. For the N4DP instrument, this can be compensated by the new focusing neutron guide (see Chap. 4).

2.3.2 Coincidence Method

In NDP kinematics, due to the conservation of momentum, the two particles are emitted back-to-back. When both particles are detected by two separate detectors (D1 and D2), as shown in Fig. 2.4b, we can reconstruct its vertex on the sample plane from the known geometry. This reconstruction requires a well-defined coincidence window with the corresponding energies. The lateral resolution of this method is determined by the width of the convolution of two uniform distributions of the same width (*i.e.* the same pitch width p), which forms a triangular distribution as described previously. The standard deviation is given in Eq. 2.21 for the special case of $p = m/2$. However, when detectors in a setup are slightly misaligned, the resolution may be compromised, leading to a miss-correlation between different strips of the detector.

This method is limited to the maximum achievable depth by the heavier particle since it loses its energy faster in the sample. The maximum thickness of the sample is then given by twice the maximum range of the heavier particle. In Tab. 2.4, different maximum depths are compared for the two methods.

With this theoretical foundation for neutron depth profiling and semiconductor detector technology, we are now in a position to create a detector system capable of lateral mapping. In the next chapter, we describe the development of the novel strip detector, with its PCB and electronics, to achieve state-of-the-art 4-dimensional neutron depth profiling.

Detector Development

In this chapter, we discuss the important steps for the development of the highly segmented detector modules, ranging from the optimization of the implantation profile, strip biasing, and signal transport to the custom-made ASIC-based electronics. We then show the implementation of the double-sided silicon strip detectors on a Printed Circuit Board (PCB) with these electronics.

3.1 Basic Detector Specifications

There are many silicon sensor suppliers in the market, but they mainly focus on mass production for industrial applications, and only a few are capable of manufacturing custom-made detector systems, as the production of small quantities of wafers is uneconomical for most suppliers due to the significant Research and Development (R&D) costs involved. CiS Forschungsinstitut für Mikrosensorik GmbH in Erfurt, Germany, showed interest in developing and manufacturing the novel DSSSDs.
For the special application discussed here, the following points need to be considered:

1. The type of bulk material and its implantation method to achieve the thinnest possible and homogeneous entrance window;

2. Coupling the detector to the compact, low-noise readout electronics;

3. Biasing the highly segmented detectors, which are operated in vacuum;

4. Detector geometry, segmentation, and thickness.

3.1.1 Development of Thin Window Detectors

The thickness of the insensitive region through which the incident radiation must pass to reach the depletion region is highly important. In high-energy physics experiments, particles typically pass through the detector material without a significant change in velocity. Therefore, the energy loss in this dead layer can be regarded as negligible. However, in NDP, the particles stop within a few μm, and therefore, not only the thickness but also the uniformity of this layer is important for resolution. Variations in the thickness of the dead layer can lead to the appearance of so-called satellite peaks [96]. We can explain this phenomenon by a simple model: mono-energetic particles with energies in the range of a few MeV hit a detector with a dead layer of thickness on the order of 100 nm, shifting the detected energy by a few keV. In case of a varying dead layer thickness, peaks at different energies would appear in the spectrum, possibly degrading the energy resolution. The insensitive region comprises several
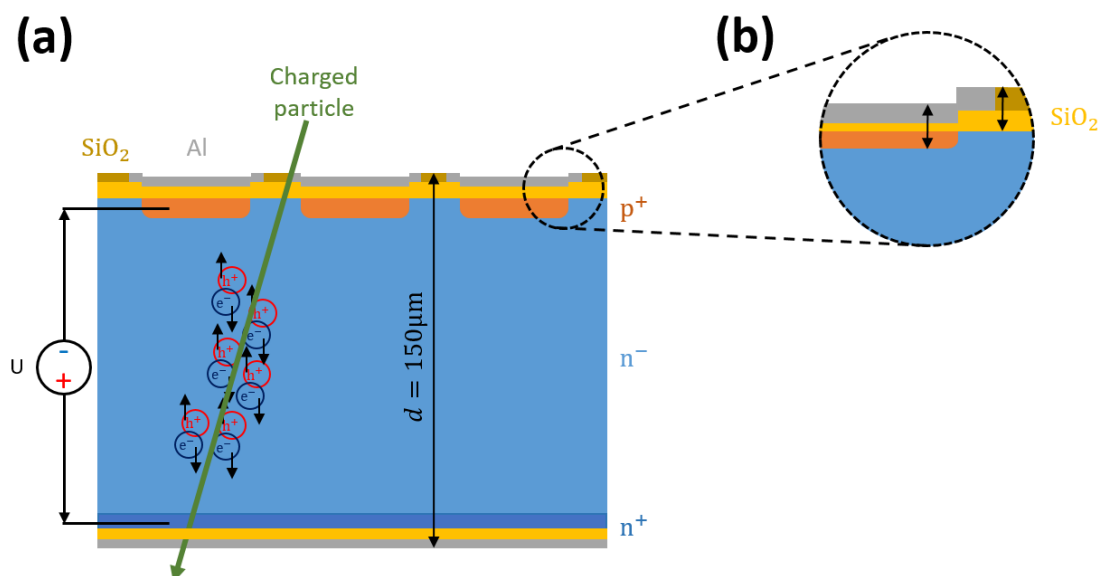
Figure 3.1.: (a) Sketch of the cross section of a *p*-in-*n* detector with AC coupled *p* side. When a charged particle enters the detector's active volume, it generates electrons and holes, which are collected at the n^+ or p^+ side, respectively. The superfix $^+$ denotes a strong doping (roughly 10^{19} to 10^{20} atoms/cm^3), whereas $^-$ represents a weak doping (roughly 10^{15} to 10^{16} atoms/cm^3). **(b)** Magnified picture of the insensitive region. By adding a second oxide layer (colored as gold), the so-called compensation oxide, the inactive region has the same thickness throughout the detector. Image adopted from [97].

layers: the *p* or *n* implant, the oxide layer, which acts as an AC coupling, and the contact Al metal layer. The depth of the inactive *p* layer of the diode can be controlled by varying the implantation energy and the dopant dose, as well as the subsequent heating in the process, where the dopants diffuse deeper into the crystal. To have a highly homogeneous insensitive region, a second so-called "compensation" oxide layer was deposited on the detectors, as shown in Fig. 3.1. This additional oxide layer guarantees the same energy loss through the insensitive region over the whole detector. We tested several smaller unsegmented test structures[1] for their energy resolution and their breakdown voltages. These test structures were produced like real single-sided detectors with the *p* implant, a thin metallization, and a guard ring structure on the *p* side, and ohmic contacts on the *n* side. Different acceptor (*p* side) depth distributions were achieved by ion implantation with different Rapid Thermal Annealing (RTA) [98] parameters: the accelerating potential was set to 6 kV, the boron ion beam fluence to $4 \cdot 10^{16}$ cm^{-2}, an annealing temperature from 950°C to 1100°C, and the annealing time from 5 s to 15 s. SIMS measurements [99] are shown in Fig. 3.2. Since the heating

---

[1]Provided by CiS Forschungsinstitut für Mikrosensorik GmbH

process typically overshoots the target temperature by up to 150°C in the first seconds of the process, it was decided to use a temperature of 950°C for 15 s. This showed an optimal and well-reproducible result for the p implant, with a layer thickness of 150 nm.
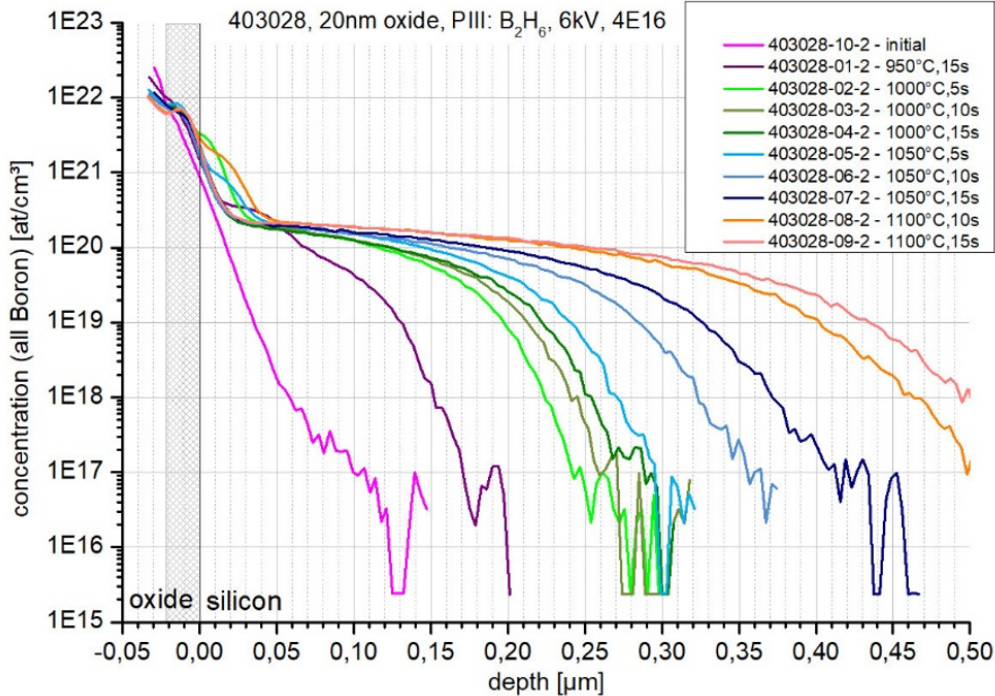
Figure 3.2.: SIMS measurements for the boron implantation profiles with different RTA parameters. It is important to keep the annealing temperature as low as possible to ensure a thin implantation profile, contributing to the overall dead layer. The pink line shows the initial implantation profile before RTA. The graph was kindly made available by the CiS group.

Overall we can estimate the thickness of the dead layer: the p implant (shown as the profile in Fig. 3.2 $\sim$ 150 nm), the SiO_2 AC coupling ($\sim$ 20 nm), and the Al contact[2]. The metallization was chosen to be $\sim$ 30 nm thick to match the ohmic resistance to the silicon layer. The oxide layer affects the implantation profile as the boron has to be implanted through the oxide. Overall, the dead layer is expected to be $\sim$ 200 nm thick. For the $Li^6(n,\alpha)H^3$ reaction, we obtain the following energy losses in this dead layer: $E_{\mathrm{loss}}(H^3_{2.7\,\mathrm{MeV}}) \approx 9.7 \pm 1.4\,\mathrm{keV}$ and $E_{\mathrm{loss}}(\alpha_{2.0\,\mathrm{MeV}}) \approx 53.5 \pm 2.7\,\mathrm{keV}$[3].

We tested the different unsegmented detectors (with different implantation profiles) with a point-like α source in our laboratory. The weak source[4] [100] contains 3 different radionuclides (listed in Tab. 3.1) deposited on a stainless steel disc. The line widths of each peak are less than 10 keV as specified by the company. Each radionuclide has a

---

[2]The Al was mixed with a small amount ($\approx$ 3%) of Si to reduce electromigration and have better adhesion to the SiO_2.

[3]These values were calculated by using the WebAtima energy loss calculator.

[4]By Eckert & Ziegler Nuclitec GmbH

nominal activity of 1000 Bq.

Table 3.1.: α emitter energies with corresponding intensities.

Radionuclide	α-particle Energy [MeV]	Intensity [%]
	5105	11.5
^{239}Pu	5143	15.1
	5155	73.4
	5388	1.4
^{241}Am	5443	12.8
	5486	85.2
^{244}Cm	5763	23.3
	5805	76.7

We glued the unsegmented detectors to an insulating support (shown in Fig. 3.3a). The backside of the detector was connected with conductive silver adhesive, while the front was wire bonded with 15-μm-thick wires to the preamplifier[5].
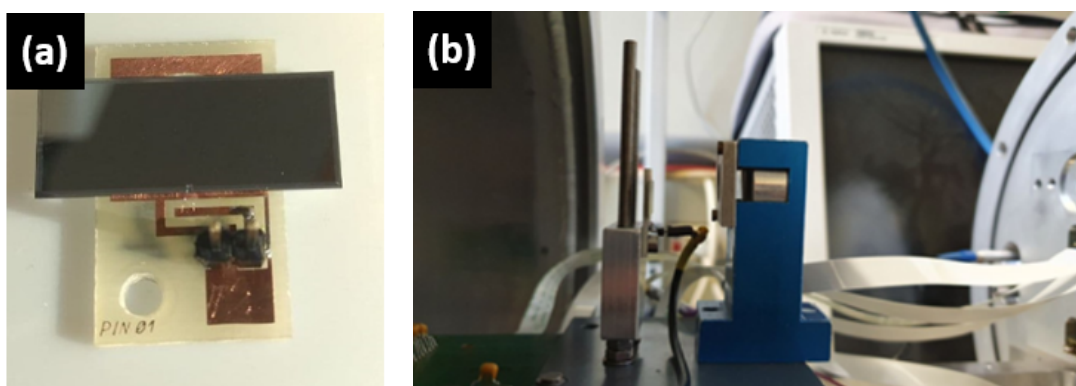
Figure 3.3.: (a) Unsegmented detector mounted on a plastic holder. The n side of the detector sits on a copper layer soldered to one electrode of the high voltage, while the p side is to the other one. **(b)** Detector test setup. The point-like α source is encased in a holder (blue in the figure). Left to the holder is the detector. The detector is connected to the high voltage via a preamplifier, from which the signal is fed to the digitizer.

We found that the annealing parameters of 950°C at 15 seconds, corresponding to the p implant of ~ 150 nm, gave us the best resolution with a $\Delta E_{\mathrm{FWHM}} = 16.7$ keV of the ^{241}Am peak at 5486 keV (shown in Fig. 3.4). For these measurements, the CAEN digitizer (the same as used for the N4DP instrument, described in Sec. 4.2) was used to acquire and analyze the data. Due to the proximity of the source and the large detector, the energy resolution has two major contributions. First, the dead layer thickness d influences the energy loss at different angles α to the detector with the contribution proportional to $1/\cos\alpha$. Second, the energy loss due to the straggling is proportional to

---

[5]Model A1422H from CAEN

$\sqrt{d}$. A further minor contribution is due to the low-noise electronics, which is expected to be around $2 - 3$ keV.
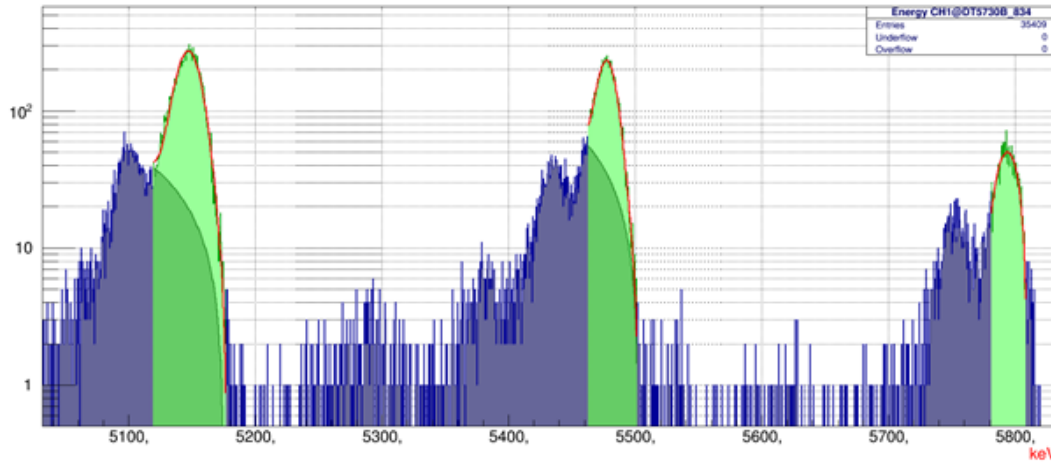
Figure 3.4.: α source measurement using an unsegmented detector. The spectrum was recorded using a CAEN DT5730SB digitizer. Gaussian fits were applied to the main peaks using the CAEN spectrum software. The ^{241}Am peak at 5486 keV gives the best fit with $\Delta E_{\mathrm{FWHM}} = 16.7$ keV.

There are two possible types of semiconductor detectors: p-in-n and n-in-p. In a p-in-n detector (as shown in Fig. 3.1a), the holes generated by the impinging particle are collected on the segmented side, whereas in a n-in-p, the electrons are collected. In general, both bulk types can be used to detect charged particles, with a few differences. One of the most important differences is the radiation sensitivity, which decreases over time. Effective defect models have been developed to simulate the damage caused by the irradiation of proton and neutron in such semiconductor detectors [101, 102]. For example, it can be shown that, after high flux irradiation (as expected in the LHC experiments [103]), n-in-p type sensors are more robust thanks to the lack of type inversion of the bulk. Radiation damage in silicon sensors effectively converts the n type to p, resulting in an increase in leakage current due to the higher recombination rate at the p-n interface. Irradiation, as shown in [104], increases the noise in p-in-n sensors due to stronger electric field regions, which accelerate thermally generated charge carriers. Nevertheless, the radiation dose at the N4DP instrument is far below the values expected at the LHC since the sensors are placed next to the neutron beam, and the beam intensity itself is 3 to 4 orders of magnitude lower. Detectors based on p bulks are not yet standard for semiconductor detection technology. As the CiS team has more experience producing detectors with p-in-n technology, we have chosen to use this for our detectors.

Achieving a highly compact detector module necessitates the AC coupling (discussed in the next subsection) of both sides being established on the detector itself. This is achieved by the thin oxide layer between the implant and the metalization, causing a problem with the insulation of the n strips as described in [105, 106]. For a p-in-n type detector, an electron-accumulation layer forms between the n-strips below the AC oxide layer. This layer of e^{-} creates an electric short circuit between the neighboring n

strips caused by the positive charges at the oxide interface [73]. Therefore, in order to isolate these strips, we have decided to use the *p*-stop technique [63, 107], in which a *p*-strip is added between the *n* strips, stopping the accumulation of electrons.

3.1.2 Coupling to Electronics

Two methods of coupling the detector to the readout electronics are possible: Direct Coupling (DC) and Alternating/capacitive Coupling (AC). For the DC, the preamplifier must absorb the dark current from the detector and compensate for it with a current of the opposite sign. If this is not compensated for, a high current in the amplifier will distort the shape of the signal through shifts in the pedestal and affect its linearity and dynamic range [34, 63]. An AC ensures that this leakage current is dissipated by a bias voltage. To collect all the charges generated in the depleted zone of the detector, the decoupling capacitance C_c must be at least equal to the magnitude of the individual strip capacitance of the detector C_d. To achieve a highly compact detector module, the concept was to achieve AC by an additional decoupling layer between the contact and the implant by depositing 2 different insulators: SiO_2 and Si_3N_4. The strip capacitance for the *p* side is in the order of $10\,pF$, from which we calculated the thickness of the decoupling layer to be less than $80\,nm$ for the oxide and less than $100\,nm$ for the nitride. The deposition of such thin layers of a relatively large area introduced 3D structures (so-called pinholes) that directly connect the metallic contact layer to the implant, resulting in the lack of AC. These pinholes can occur due to uneven deposition and etching [108]. In our case, the wet etching of the second oxide layer on the contact pads (to achieve a uniform dead layer) probably induced these pinholes. We observed the lack of AC for several strips independent of the insulator material. Therefore, we had to AC couple the detector by external Surface Mounted Devices (SMD) capacitors. The calculated strip capacitances for the *p* side strips is $5 - 20\,pF$, and around $50\,pF$ for the *n* side strips. High-resistance SMD capacitors usually introduce very little noise. Typically, the resistance of such capacitors is not always specified but is higher with a higher voltage rating. We chose to use capacitors with a maximum operating voltage of $200\,V$ and with a capacitance of $330\,pF$ for the *p* strips[6] and a maximum operating voltage of $100\,V$ and with $1000\,pF$ for the *n* strips[7].

3.1.3 Biasing Method

The bias voltage and the doping concentration of the bulk material determine the thickness of the depletion region (see Eq. 2.11). For minimum noise and homogeneous detector and to separate the *n* strip signals, the bulk must be fully depleted. There are several techniques for biasing circuits: via punch-through or polysilicon resistors. It is important to achieve high resistance values for the bias resistors to reduce their current noise contribution, which is inversely proportional to the square root of the resistance (Norton equivalent of the voltage source [109]). Although silicon detectors biased via punch-through resistors may initially show very low leakage current, it significantly increases after radiation exposure [110], resulting in higher noise. Polysilicon resistors

---

[6]C0402C331J2GACAUTO from KEMET
[7]C0402C102K1GECAUTO from KEMET

not only allow for a more compact design, which is very desirable in our case, but also show better radiation resistance [111]. Their fabrication is slightly more complex. We opted for the biasing method with polysilicon resistors with oxide openings as contacts to the p-implants and a biasing ring around the effective detector area connected to the high voltage supply (Fig. 3.5 as number 4). At the edges of the detector (shown in Fig. 3.5 as the number 2), we used a set of 15 guard rings (p implants) [112] to mitigate any inhomogeneities of the electric field.
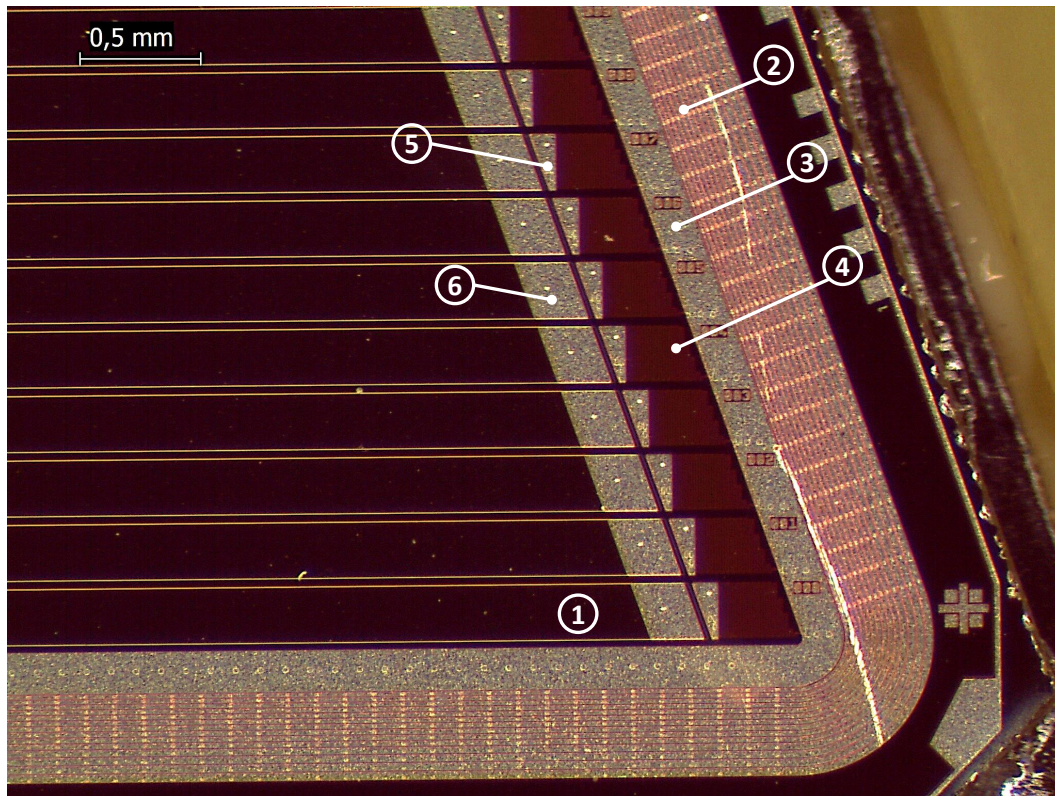
Figure 3.5.: Image of the major right corner from the p side of the detector. Important visible parts of the detector are labeled: 1. the first p strip of the detector; 2. the guard rings; 3. the bias ring; 4. the meander polysilicon structure that connects the bias ring to the strips; 5. the DC bonding pad; 6. the AC bonding pad.

3.1.4   Geometry, Segmentation, and Thickness of the Detector

The geometry of the detectors was chosen so that they could be adaptable to many different experiments. To achieve this, we designed them with an isosceles trapezoidal shape, allowing for variable segmentation for various experimental needs. With the fan-out shape of the n strips (shown in Fig. 3.12b), we obtain pixels of different sizes. Furthermore, by achieving different strip capacitances on the p side (which is shown in Fig. 3.12a), we can optimally adjust the resolution for different particle energies. The detectors were also developed in collaboration with the Transfer Reactions EXperiments (TREX) group at the REX-ISOLDE facility at CERN.

In the upgrade of the HI-TREX experiment, a high solid angle coverage aims at a better separation of low-intensity excited states from transfer reactions [38]. The isosceles trapezoidal shape of the detectors allows nearly 4π coverage when arranging 12 detectors symmetrically around the sample, as shown in Fig. 3.6.
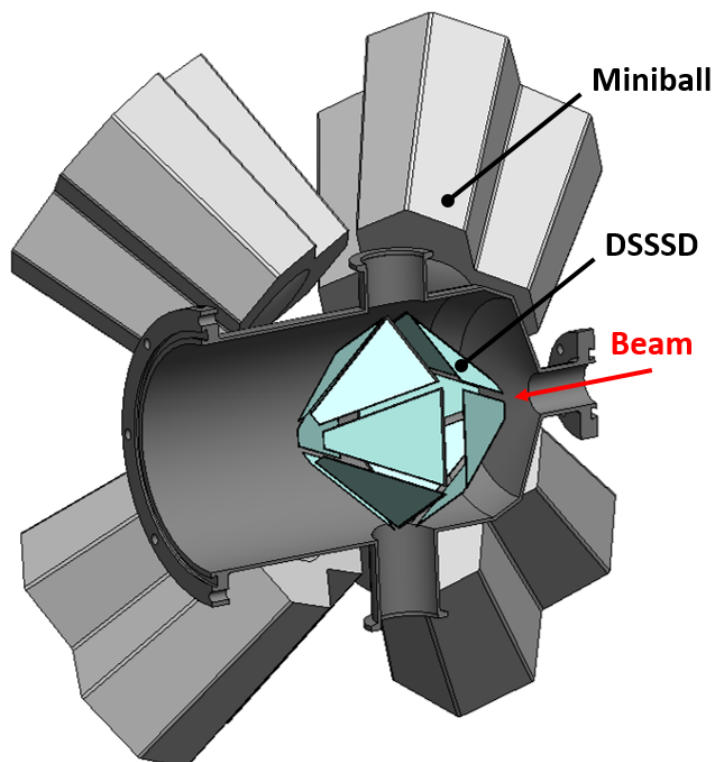
Figure 3.6.: Upgraded HI-TREX detector system at the CERN ISOLDE facility. In this experiment, a beam of heavy ions hits a target in the center. Around it, 12 detectors are symmetrically arranged to cover nearly 4π. The Miniball germanium detector array measures the γ radiation in correlation with the DSSSDs. Source: S. Golenev.

The external dimensions of the DSSSD are 60.42 mm on the long side, 10.65 mm on the short side, and it is 71.64 mm high. The effective area of the detector is smaller than the geometric area due to the extra ring for the bias and guard rings. It is $A_{\text{eff}} \approx 2251\,\text{mm}^2$. The segmentation is different for the two sides: on the junction side, the p implant strips are horizontal and parallel to each other. Their length varies from 57.0 mm to 8.9 mm from the major to the minor side of the detector. The ohmic n side has a fan-out of the strips (see Fig. 3.12b) from the minor to the major side of the trapezoid, with each detector segment having the same size and a length of approximately 68.9 mm. The last but not least critical factor was the thickness of the detector. This is just as important as the other specifications, as the background signal from β particles (generated from the Al chamber) is determined mainly by the thickness of the detector. A thickness of 50 μm is enough to stop all the possible NDP particles with very little background, but it leads to higher interstrip capacitances, worsening the energy resolution overall.

To balance the background and capacitance between the strips, we opted for a bulk thickness of 150 μm.

3.2   Control Electronics

In this section, the electronics are briefly summarized, based on the theses of C. Berner [97] and L. Werner [113], who made major developments of these parts. The development of the N4DP detector board, which was one part of this work, is discussed in detail at the end of this section.

3.2.1   Electronics and the DAQ system
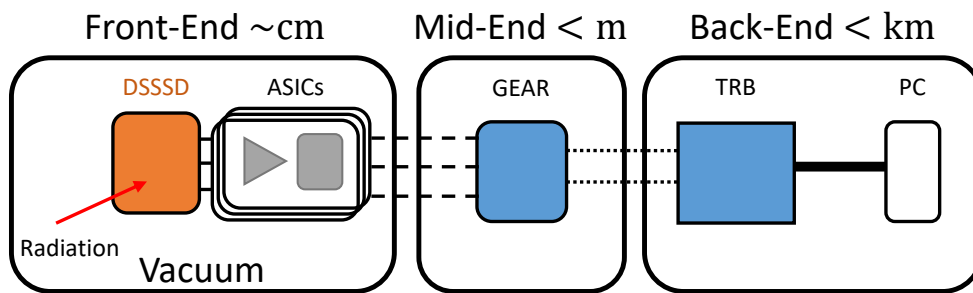
Figure 3.7.: Scheme of the DSSSD DAQ system for the N4DP upgrade. Unlike the DAQ system for the conventional NDP described in Sec. 4.2, where only the detector sits in the vacuum, here the electronic parts such as the preamplifier, shaper, and ADC (which are contained in the ASIC) are also placed in the chamber near the detector ($\sim$ cm). Outside the vacuum, close by ($<$ m) is the GEAR board, which monitors and controls important settings of the SKIROC ASICs. Further away ($<$ km) is the TRB network, which is responsible for the readout and transferring data to the DAQ PC.

Signal processing plays a critical role in the functionality of highly segmented radiation detectors, affecting key performance metrics such as amplitude measurement accuracy (*e.g.* energy resolution), position resolution, maximum event rate, and timing accuracy. Its implementation can also have a significant impact on power consumption, which is also an important factor in vacuum applications. The signal processing techniques are selected according to the specific needs of an application: a combination of several detector parameters (such as those described in Sec.3.1.1) and electronic noise [66]. Application Specific Integrated Circuit (ASIC) technology is often the basis for compact readout systems in highly segmented silicon detectors. This technology is advantageous in reducing electronic noise, saving space, and lowering power consumption compared to modularized electronics (as described in Chap. 4). The significant resources required for development and implementation mean that ASIC technology is primarily used in large-scale physics experiments or specific consumer market applications [114]. This technology was also used for the N4DP upgrade. An overview of the

Data AcQuisition (DAQ) scheme from the DSSSD to the PC for the N4DP instrument upgrade is shown in Fig. 3.7.

The electronics requirements for the upcoming N4DP upgrade [36] towards four-dimensional tomography, as well as the TREX experiment upgrade [38] at MINI-BALL [115], are the following: vacuum-safe operation, low power consumption, good spectroscopic energy resolution (in the keV range), large dynamic range, a high number of channels for a small footprint, as well as reasonable data rate (in the order of kHz) and a high number of control lines. All these points motivate the use of SKIROC ASICs [116] as front-end electronics. A generic FPGA-based board (the GEAR board) is used to control the settings of the various stages in the ASICs, to provide clock timing information, to distribute power to the active components on the front-end, and to provide a communication platform for the back-end. To handle multiple detector boards simultaneously and to provide a user-friendly interface on the DAQ PC, the TRB network is used as the back-end. Each of these electronic components is briefly described below.

Front-End SKIROCs

The Silicon Kalorimeter Integrated ReadOut Chip (SKIROC) is the front-end ASIC designed for the readout of the silicon PIN diodes for the Electro Magnetic CALorimeter (EMCAL) at International Linear Collider (ILC) [116]. The chip was optimized for an input capacitance of 20 pF. One chip has 64 input channels with positive polarity, each with a preamplifier of variable gain, two slow shapers, one with a low gain ($G = 1$) and one with a high gain ($G = 10$), and one fast shaper for trigger generation [117]. After a tunable delay, a trigger threshold sends a hold signal to each stage in the chip, which stores two of the following lines: the low gain, high gain, or timing information in an embedded Switching Capacitor Array (SCA). For the SKIROC 2A chip, there are 15 such capacitors per channel, each with a capacitance of 500 fF. When all 15 capacitors are filled, the state of the chip is changed from acquisition to readout mode. An analog multiplexer and a Wilkinson Analog-to-Digital Converter (ADC) convert the data into digital values, which are then sent to the mid-end electronics.

By using multiple shapers with variable feedback capacitance, these chips can handle a large dynamic range from 0.1 MIP (0.4 fC or $\sim 2500\,e^-$) to 2500 MIP (10 pC or $\sim 62.5 \cdot 10^6\,e^-$). In addition, they have a low Equivalent Noise Charge (ENC) ($\sim 6\,\text{keV}$) and consume very little power when operated in a certain mode[8]. A simplified circuit diagram of the SKIROC 2A is shown in Fig. 3.8.

---

[8]In the so-called power pulsing mode, the SKIROC 2A is operated only when a signal pulse is expected, thus consuming very little power on average (down to 25 μW per channel)
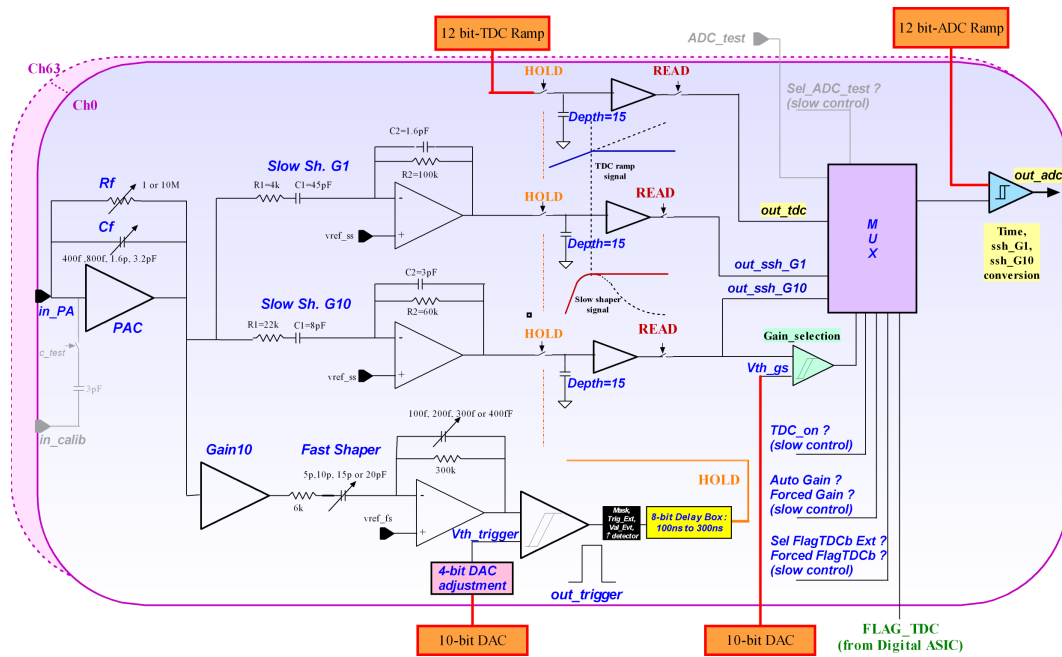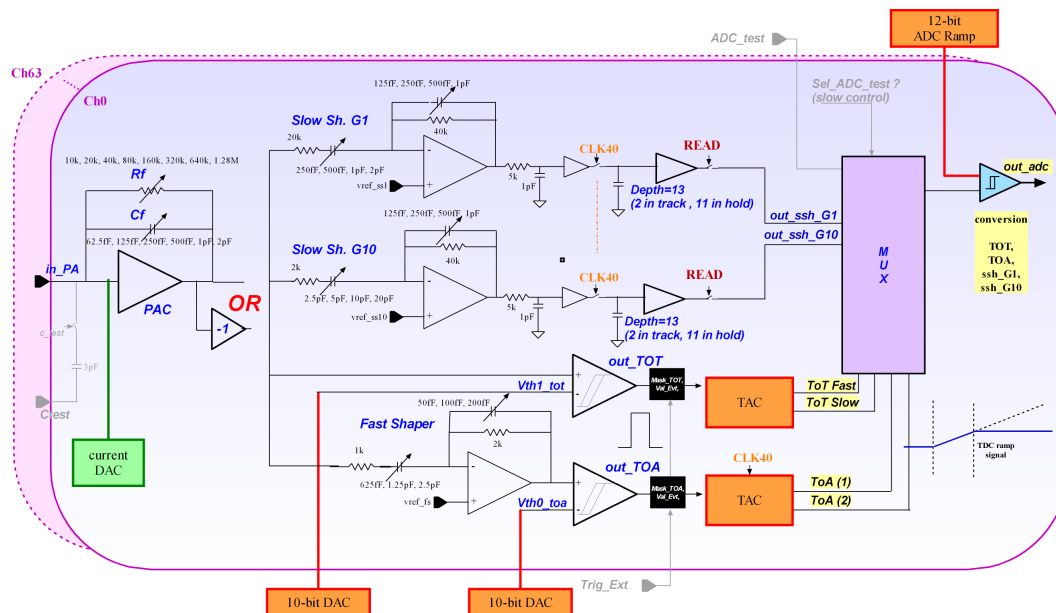
Figure 3.8.: Simplified circuit diagram of the SKIROC 2A chip. The main components of the diagram are: the preamplifier (PAC), slow shapers with low ($G = 1$) and high gains ($G = 10$), a fast shaper for trigger discrimination, the switching capacitor arrays with depths of 15, the multiplexer, and the analog to digital converter. The diagram was kindly made available by S. Callier from the Omega Microelectronics Center [117].

Since the SKIROC 2A can only accept a positive input, we need a different chip for the n side: the SKIROC CMS [118]. Originally designed for the CMS experiment [69], the CMS ASIC is a chip derived from the SKIROC 2A, which allows for both polarities, but with some drawbacks, such as missing self-trigger generation, a worse energy resolution, less number of SCAs (13), and the method of measuring high input-charges with the Time-over-Threshold (ToT). A simplified circuit diagram of the CMS chip is shown in Fig. 3.9.

The SKIROC CMS chip is optimized for an input capacitance of 70 pF. It features 64 input channels of both polarities, with 48 different gain settings for the preamplifier, 16 shaper settings from $10 - 150$ ns for two slow shapers, one with a low gain ($G = 1$), and one with a high gain ($G = 10$), and 8 settings for a fast shaper which provide the timing information by using two discriminators, a Time-of-Arrival (ToA) and a TOT based on Time-to-Amplitude Converter (TAC) with time steps of 25 ps. The CMS chip acts as a waveform sampler (in rolling mode) to record the signal's shape but can also be externally triggered in a so-called single-event mode, which is also used for the N4DP instrument. After an external trigger, the time, low, and high gain information is stored in 13 SCA memory cells and converted by a 12-bit ADC. Although there are 13 memory cells in the CMS chip, due to the rolling mode, only 11 can be used in single mode. As the energy resolution of the CMS chip is worse ($ENC \approx 8$ keV) than that of the 2A chip, the N4DP instrument primarily uses the CMS for the strip hit information from

the n side of the detector and background suppression by a comparison of energies from the n and p sides. The SKIROC 2A is used to obtain the trigger and precision energy information from the p side. Events from both chips, using a time and energy coincidence, give the pixel information on the detector.

Figure 3.9.: Simplified circuit diagram of the SKIROC CMS chip. The architecture of the CMS chip looks very similar to that of the 2A chip, but it has an additional inverting amplifier and additional timing discriminators after the fast shaper, allowing for ToT and ToA information. The diagram was kindly made available by S. Callier from the Omega Microelectronics Center [118].

Mid-End GEAR

The GEneric Asic Readout (GEAR) board (shown in Fig. 3.10) as a DAQ was developed as part of the doctoral thesis of C. Berner [97] and L. Werner [113]. The board must be generic and scalable for nuclear physics experiments with silicon detectors, such as HI-TREX or NDP. Using Field Programmable Gate Array (FPGA) and off-the-shelf components, it was possible to create a module to control and power the ASICs and interfaces to the back-end electronics. Furthermore, it provides timing signals to the ASICs, timestamps the events faster than the ASIC's clock, and ensures proper functioning of the SKIROC CMS in the single event mode triggered by the SKIROC 2As. There are two different operating modes for each of the SKIROC ASICs. First, the SKIROC 2A requires two clocks at 5 MHz and 40 MHz, which generate the trigger times. The mode of operation can be selected via the SlowControl settings. The CMS chip is designed to operate at 40 MHz, and it is not necessary to change the internal clock of this chip. However, it still has different operating modes: the rolling and the single event mode. One can choose between these two modes via the SlowControl. In the single event mode, the CMS chip can be triggered externally, *e.g.*, by the SKIROC 2A - this mode is used in our experiments since the signal generated in the detectors

should be collected simultaneously on both sides. During a full readout cycle, the ASICs have a ~ 7-ms-long dead time. This can be reduced to $\sim 1\,\text{ms}$ by switching to the faster clock in the 2A, but reduces the readout stability overall.
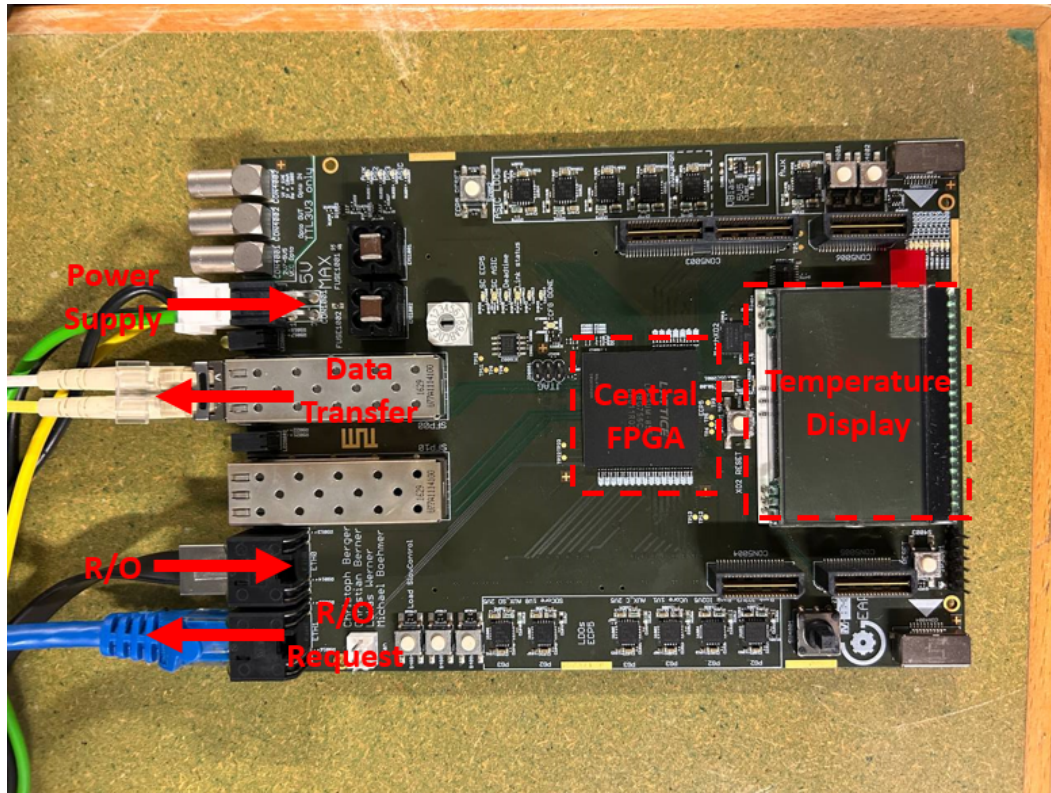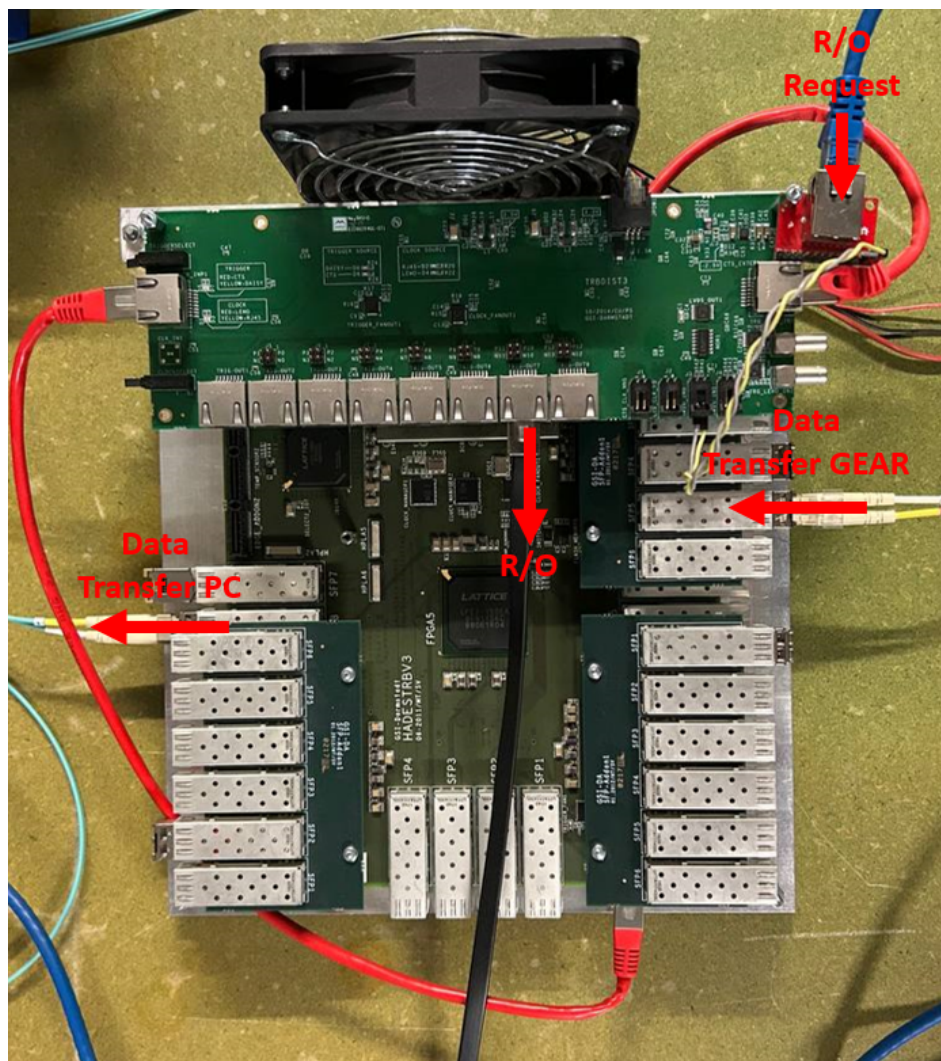

Figure 3.10.: Picture of a GEAR board. Important parts and connections are labeled.

Back-End TRB3

The TRB3[9] (shown in Fig. 3.11) framework was originally designed for the High Acceptance DiElectron Spectrometer (HADES) experiment at GSI [119] and is mainly used for TDC measurements and digital readout [120]. A central FPGA acts as a trigger system, managing the data collection, and four additional peripheral FPGAs can be configured for various applications. At the N4DP instrument, the back-end TRB3 is mainly used for the readout, bunching, and transfer of the data, as well as setting the control parameters from the DAQ-PC. It hosts a gigabit ethernet (GbE) controller, which connects to Dynamic Host Configuration Protocol (DHCP) as a simple integration into any GbE network. Once the data are collected from the GEAR board, they are sent to the computer via an optical fiber using a User Datagram Protocol (UDP) connection. The raw data are then stored in a bundled 'dabc' format [121] and unpacked into a readable format using the ROOT framework [122]. The structure of the raw data of both ASICs is briefly described in Appendix B.

---

[9]From trb.gsi.de: *what does TRB mean? You can choose between: TDC-Readout-Board, Triggered-Readout-Board and Triggerless-Readout-Board*

In our experiments, the following DAQ scheme was used: after a particle creates a trigger on the p side, all 64 channels of one of the two SKIROC 2A are triggered, with (optimally) only one channel having the trigger information, while the others contain the baseline. This trigger is sent through the GEAR board to the CMS chip, externally triggering it. The data from all channels on the n side is stored. After a maximum number of 11 events, the memory cells of the CMS chip are full, and the chip sends a "full" signal to the GEAR board. The maximum number of events is adjustable in the FPGA code. The GEAR board sends a readout request to the TRB3 backend, which in turn starts collecting the data.

Figure 3.11.: Picture of a TRB3 board connected to a single GEAR board and the PC. Important connections are labeled. When the memory cells of the ASIC chips are full, the GEAR board sends a readout request to the TRB3 board. This then collects the data, bundles it, and sends it to the PC via optical fibers. Up to 24 GEAR boards can be simultaneously connected to a single TRB3 board.

3.2.2 Printed Circuit Board

The detector PCB (shown in Fig. 3.12, see also Appendix A) has six layers, an area of $137 \times 126 \, mm^2$ on a standard FR4 TG170[10] board, and is 1.6 mm thick. A 1 mm z-axis milling on one side of the board allows for gluing the detector, plus an additional support frame and support bar on the minor side - both made of silicon. The support bar holds the detector flat while the n side is bonded to the gold-plated (ENIG) contacts. Next to the detector contour are the AC coupling capacitors, the SKIROC ASICs, and the High Voltage (HV) supply lines with RC filters. There are also several 3-mm-diameter holes (contacted to the ground) on the board for mounting to external support. On the sides of the board, there are LEMO connectors for HV power and signal in and out for test purposes, as well as FFC connectors for communication between the ASICs and the FPGA of the GEAR board. Other passive components (mainly resistors and capacitors) are distributed across the board, as well as four active I^2C temperature sensors located under the ASICs and on the PCB, and a single supply operational amplifier[11] above the CMS ASIC for a backup special readout mode[12] of the CMS. A picture of a DSSSD mounted on a PCB is shown in Fig. 3.12c.

On the p side, the detector is segmented into 266 strips. To match the total amount of 128 readout channels from two SKIROC 2A ASICs, we bonded the p strips in groups of 2 and 3. We used a lower granularity (3 strips bonded together) for nine channels on the minor side and the very first channel on the major side (shown in Fig. 3.12a).

In short, we made the following steps to successfully install and test the detectors:

1. PCB development and production

2. Mounting of electronic parts on the PCB

3. Testing the equipped PCB with an artificial signal

4. Development and production of support plates - Al plates for keeping the PCB flat during bonding

5. Gluing the silicon frame into the printed circuit board

6. Gluing the DSSSD to the frame

7. Gluing the support bar on the minor side (1 day dry each)

8. Wire bonding of the p and n strips, and the HV to the respective pads

9. Final testing of the DSSSD with radioactive sources

---

[10]From Multi Circuit Boards Ltd.

[11]MAX4012

[12]In the special mode of operation of the CMS ASIC, only the hit information of the n side is collected, with no additional power or timing information. In this mode, the readout can be accelerated to 200 MHz, reducing the dead time between two hits to $\approx 0.5 \, \mu$s.
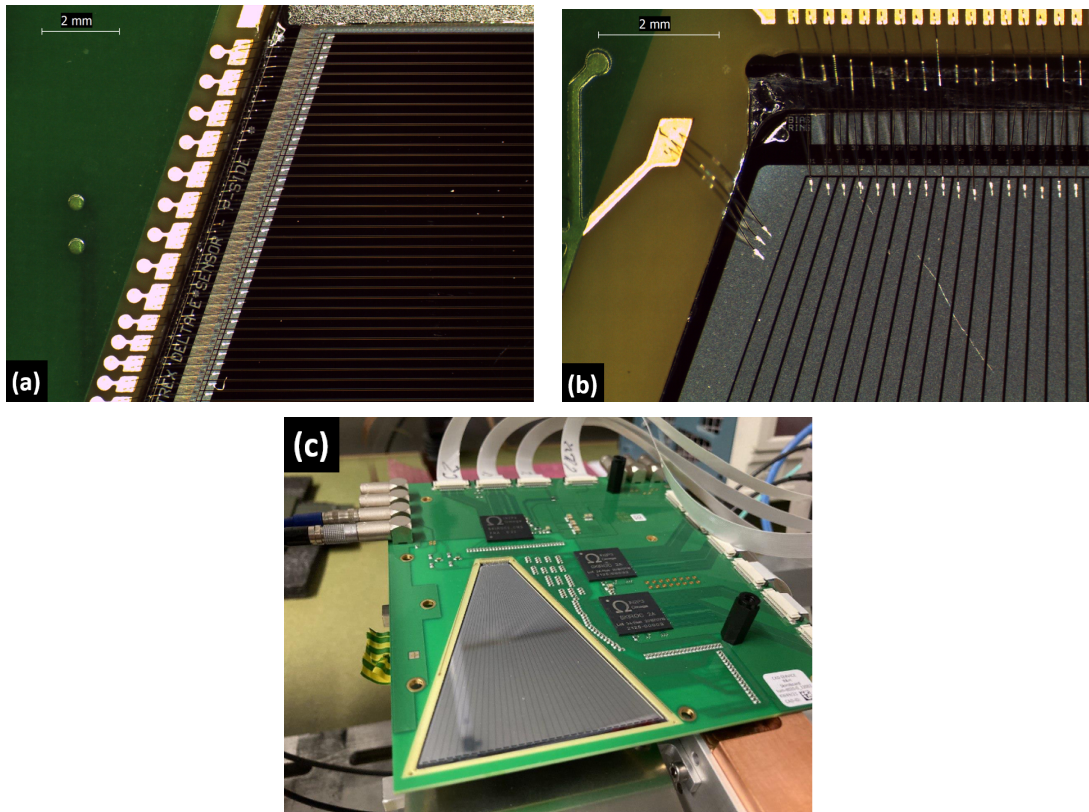
Figure 3.12.: (a) Upper left part of the detector from the p side. The last 9 channels are bonded in groups of 3 strips. Note the small support bar at the top of the detector. **(b)** Upper left part of the detector from the n side. We can see the bonding to the HV and the long bonds from n strips to the pads. **(c)** Detector PCB. The n side of the detector is on the side of the PCB hosting the ASICs. The HV is supplied via LEMO connectors on the left side of the board. Flexible Flat Cables (FFC) connect the ASICs to the GEAR board, which sits outside the vacuum.

With the completion of the design and implementation of the novel double-sided silicon strip detector and its electronics on a custom printed circuit board, we are now in a position to characterize the system and take further steps towards four-dimensional measurements.

N4DP Instrument

The development of the N4DP instrument was primarily done by L. Werner [36, 113] and M. Trunk [53, 123]. In this chapter, we provide a brief overview of the instrument, including upgrades made within the scope of this work. At the end the implementation of the new detectors in the N4DP instrument is shown.

4.1 Experimental Setup
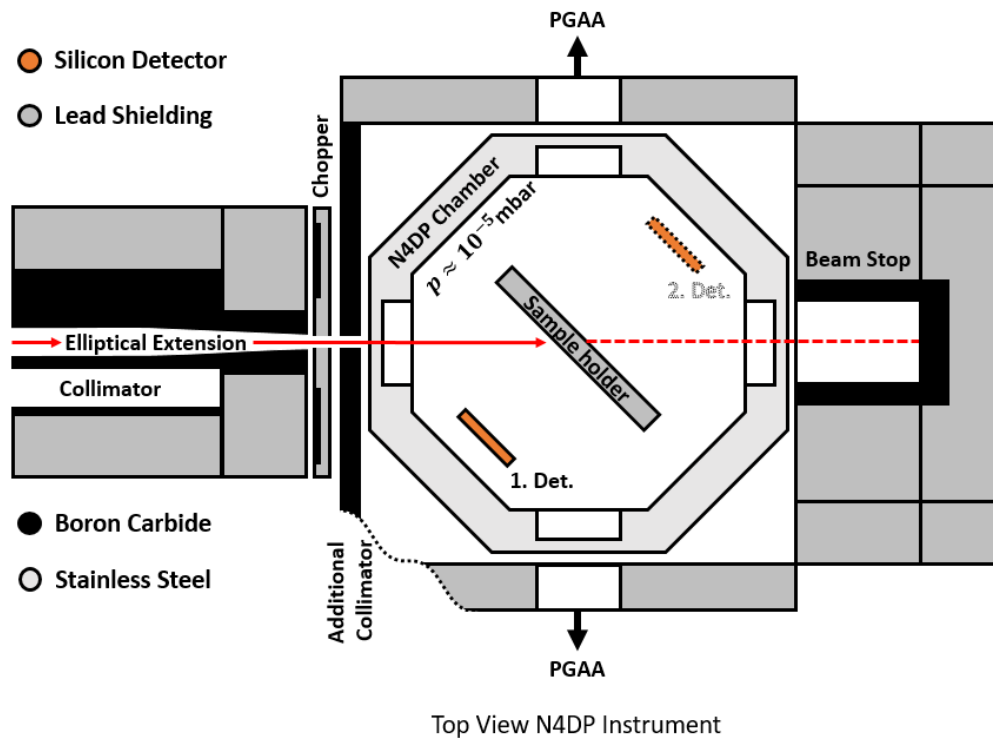
Figure 4.1.: Top view of the N4DP instrument. The neutrons from the reactor, transported by one of the neutron guides, pass through an optional chopper system and undergo additional collimation before entering the N4DP chamber. Upon arrival, they interact with the sample, which is rotated at a 45° relative to the beam axis before being absorbed by the beam stop. Adapted from [36].

A top-view of the N4DP instrument is shown in Fig. 4.1. The instrument uses a cold neutron beam at the PGAA facility at Forschungs-Neutronenquelle Heinz Maier-Leibnitz (FRM II), with an average neutron energy of 1.83 meV (6.7 Å). This beam is directed from the cold source to the PGAA facility via the curved neutron guide NL4b. The last 6 m of the guide are elliptically tapered, and its last 1.1 m can be replaced by a set of collimators, where the neutron flux is 2×10^9 cm^{-2}s^{-1} within a beam cross-section of 2×1 cm^2 [124] and a uniform beam profile. The flux density, expressed as a thermal equivalent value, was determined using gold foil activation. Within the budget of the N4DP project, E. Kluge simulated an optimized elliptical taper design yielding a neutron flux of $\sim 5 \times 10^{10}$ cm^{-2}s^{-1} with a focal point at ~ 15 cm away from the end of the guide. This is more appropriate for the other experiments (PGAA, NDP, and Prompt Gamma-ray Activation Imaging and Neutron Tomography (PGAI-NT)) as well. This new elliptical guide extension has already been installed but has not yet been characterized due to the shutdown of the FRM II since the start of the year 2020. At this sample position, the beam spot is collimated to a circle of approximately 4 mm in diameter.

To reduce the background from neutrons and γ radiation that may be emitted from the neutron guides and the surroundings, the guides are surrounded by shielding made of a mix of boron-containing rubber and lead bricks. After the vacuum chamber, a beam stop made of boron carbide plates and lead bricks absorbs the remaining neutrons [124].

4.1.1 Vacuum Chamber - Outside

The N4DP vacuum chamber is made of two stainless-steel cylinders and an octagonal aluminum profile (shown in Fig. 4.4). The octagonal piece contains four CF100 and four CF63 flanges. To minimize the interaction with the neutron beam, aluminum windows with a thickness of 100 μm and a diameter of ~ 40 mm were used at the front and rear flanges to serve as neutron beam entry and exit windows. Perpendicular to the neutron beam, two further flanges can be found, which are the windows for the γ-ray detectors used for PGAA experiments. The other four larger flanges are designed for electronic interfaces, such as the control system feed-through or connections to sample environments, such as electrical connections (for powering batteries or electronic samples), monitoring and regulating the temperature. The top lid has two KF40 connections, used for pressure regulation and evacuation processes. Two feed-throughs on the top lid are used for the preamplifier and the electric connection to the detectors in the chamber. A 30 cm $\times$ 15 cm opening on the lid allows for easy exchange of samples and is closed by an aluminum lid. The chamber is typically pumped down to a pressure of $\sim 10^{-5}$ mbar by using a roughing pump[1] and a turbo-molecular pump[2].

4.1.2 Vacuum Chamber - Inside

Inside the chamber (shown in Fig. 4.4), samples are placed on a modular sample holder, which can be adapted to the requirements of different applications [123]. A mounting system with a sliding caliper is used, enabling quick and precise switching between

---

[1]ECODRY plus, Leybold
[2]Turbovac 350i, Leybold

different sample holders. The mounting system uses a dual linear stepper motor[3], serving as a two-axis target drive for accurate sample placement. Typically, the angle between the sample and the neutron beam is 45°, but it can be adjusted to different angles if necessary.

The standard detector for depth profiling, a SSB detector[4], faces the sample surface at a distance between 87.1 mm and 141.1 mm in 9 mm increments. Additionally, the detector can also be placed at angles between 0° and 90° in 15° increments relative to the neutron beam, both in front of and behind the target stage. A mechanism in front of the detector facilitates the placement of various separation foils or pinhole apertures. The diameter of the active surface of the detector is 13.8 mm, and a typical distance from the sample to the detector of about 100 mm. Thus the geometric efficiency $\epsilon_{\mathrm{geom}} \approx 0.48\,\%$.

4.2   Default Data Acquisition

The DAQ can be performed analog or digital (schematically shown in Fig. 4.2). For the analog system, we use standard electronic modules based on the Versa Module Europa (VME) bus and Nuclear Instrumentation Module (NIM) systems. A NIM-based HV supply[5] powers the detectors at $\approx 100\,\mathrm{V}$. The detector output signal is fed to a charge sensitive preamplifier[6] and then further shaped by a shaping module[7] with a 1-μs-shaping time. This is then fed into a peak-sensing VME ADC[8]. The data is collected on an event-by-event basis using the MBS And ROOT Based Online/Offline Utility (MARaBOU) software [125], which operates within the ROOT data-analysis framework [122] incorporating the signal distributor Multi Branch System (MBS).
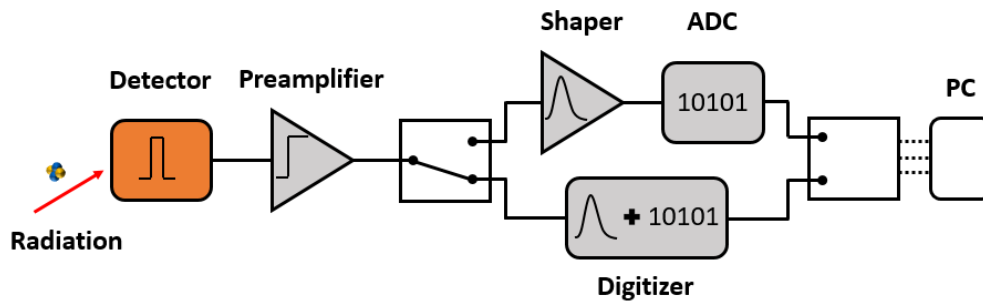
Figure 4.2.: Scheme for two different DAQ systems used at the N4DP instrument. The preamplified detector signal can either be shaped using analog modules and then converted into digital data or handled by a desktop digitizer.

Instead of using the analog shaper and an extra ADC as VME modules, a new digi-

---

[3]VT-50L, Micronix
[4]AD-025-150-100, ORTEC AMETEC
[5]MHV-4, Mesytec
[6]WA1422H090F2, CAEN
[7]MSCF-16, Mesytec
[8]V785, CAEN

tal spectrometer[9] was implemented. This records waveforms as well as performing advanced Digital Pulse Processing (DPP), including Pulse Height Analysis (PHA). The digitizer has eight input channels, and it is possible to make coincidence/anti-coincidence between the signals. The analysis is based on the CAEN Multi-PArameter Spectroscopy Software (CoMPASS), which supports data storage in ROOT format and also facilitates energy calibration and synchronization of multiple boards.

4.3   Design and Implementation of the Beam Chopper
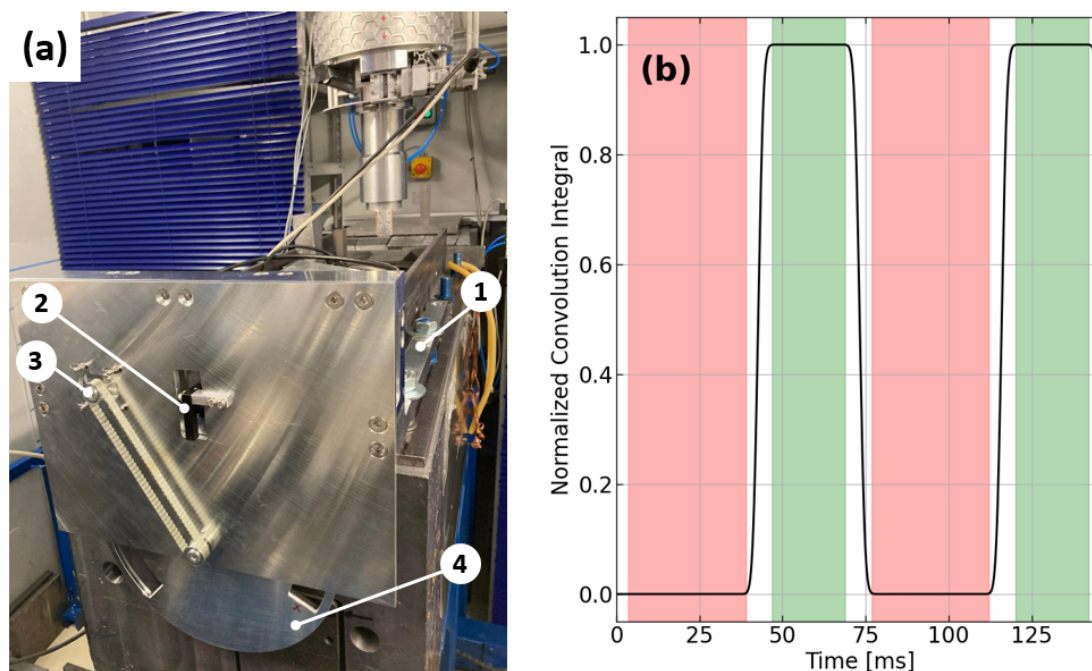
Figure 4.3.: (a) Beam chopper installed at the PGAA facility. The main parts are labeled: **(1)** neutron guide; **(2)** light barrier; **(3)** motor rotating the disc via a belt; **(4)** chopper disc in a closed state. **(b)** Normalized opening function of the chopper system [126]. The red area marks the closed states, where only the background is measured. The green area marks the open states, where the signal and background are measured at the same time. The function is a convolution of the beam profile with the chopper transition.

Reactions of the neutrons with the surroundings of the experimental setup and with the sample itself induce prompt γ radiation, as well as delayed β radiation (depending on the material). The delayed component is time-dependent and increases progressively to a saturation point during a measurement, varying with the composition of the sample matrix [52]. This radiation typically appears in the energy spectrum below a threshold value, where it increases exponentially at lower energies, *e.g.*, Co-Re at $\approx 1000\,\mathrm{keV}$ [127]. Although the N4DP instrument has a good signal-to-noise ratio, the measurements can significantly be improved by directly measuring the background. This can be achieved

---

[9]DT5730SB, CAEN

with a pulsed neutron beam produced, *e.g.*, by a chopper mechanism. In the frame of the bachelor thesis of J. Schlegel [126], such a chopper was designed and implemented at the PGAA facility.

The chopper is schematically shown in Fig. 4.1 after the neutron guide, and the picture of it is shown in Fig. 4.3a. It is located between the end of the neutron guide and the target chamber. A rotating disc with alternating point symmetric segments covered with B_4C[10] opens or closes the neutron beam. The thickness of the B_4C layer is 5.5 mm and was calculated to be sufficient to attenuate the beam intensity by 99.99 %. It was found that measuring 1.6 times longer in the closed state than in the open state optimally reduces the overall statistical error from the background by subtracting it from the signal. A motor[11] precisely maintains a rotation frequency of 7 Hz, and a light barrier[12] accurately determines the phase of the chopper. The normalized opening function over a full rotation is shown in Fig. 4.3b, illustrating two possible states: open and closed. During the open state, the signal and background are measured within the specified time interval. In the closed state, only the delayed background is measured.

4.4   DSSSD Implementation in the N4DP Instrument

We designed a new lid for the octagonal vacuum chamber of the N4DP to hold the front and mid-end electronics and the detector board. The lid has two KF40 ports for vacuum control and two further feedthroughs to support the two GEAR boards (as shown in Fig. 4.4). Special feed-through PCBs were designed to connect the signals through FFC cables[13] from the detectors in the chamber to the GEAR boards outside the chamber. A fork supports the detector PCB at a fixed distance $z \approx 105$ mm from the sample. For the camera obscura setup, a pinhole can be placed between the detector and the sample at variable distances using a movable holder fixed to the bottom of the chamber. For the coincidence setup, a second detector would be used on the other side of the sample without a pinhole at all.

Although no measurements could be made with the N4DP instrument due to the shutdown of the FRM II, it was nevertheless upgraded to include the detectors for four-dimensional profiling. First measurements are foreseen after the projected restart of the FRM II in 2025.
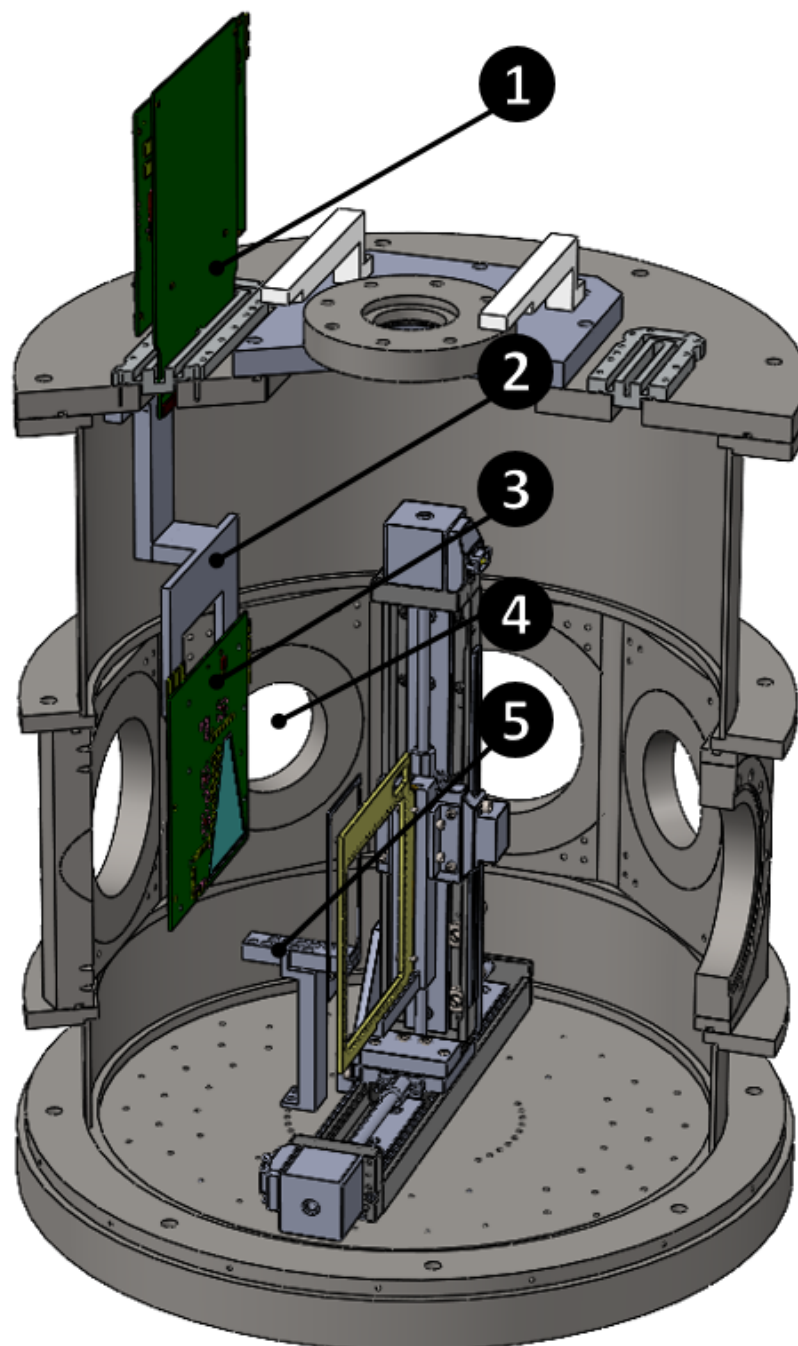
---

[10]The boron carbide was custom-made by SITUS Technicals GmbH.
[11]2-Phase-Hybrid-Stepper motor of the ZSS series with 200 steps
[12]Fork light barrier from Baumer AG
[13]part no. 686620200001, from Würth Elektronik GmbH&Co.KG

Figure 4.4.: Cut view of the N4DP chamber with the new lid. The main parts are the
following: **(1)** GEAR board; **(2)** fork for holding the detector; **(3)** detector
PCB; **(4)** neutron entry window; **(5)** pinhole holder. The second GEAR
board, the detector board, and the connecting cables are not shown.

Detector Characterization

This chapter focuses on the characterization of the new DSSSD and also introduces the further development of the multi-detector system. The characterization experiments were performed in the central technology laboratory (Zentrales Technologie Labor (ZTL)) of the physics department. Here, we produced the first 2-dimensional images, determined the energy resolution of all the pixels with a point-like α emitter, and investigated the temperature dependence of the system. With a modified setup, we determined the dead layer of the detector from both sides. In Sec. 5.2, we describe the upgrade of the system where we added a synchronization board to handle multiple detectors simultaneously, opening up possibilities for coincidence measurements. In a proton scattering experiment in Krakow, Poland, we successfully tested this upgraded system and developed the analysis tools for a multi-detector system.

5.1 Laboratory Setup with Radioactive Sources

Temperature Dependence

To characterize the detector performance, we used the weak radioactive point-like source of α particles described in Chap. 3. As already stated in Chap. 2, the surrounding temperature directly influences the signal, shifting the detected charges and changing the energy resolution non-linearly. The temperature values are collected from sensors[1], which are placed adjacent to the SKIROC chips on the opposite side of the detector PCB (as described in Chap. 3). Keeping the system at a constant low value of about 35°C is crucial for high-resolution NDP experiments. This temperature is constantly monitored, and in addition, one can calibrate the energy shifts for each pixel as a function of it: (1) linearly up to roughly 45°C and (2) non-linearly above that, as can be seen in Fig. 5.1a. Nonetheless, the resolution worsens with increasing temperature (as can be seen in Fig. 5.1b for the baseline), so it is important to keep it as low as possible during a measurement. We controlled the temperature by regulating the water (shown in Fig. 5.4) temperature with a chiller[2]. Figs. 5.1c,d show how the ADC values of the three α peaks directly correlate with the temperature. In Fig. 5.1d, we observe the temperature measured with one of the chips, showing the main influence from our cooling system and minor fluctuations from the surroundings (*e.g.* from the air conditioner used in the lab, etc.).
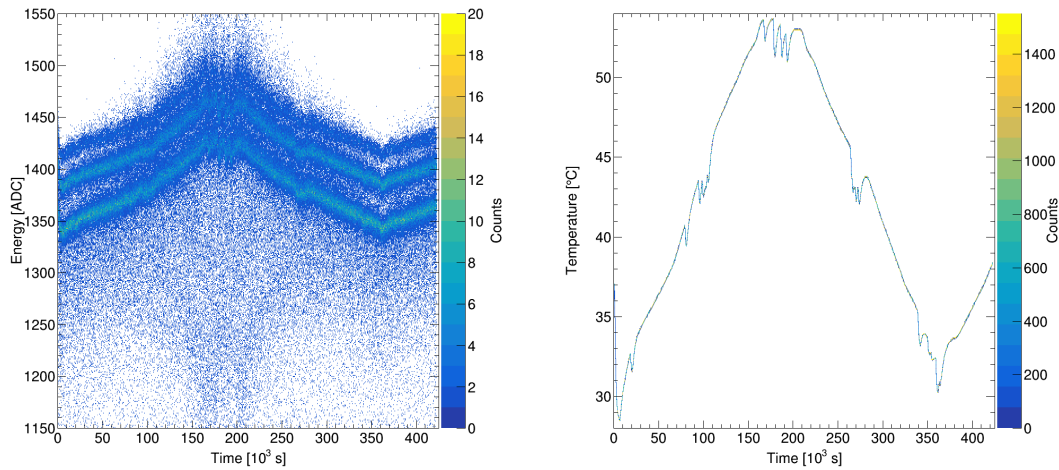
---

[1]TMP102AIDRLT from Texas Instruments
[2]CC-K6s from Huber Kältemaschinenbau GmbH
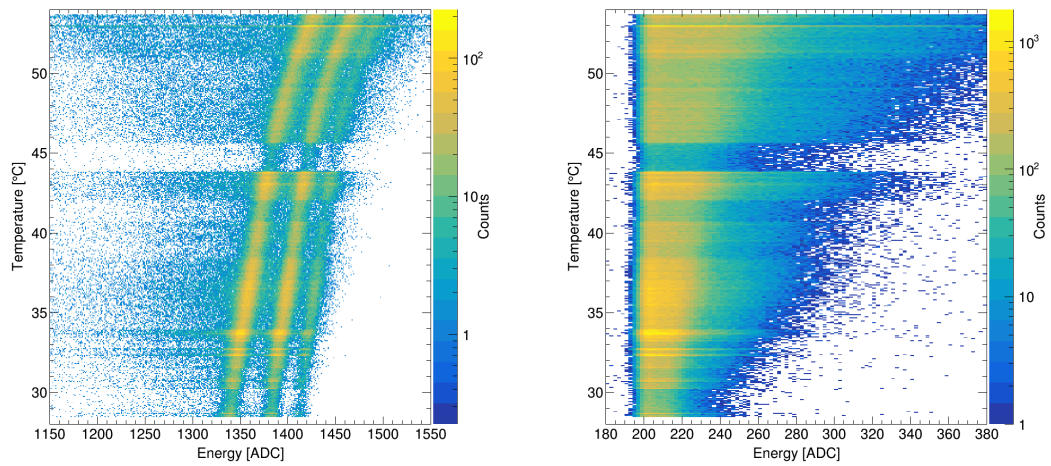
(a) Particle signal amplitude versus temperature of channel 47.

(b) Temperature dependence of the baseline of channel 47.

(c) Particle signal amplitude varying over time.

(d) Temperature varying over time.

Figure 5.1.: Influence of the temperature on the detector system. A shift can be observed for the three α energies in figure **(a)**. The mean signal amplitude and the width of the pedestal slightly shift and increase with temperature, as shown in figure **(b)**. For the temperature axis, a binning of 0.0625°C is used, matching the specification from the manufacturer of the temperature sensors. Figure **(c)** shows the three peaks varying over time, correlated to the temperature, which is plotted over time in figure **(d)**. The amplitude values are given units of ADC, as described below.

The shift of signal amplitude and resolution are specific to each readout channel of the SKIROC chip and need to be individually treated for any experiment. In this particular case, for channel 47 of the SKIROC 2A chip, the amplitude of the first peak shifted from $E_{28.5°C} = (1338.8 \pm 0.4)$ ADC to $E_{53.5°C} = (1428.8 \pm 0.6)$ ADC with its standard deviation increasing from $\sigma_{28.5°C} = (4.6 \pm 0.4)$ ADC to $\sigma_{53.5°C} = (8.3 \pm 0.7)$ ADC. This

shift in the mean amplitude value and an increase in the spread is also observed for the baseline.

Energy Calibration

Typically, NDP spectra are initially measured in an arbitrary unit, which is denoted in this work as ADC, just indicating the digitized signal amplitude of a certain channel. To obtain an absolute energy scale (usually in keV) from the measured amplitude in ADC channels for all the channels, an automatic calibration software was developed. This software is based on the TSpectrum class of the ROOT analysis framework [122]. It first automatically searches for the three main α peaks and one for the pedestal, whose center is supposed to be at $0\,\mathrm{keV}$. The algorithm assumes a Gaussian peak shape with a maximally linear dependant background [128]. It is based on the second difference $S_i = N_{i+1} - 2N_i + N_{i-1}$, with N_i representing the discrete count number of the channel i. Due to the discrete nature of the data, the second difference is used, which is equivalent to the second derivative. If we assume a maximally linear dependent background, we can express any data point as

$$N_i = G_i + B + C \cdot i = A \exp\left(-(i - i_0)^2/(2\sigma^2)\right) + B + C \cdot i, \qquad (5.1)$$

with B and C being some constants describing the background, and G_i representing a discrete Gaussian function, with A being its count number of the peak centered at channel i_0, and σ being the standard deviation, which is related to the width of the peak. By taking the second difference, the background is removed, and S_i is only different from zero in the presence of a peak. However, because the data is defined within a statistical error, S_i fluctuates around the expected value at i_0 according to the standard deviation. If the expected value is comparable to its standard deviation $F_i = \sqrt{N_{i+1} + 4N_i + N_{i-1}}$, we cannot perform a peak search [128]. By averaging (smoothing) the second difference, we can reduce its standard deviation. Then, we can establish an algorithm that automatically identifies peak positions by properly choosing parameters, such as average window size, the expected standard deviation of the peak, and a threshold that defines if it is a peak. More details on the automatic peak-search algorithm using the smoothed second difference are described in [128, 129].

After finding the peak values, the algorithm solves two sets of linear equations by Singular Value Decomposition (SVD) [130]. The two sets are: (1) the pedestal and the main peak of the ^{239}Pu, and (2) the same peak and the main peak of the ^{244}Cm. These two sets give us two sets of linear parameters to convert the ADC channel values into keV in each region. These parameters are then saved and applied to all channel values for all the pixels, ultimately leading to a calibrated spectrum. A calibrated spectrum for all p strips when using the α source is shown as an example in Fig. 5.2. To avoid steps on the channel-to-energy function, a random value between -0.5 and $+0.5$ must be added to the ADC value before we calibrate to keV.
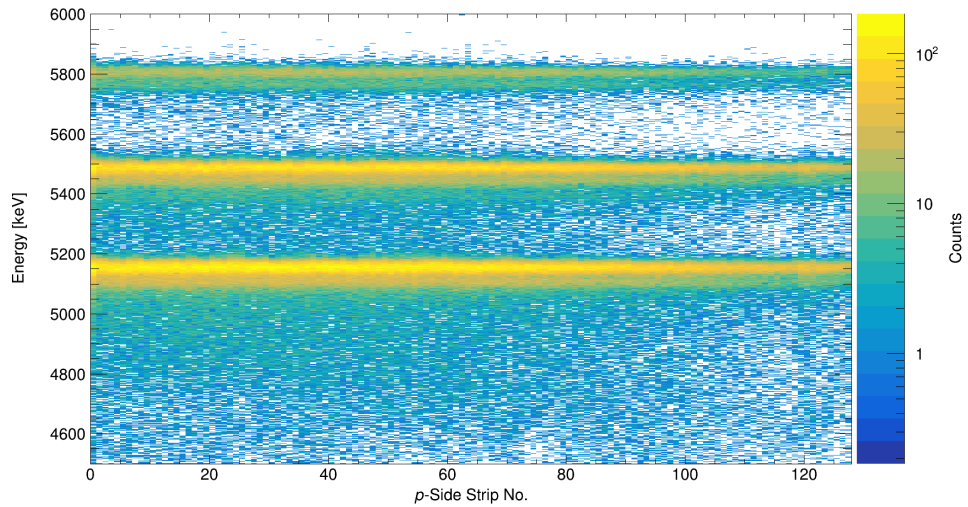
Figure 5.2.: Calibrated 2D spectrum showing calibrated energies of all *p* side channels. The three main α peaks and the weaker peaks (from decays to excited states, given in Tab. 3.1) can be observed. For this plot, only SCA number 0 was used.
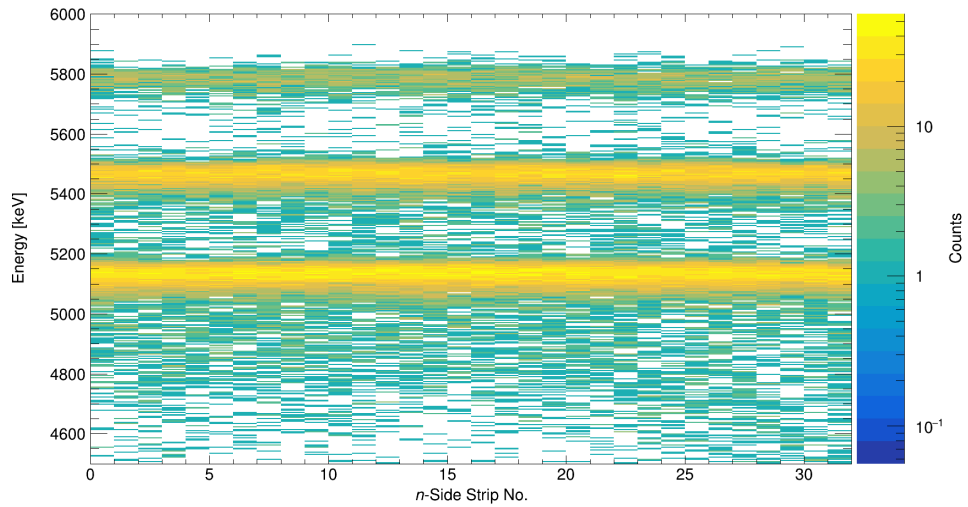

Figure 5.3.: Overview spectrum showing calibrated energies of all *n* side strips. The three main α peaks can be observed. The weaker lines are not separated anymore due to the worse energy resolution of the *n* side readout. For this plot, only the correlated events with a single *p* strip were used.

The same calibration procedure is applied for the *n* side as well, which is shown in Fig. 5.3. For the calibrated plots, we excluded events that show charge sharing between *p* strips and between *n* strips. We define charge sharing as if a second strip with a trigger has an energy value slightly but significantly above the pedestal ($\sim 300\,\mathrm{ADC}$).

To calibrate all detector channels, no mask was used between the detector and the α source in the setup shown in Fig. 5.4. For this measurement, the cooling temperature was kept constant at approximately $30°$C.

5.1.1   2D Imaging with a Point-Like Source
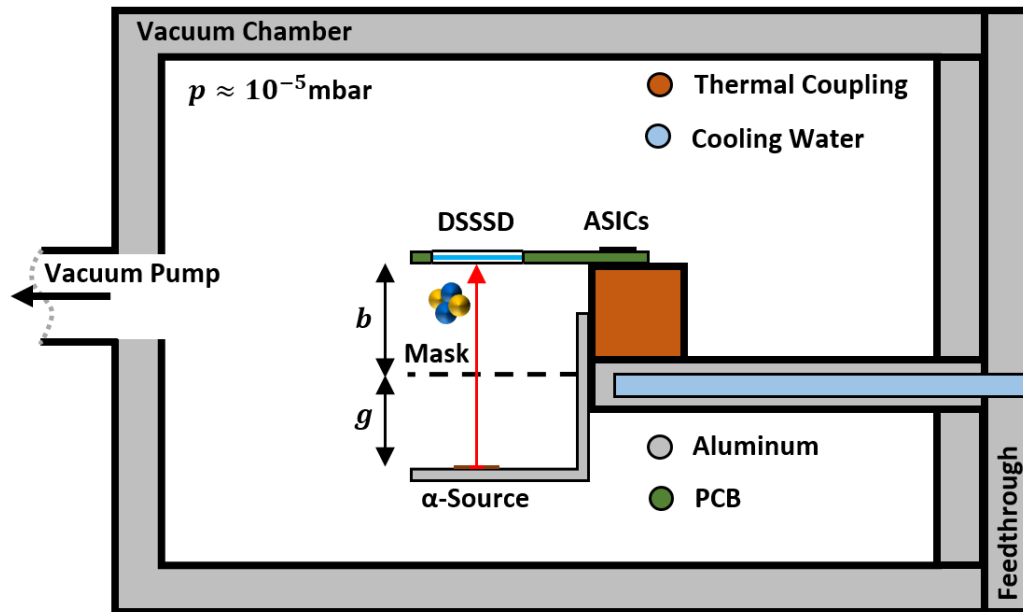
Figure 5.4.: Scheme of laboratory setup. The detector PCB is connected to a copper block, which provides thermal coupling. Circulating cooling water provides temperature stability to the SKIROC chips. The α source is placed under the detector at a distance of about 80 mm. Between the detector and the source, a patterned mask can be placed.

The experimental setup used to obtain 2D images is schematically shown in Fig. 5.4. A mask with a pattern[3] is placed between the point-like source and the detector [131]. The particles pass through this mask and arrive at the detector as a magnified picture of the pattern. We define the distance between the source and the mask as g and from the mask to the detector as b. If the pattern height is G and the picture on the detector is B, we can state without derivation that $B = (\frac{b}{g} + 1) \cdot G$ (intercept theorem [91]). If $b = 0$, the mask sits on top of the detector, and $B = G$. On the other hand, if the mask is very close to the source, *i.e.* $g = 0$, then the particles travel in all directions, and no picture is displayed on the detector. In our case, the α emitter was placed at a distance $d \approx 80$ mm from the detector, and $b/g \approx 0.5$.

---

[3]Masks made of stainless steel, laser cut by the company Becktronic GmbH

**(a)** Masks used for the inverse camera obscura method.
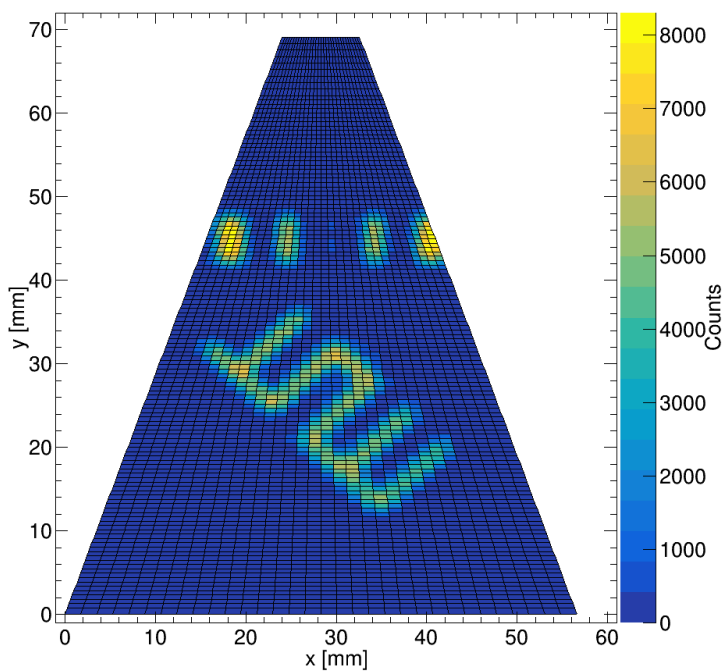
(b) 2D image of the TUM pattern.

Figure 5.5.: (a) Some simple masks were first tested for the correlation between p and
n strips of the detector, while the more complex, tilted TUM pattern with
stripes of different widths was used to show the capabilities of the detector.
(b) Using a "point-like" source and a mask between the detector and the
source, we obtain a magnified image of the pattern. Here, the n strips and
p strips are correlated to obtain the position information on the detector.

We observed that the rate from the α source is about $9\,s^{-1}$ when measuring with the tilted TUM mask (shown in Fig. 5.5a). Fig. 5.5b shows the detector image from this mask, which took about 4 days of measurement time. In the case of the regular intensity used at the PGAA facility, such a picture would be produced within minutes. A homogeneous distribution over the mask was observed, which is expected since the distance from the source to the mask is roughly the same for each point on the mask. We can see the stripe pattern from the mask, with the very thin (0.1-mm-wide) middle slit having few counts only. The tilted TUM pattern, with slit widths of about 1 mm, is certainly recognizable, with the intensity similar to those of the 1-mm-wide slits from above. On the detector, the image is roughly twice the size of the pattern on the mask, which agrees with the expected magnification. The blurred edges arise from the extended area ($\varnothing 5$ mm) of the source rather than being point-like.

5.1.2 Dead Layer Measurements
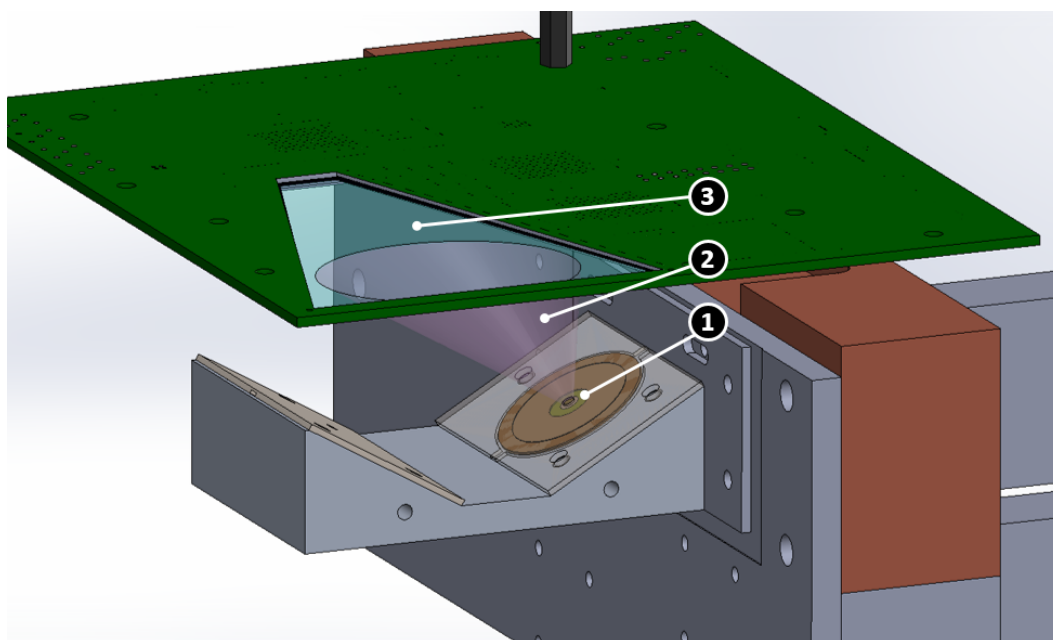
Figure 5.6.: CAD model of a laboratory setup for the dead layer measurements. The main parts of the CAD drawing are marked: **(1)** Collimated radioactive source; **(2)** Particle cone with $\theta = 60°$; **(3)** Detector area. 2 positions are used for the source for both sides: under n strip 4 or 28 and p strip 19 (strip 1 being the longest strip). From the geometry, the angle between the two n strips along the p strip 19 to the source is $60°$.

The dead layer of a semiconductor detector is very important for high-resolution spectroscopy for particles of low energies (see also Chap. 3). If the dead layer is non-uniform when detecting heavy ions, so-called satellite peaks may appear in the spectrum. These peaks are shifted from the main peak due to the non-uniformity of the dead layer. Furthermore, it is also important to keep the dead layer as thin as possible

to minimize energy straggling. In this section, we estimate the thickness of the dead layer from both sides of the detector and check its uniformity using a modified setup shown in Fig. 5.6.

We determined the dead layer of the DSSSD by measuring the energy loss of the alpha particles at different angles to the detector. For this, a new support for the α emitter was manufactured. The source was placed at an angle of 30°, so the energy loss through its active area is minimized overall for all the strips. Furthermore, the radioactive source was further collimated by a 2 mm pinhole placed on top, reducing the diameter of the active area. The temperature was kept constant at 33°C.
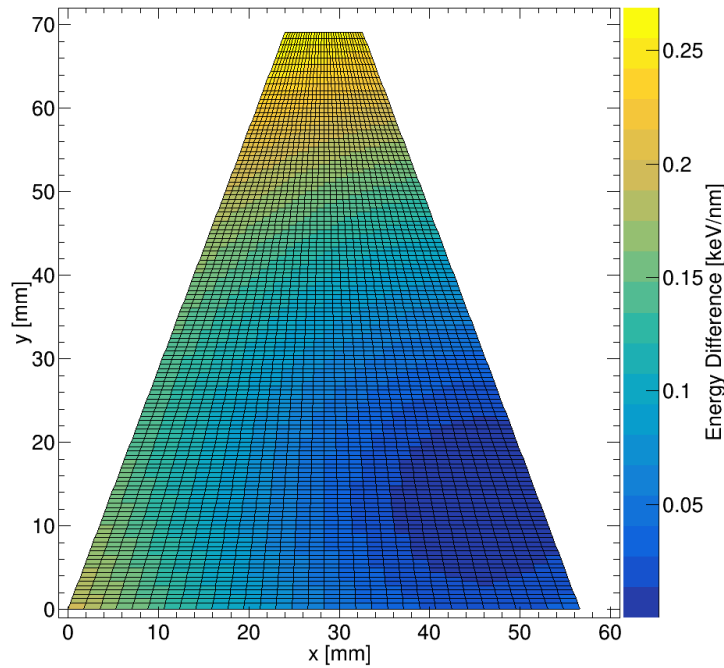
Figure 5.7.: Calculated average energy loss per SiO_2 dead layer thickness. A smooth energy loss function is expected for a homogeneous dead layer. The radioactive source is located in the center of the dark blue area.

Calculations were performed based on the geometry to estimate the expected energy loss for each pixel of the detector. For these, we compared two pixels at different angles. We calculated the average energy loss from the angle θ between the source and any pixel, which results in an increased effective thickness of $d_{dead}/\cos\theta$. Uncertainties arise from the width of the pixels and from the source collimation. The energy loss in SiO_2[4] of the α particles at energies around 5.5 MeV is $dE/dx^{\alpha}_{SiO_2} \approx 0.15$ keV/nm. The radioactive source was placed under the n strip number 29 (counting from the left-hand side of the detector) and under the p strip number 19 (counting from the major side). The calibrated energy in this particular pixel is used as a reference for all
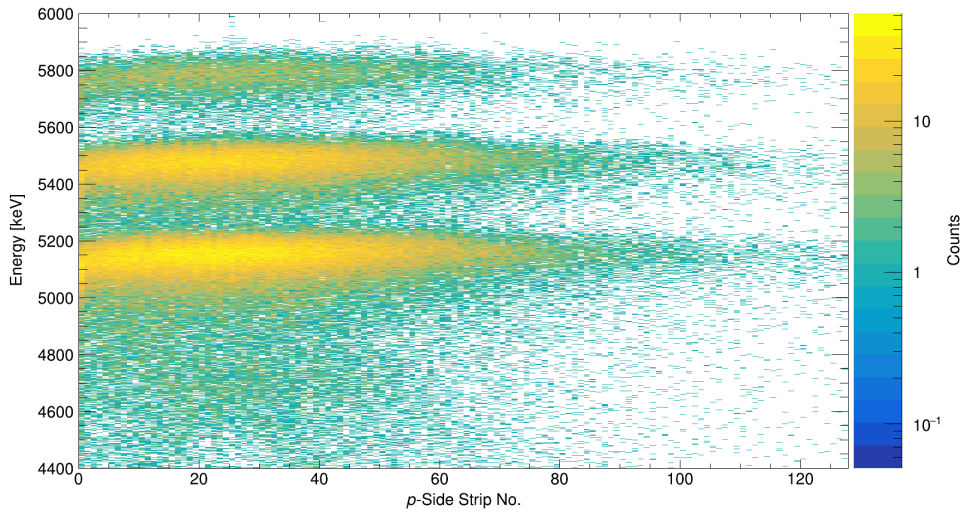
---

[4]Value taken from WebAtima tool [132], calculated with the density $\rho_{SiO_2} = 2.65$ g/cm^3

the other pixels with $\theta = 0°$. Fig. 5.7 shows the expected energy loss difference (given in keV/nm) for the entire detector.
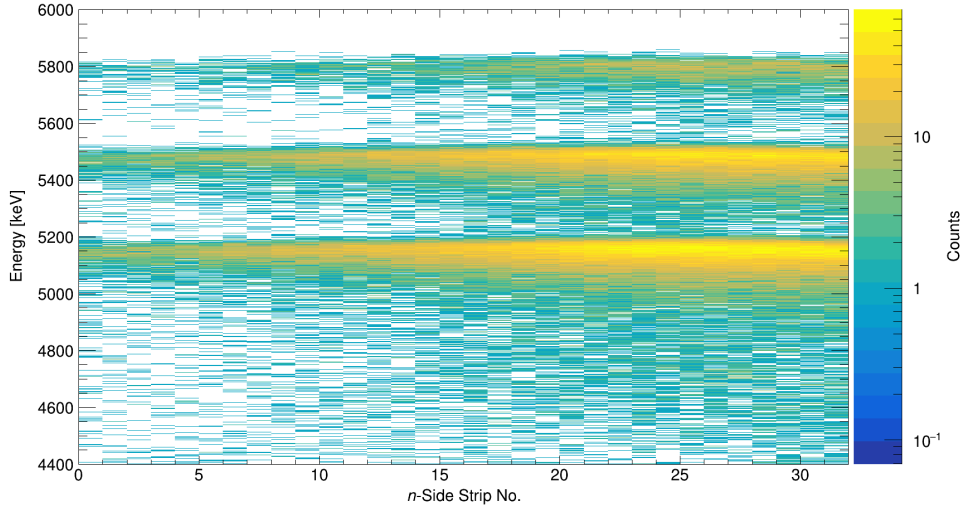
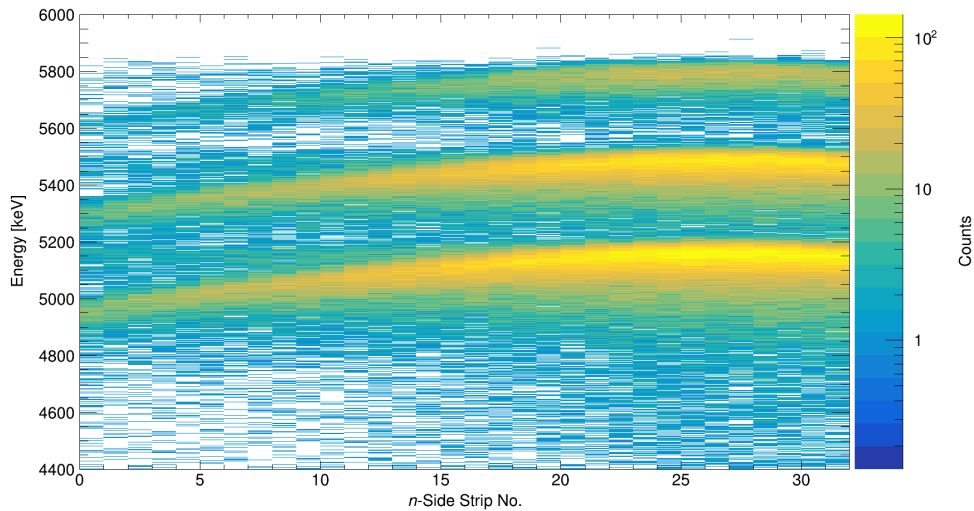**(a)** Calibrated energies of p strip number 19 in coincidence with all n strips.

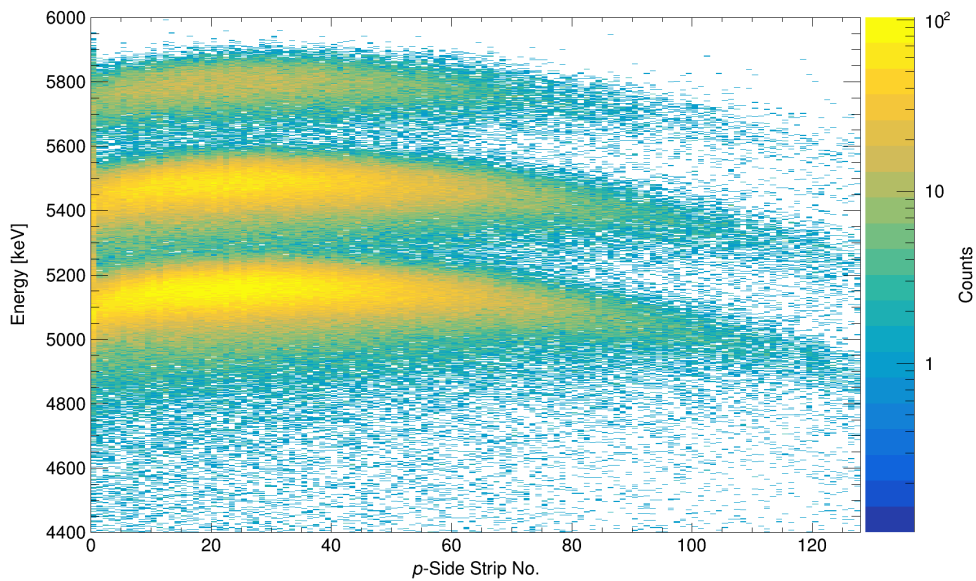**(b)** Calibrated energies of n strip number 29 in coincidence with all p strips.

Figure 5.8.: Calibrated spectra of the α source for a single p and a single n strips in coincidence with the other side and the source facing the p side. The dead layer on this side is expected to be very thin. We observe this as a result of a very slight bend of the three peak positions. The energy difference of the second peak at $\theta = 60°$ is around 16.5 keV, which corresponds to a total dead layer thickness of $d_{\text{dead},p} \approx 110$ nm.

We need to calibrate all the pixels correctly with reference to the pixel mentioned above. For the reference pixel, we set the energies of the three main peaks to the values given

in Tab. 3.1. If we examine single p and n strips, we obtain Figs. 5.8a,b when the source faces the p side, and Figs. 5.9a,b when it faces the n side.

(a) Calibrated energies of p strip number 19 in coincidence with all n strips.

(b) Calibrated energies of n strip number 29 in coincidence with all p strips.

Figure 5.9.: Calibrated spectra of the α source for a single p and a single n strips in coincidence with the other side and the source facing the n side. As a result of a thicker dead layer from the n side, a strong bend of the three peak positions is observed. At $\theta = 60°$, the energy of the second peak is at ~ 5330 keV. The difference to the peak at $\alpha = 0°$ is ~ 156 keV, which corresponds to a total dead layer thickness of $d_{\mathrm{dead},n} \approx 1.04$ μm.

We calculate the thickness of the dead layers from both sides by looking at the energy differences at pixels under the n strips 4 and 29 and under p strip number 19, with the angle between these two pixels of $\theta = 60°$. If we look at the main α peak from ^{241}Am at $\sim 5.5\,$MeV, we observe an energy difference of $\Delta E_p \approx 16.5\,$keV when the source faces the p side, and $\Delta E_n \approx 156\,$keV when the source faces the n side. These values correspond to the dead layer thicknesses of: $d_{\text{dead},p} \approx 110\,$nm and $d_{\text{dead},n} \approx 1040\,$nm. These values are in agreement with the expected values, which are $\sim 150\,$nm for the p side and $\sim 1000\,$nm for the n side, as mentioned in the thesis of C. Berner [97], in which the author started the design of these detectors.

Similar images are observed for all the p and n strips across the detector. From the smoothness of the bending of the three peak positions on both sides, we can conclude that the dead layer is uniformly distributed, which enables high-resolution measurements. The first p strip correlated with any n strip (shown in Figs. 5.8b and 5.9b) has a broader distribution due to its larger area (3 strips being bonded together), which does not overlap with the n strips but with the meander resistors of the detector on the n side.

We have shown in this section that single detectors can work with the SKIROC-based electronics, allowing for 2D imaging. Now that we understand the various influences on the system and have experimentally determined the dead layer, the next step is to implement multiple detectors in the system to enable coincidence measurements.

5.2   Coincidence Measurements with Protons

In a proton scattering experiment on fixed targets with incoming proton energies of $(80 - 200)\,$MeV, carried out at the Bronowice Cyclotron Centre in Krakow, Poland, we tested our detection system using different clocks from multiple GEAR boards. A significant result of this experiment was the successful reconstruction of coincident events using a new setup - which, for the first time, included multiple detectors. We compared the measured angular distributions of elastic proton-proton scattering and the (p,2p) Quasi-Free-Scattering (QFS)[5] reaction with scattering simulations, highlighting the relativistic kinematics of such reactions. We also obtained the first multi-detector coincidence images, allowing us to synchronize several detectors. This prepares our system for further coincidence measurements in NDP, as introduced in Chap. 2. An important result of this experiment was understanding the energy dependence of the detection efficiency on the energy threshold, count rate, and other SKIROC parameters.

5.2.1   (p,2p) Simulations

The reaction mechanism of proton-induced single-nucleon knockout at relativistic energies is mainly dominated by the quasi-free proton-nucleon scattering process,

---

[5]First observations of quasi-free-scattering reactions were made by Emilio Segrè and Owen Chamberlain [133].

denoted as (p,2p) or (p,pn) [134]. QFS reactions are typically used as a tool to study the structure of nuclei. The main physics involved in these types of reactions are summarized in [135]. The geometry of such reactions is shown in Fig. 5.10, highlighting the angles in the target plane. The opening angle θ_{op} in the laboratory system of the outgoing proton pair can be expressed as:

$$\theta_{op} = \sin\theta_1 \sin\theta_2 \cos(\phi_2 - \phi_1) + \cos\theta_1 \cos\theta_2 , \tag{5.2}$$

where θ_i is the polar angle of the i-th proton with respect to the z axis, and ϕ_i the azimuth angle relative to the x axis in the projection plane.
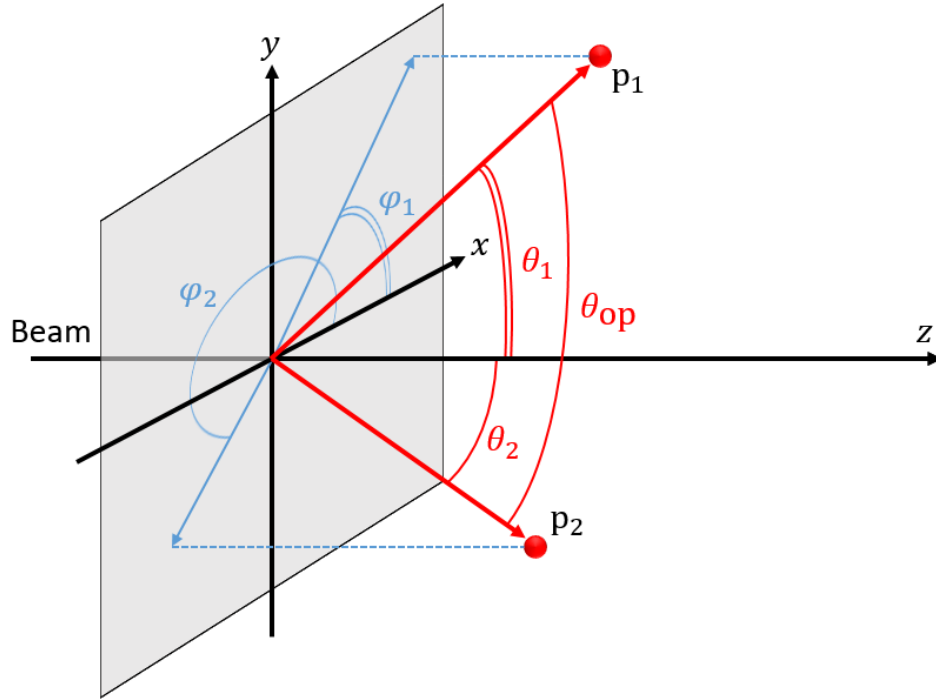
Figure 5.10.: Geometry of a (p,2p) reaction. The protons leave the origin of the reaction with an opening angle θ_{op}. The figure is reconstructed from [134].

We simulated the angular distribution of the opening angle of the (p,2p) reactions in CH_2, shown in Fig. 5.11. For the simulation of the relativistic kinematics of QFS reactions, the event generator for the R3B experiment from Panin *et al.* [135] (R3BROOT generator [136]) was used. If not mentioned otherwise, each simulated data set contains 10^5 events. There are two contributions from a polypropylene target (see Sec. 5.2.2) to the opening angle. The first one (shown in Fig. 5.11a) originates from the QFS reaction of a proton with the carbon target nucleus, in which one proton from the carbon nuclide is knocked out. Due to the non-zero internal momentum of the proton inside the band system of a nucleus, the calculated angle shows a rather wide distribution from $0° - 180°$, with its maximum at $\sim 89°$. The second and main contribution (shown in Fig. 5.11b) comes from the free scattering of the protons on the hydrogen nuclei, producing a peak at $\sim 88.7°$ with a tail toward $90°$. Because the relativistic mass of the

incoming proton is larger than the mass of the almost motionless hydrogen atom, the average opening angle between the protons is smaller than $90°$. This relativistic effect is lower if one of the polar angles θ_i goes to $0°$, and therefore we observe the tail toward $90°$.


(a) Carbon simulation.   **(b)** Hydrogen simulation.
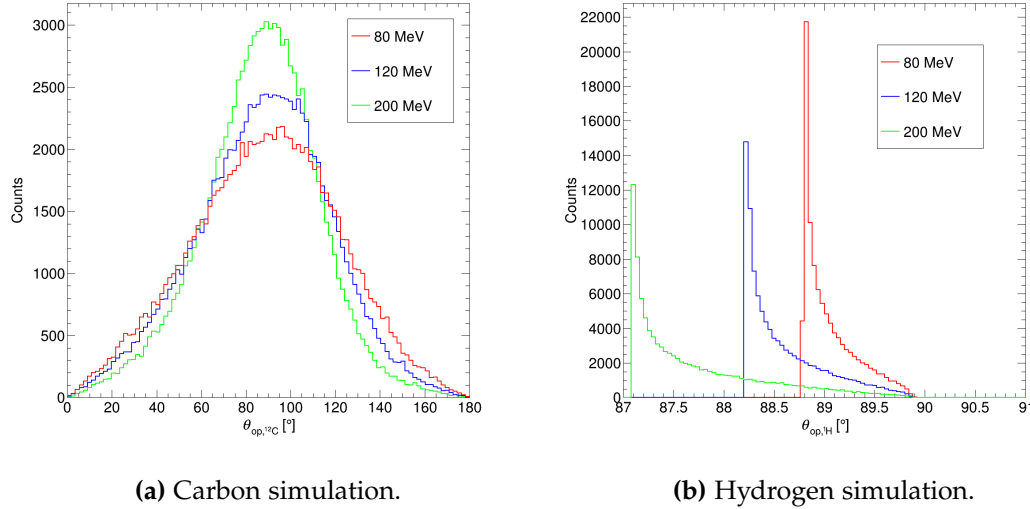
Figure 5.11.: Simulated opening angles of scattered protons on a CH_2 target at different beam energies. The combination of the two gives the expected opening angle distribution, where the rather narrow contribution is from the hydrogen shown in **(b)** while the carbon shown in **(a)** creates a rather broad signal.

5.2.2 Experimental Setup

A 3D CAD design of the experimental setup is shown in Fig. 5.12. In a two-arm geometry setup, we placed four detectors, two on each arm, at an angle of $45°$ w.r.t. the beam line. We denote the detectors on the left arm (looking from the beam direction) as detectors 1 and 2 (back and front, respectively) and on the right arm as 3 and 4 (see Fig. 5.12. The entire setup was enclosed within an aluminum hexagonal box, separating the electronics and detectors from external light and electromagnetic influences from the environment. On the top lid of the chamber, we mounted six feedthroughs for six GEAR boards, four of which we used and two as spare parts. Four LEMO connectors were installed for each detector system for the HV supply and signal testing of the electronics. Behind the chamber, we placed two blocks of CsI scintillators to measure the remaining scattered proton energy and to have a redundant system for synchronization. We included in the DAQ system a new board (described in Sec. 3.2) to distribute a synchronization signal to all GEAR boards. The modified scheme of the DAQ, including multiple detectors, is shown in Fig. 5.13. For the synchronization signal, we used the readout signal of one of the detectors, which we denoted as the master, while the others were denoted as slaves. Whenever the master board is read out, this synchronization signal is updated for all boards. To correlate the data from different detectors, we then

need to adjust the trigger times of each slave board. The time difference originates from the clock drifts of the different FPGA clocks used in the GEAR boards. With this system upgrade, we can correlate events in different detectors by matching the trigger times. In our experiment, we used detector three as the master board.

As a target, we used either a single string or multiple vertical strings of polypropylene[6] $(C_3H_6)_n$ fibers with a diameter of 0.5 mm. We glued the strings on aluminum frames, which were fixed on a sample holder (as shown in Fig. 5.14). The proton beam height was fixed at ≈ 4 cm from the bottom of the detectors so that it is positioned roughly at the center of gravity of the active area of the detectors.
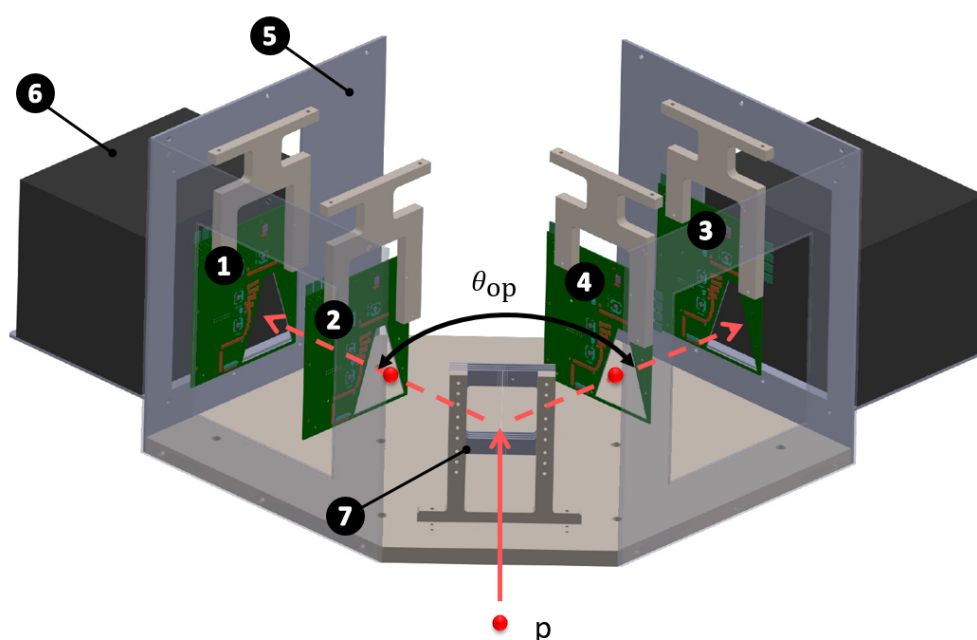

Figure 5.12.: CAD model of the experimental setup. Main parts are labeled: **(1-4)** detector number 1-4; **(5)** the hexagonal chamber; **(6)** scintillators; **(7)** target holder. A proton scatters off the polypropylene target, resulting in two outgoing protons with an opening angle θ_{op}. The two detector arms with two detectors each are arranged at 90° for the determination of the angles and the energies of the protons. Behind the chamber, the two scintillators measure the remaining energy of the protons.

---

[6]S 235 security threads from Württembergische Allplastik GmbH
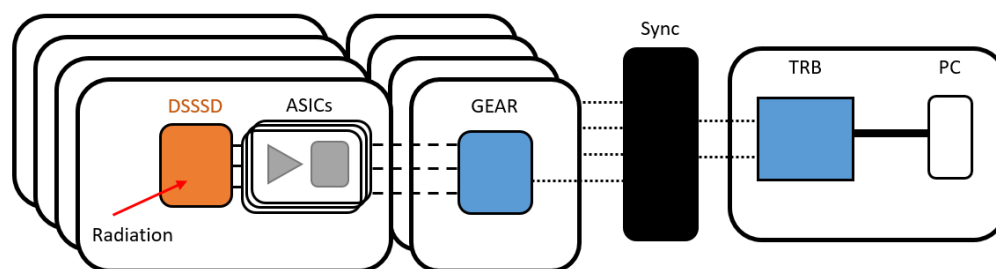
Figure 5.13.: Scheme of the modified DAQ including multiple detectors. The scheme is similar to the one used in Fig. 3.7, but it contains an additional board to synchronize the clocks. The additional board can synchronize up to 16 GEAR boards.
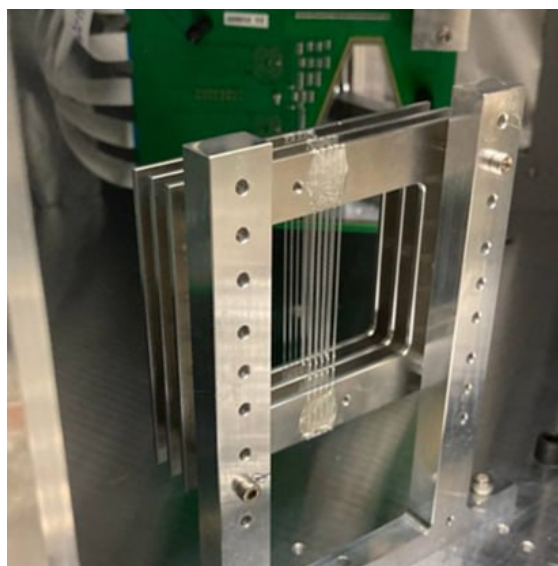
Figure 5.14.: Target with multiple strings. The strings are streched on aluminum frames, while the frames are fixed on the holder.

5.2.3 Signal Analysis

The incoming proton beam had energies of $80, 120,$ or $200\,\text{MeV}$. After the reaction on the sample, we expect from the energy and momentum conservation that the average energy of the two outgoing protons is roughly half the incoming energy. From these energies, we determined the energy loss in the 150-μm-thick Si detector, which are $410, 298,$ and $203\,\text{keV}$, respectively[7]. Measuring such low energies with our system is challenging since the preamplifiers need to be tuned to very large gains. Due to fluctuations in the energy loss from the ionization of charged particles in thin films, the energy profile is described by the Landau distribution [137], a skewed function

---

[7]Using the WebAtima - Energy Loss Calculator [132], mainly based on the Bethe-Bloch formula

with a tail toward higher energies. The main source of the Landau fluctuations is the δ electrons, which have enough energy from the interaction to become ionizing particles themselves.

From the energy measured on the p and n sides of a detector, we obtain the pictures shown in Fig. 5.15. Only plots from 80 MeV proton beam are shown, and for completeness, similar plots for the other beam energies can be found in Appendix C. Two graphs are compared to highlight the way the data acquisition works: one is non-filtered, and the other is filtered. In the non-filtered data (shown in Fig. 5.15a), we observe the baseline of all channels with no hit at ~ 300 ADC. This corresponds to the CMS chip events triggered at the same time as the SKIROC 2A chip. To filter these events out, we find the channel in the CMS chip with the two highest energy values and set their difference higher than the baseline, *e.g.* 3σ of the baseline.

(a) Non-filtered.   **(b)** Filtered.
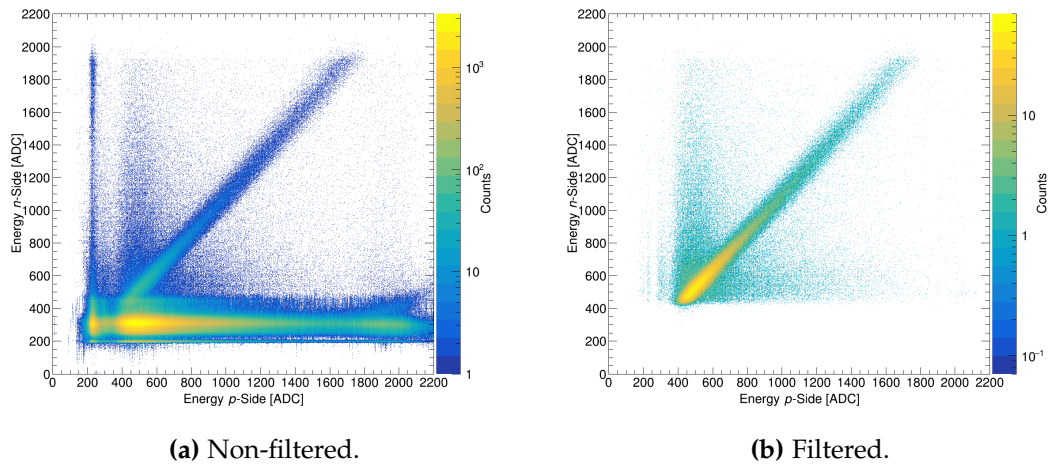
Figure 5.15.: Events from the 80 MeV-proton beam in detector 3 correlated within its p and n sides. Only data from one SKIROC 2A chip was used here. The x axis represents the energy on the p side, while the y axis represents the n side. On the diagonal, we observe the Landau distribution from the proton's energy loss. In **(a)** we observe several features: the pedestal from the n side at ~ 300 ADC, the pedestal from the p side at ~ 200 ADC, and a non-linear behaviour at amplitudes above 2000 ADC. In **(b)**, all these events are filtered out, as described in the text.

For this experiment, we tuned the preamplifier in such a way that the energy values did not exceed the 2000 ADC threshold. Above this value, the SKIROCs behave non-linearly (as can be seen in the plots in the Appendix C). At the same time, it is important not to set the preamplifier too low. Otherwise, the protons' signal disappears in the pedestal, making it impossible to identify them. One last filter used in Fig. 5.15b is a cross-talk filter on the p side. If there are multiple triggers on the p side for one event, they are discarded. This can happen whenever a proton passes through neighboring p strips. For the n side, the filter used above also acts as a cross-talk filter since only the highest value is used.

### 5.2.4 Multi-Detector Correlation

With the synchronization board, we can correlate events from the different detectors. In this experiment, we had four detectors. The two front detectors were roughly two times closer to the target than the two in the back and, therefore, had event rates roughly four times higher. Most of the time, these two detectors were saturated at the maximum rate due to the high read-out of the ASICs, while the back detectors collected useful data. Due to the non-synchronized dead time and readout of the detectors, and an incident rate of $r > \frac{1}{t_{\text{readout}}}$ little to no correlated data was found between both the two front detectors, and front and back detectors. If we nevertheless correlate events in detectors 1 and 3, we obtain Figs. 5.16a,b. In these graphs, the horizontal strips (p side) and vertical strips (n side) of both detectors are plotted against each other.
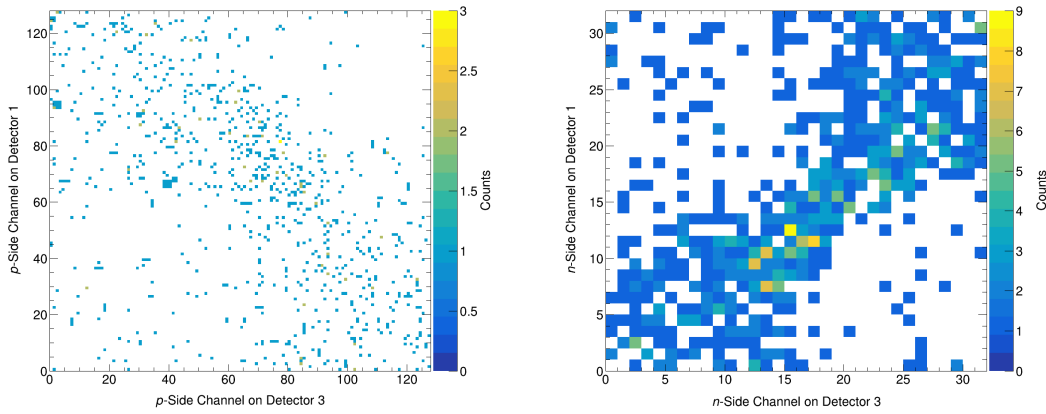
(a) Anti-correlation between the p strips of detectors 1 and 3.

(b) Correlation between the n strips of detectors 1 and 3.

Figure 5.16.: Two detector coincidence. For the p strips in **(a)**, we obtain an anti-correlation, and for the n strips in **(b)**, a correlation. This is expected from the angle constraint of the scattering reaction on the hydrogen atoms at $\sim 88°$. For these figures, only a single string was used as a target.

From these coincident events and the known geometry, we can calculate the opening angle θ_{op} between the two protons and the y position on the sample (measured from the bottom of the detector). These are shown in Figs. 5.17a,b. For these, we made the assumption that the origin of the reaction is roughly halfway between the two pixels. The angle distribution matches the expectation from the simulations in Figs. 5.11a,b. We observe a sharp peak at $\sim 88.5°$ from the scattering on hydrogen and a broader distribution from the knock-out of the proton from the carbon nucleus. Furthermore, the calculated y position matches with the expected beam height of roughly $4\,\text{cm}$.

(a) Calculated angle.   **(b)** Calculated y position.
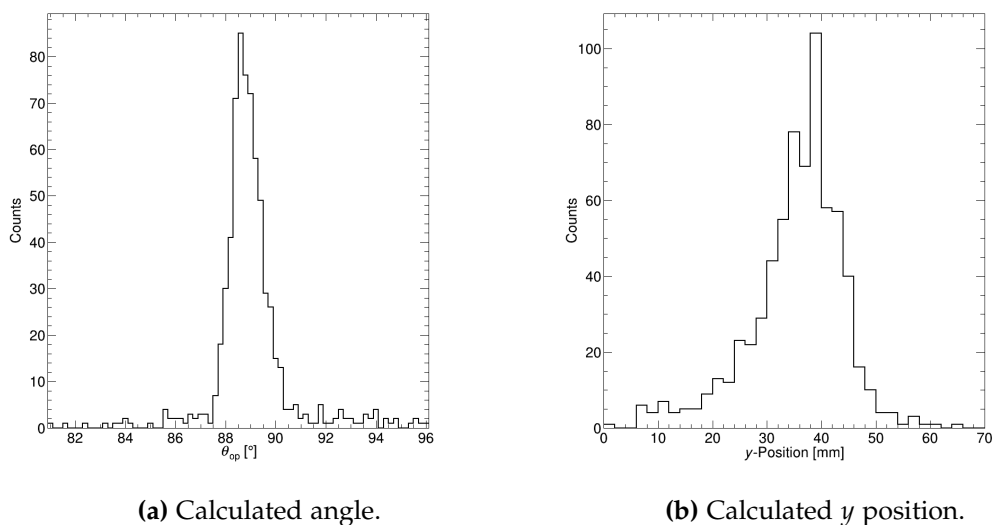
Figure 5.17.: (a) Opening angle between the coincident events between detectors 1 and 3 calculated from the known geometry and the pixels hit. **(b)** y position of the event's origin, measured for the same events.

Despite the event rate in the experiment being too large, we still showed the ability of our system to work with multiple detectors, allowing for coincidence measurements in NDP. Throughout the experiment, we improved our electronic settings, which triggered continuously in one particular channel if the threshold was too low. With this knowledge, we can now measure four-dimensional depth profiles from NDP reactions.

Neutron Depth Profiling at RID

In this chapter, we discuss the first NDP measurements with the new highly segmented detector modules and the corresponding full readout chain at the Reactor Institute Delft (RID) of the University of Technology in Delft, the Netherlands. The aim of this measurement was to test the methods for lateral mapping, benchmark the resolution of our system, and, at the same time, measure batteries *ex situ* and investigate a coded mask method. The latter two points are discussed in Chap. 7 in the outlook section. Major results from this measurement campaign have been published in [90].

At the RID, a thermal neutron beam with a wavelength maximum at $\lambda_{\mathrm{peak}} \approx 1.8\,\text{Å}$ (shown in Fig. 6.1) and a flux density of $\Phi \approx 1.0 \times 10^7\,\text{cm}^{-2}\text{s}^{-1}$ was available for our experiments.
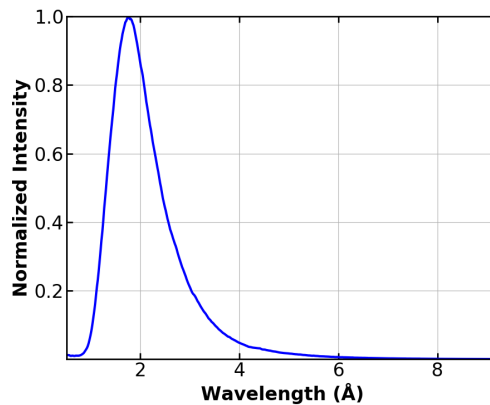
Figure 6.1.: Normalized intensity of the neutron beam versus the wavelength at the RID. The spectrum was measured and kindly made available by J. Plomp from the TU Delft.

6.1 Setup Configuration and Samples

For this experiment, the Delft team provided us with a cube-shaped vacuum chamber (shown in Figs. 6.2a,b) with an inner volume of $(19 \times 19 \times 110)\,\text{cm}^3$ and a vacuum pressure of $\approx 5 \cdot 10^{-3}\,\text{mbar}$. Inside the chamber, we placed a rectangular aperture to cut the already collimated neutron beam to the size of $20 \times 30\,\text{mm}^2$ at a distance of $\approx 50\,\text{cm}$ upstream of our sample (shown in Fig. 6.2a). To avoid any vibration effects on the detectors, the vacuum pump was connected via a long bellow, which was mechanically fixed to the massive table construction at several points.
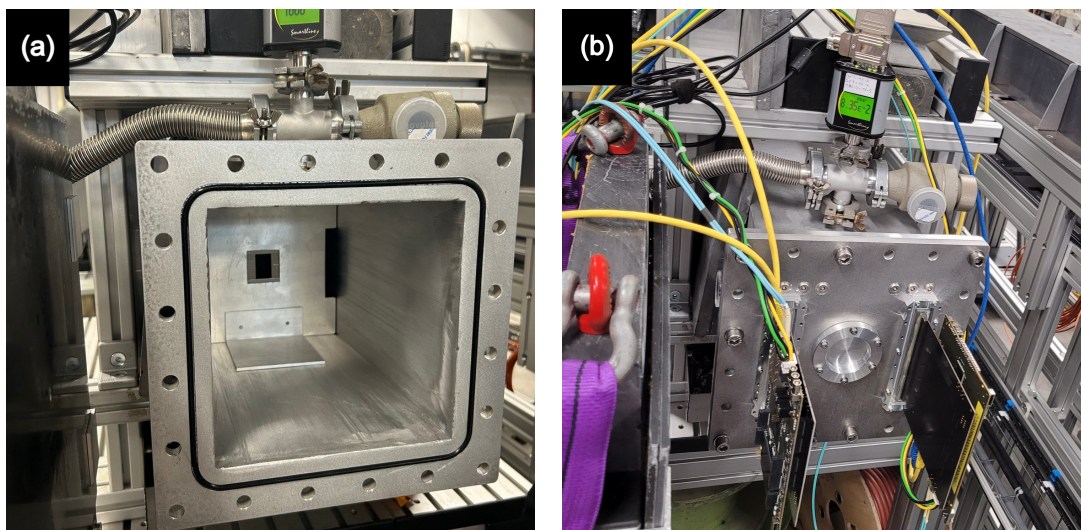
Figure 6.2.: (a) Open chamber with the aperture with the size of $2 \times 3\,\text{cm}^2$ at a distance $\sim 50\,\text{cm}$ from the lid. **(b)** Closed chamber lid with GEAR boards mounted on top of the feedthroughs and connected cables.

To feed through the signals, we designed a modified square-shaped end flange of the chamber[1] to support two GEAR boards and six vacuum-tight LEMO-connectors[2]. The GEAR boards were placed on custom-made feedthrough PCBs (shown in Fig. 6.2b). We glued[3] these boards to vacuum-tight aluminum supports. The flange was equipped with a 1-mm-thin aluminum exit window to minimize the background from neutron-induced β^- radiation from the material. We placed a lead tower with boron carbide plates as a neutron beam stop after the exit and lead blocks surrounding the chamber as shielding.

Inside the chamber, we placed an aluminum support, which was connected through thermal pads[4] to the flange for better heat conduction. We cooled the flange with an outside air fan, maintaining a reasonably constant temperature ($\pm 1 \circ \text{C}$) for the PCBs and their readout electronics. The two detectors were fixed on the aluminum structure through the same heat-conducting pads, which also served as spacers and electric insulation (barely seen in Fig. 6.3a).

We denote detector number 1 as the one on the right side (looking in beam direction) in Figs. 6.3a,b, which was placed behind a pinhole aperture for the camera obscura measurement. This aperture was a 100-μm-thick aluminum plate, with hole diameters of either 1 or 2 mm. These two diameters result in a different resolution, as described in Sec. 4.1. Behind this detector, we mounted a thicker ($\sim 700\,\mu$m) unsegmented Si detector. In the frame of the bachelor thesis of L. Ziegele [138], this thicker detector was tested, and the background radiation, coming from the β^- particles penetrating the first DSSSD, was also investigated.

---

[1]Constructed by the Delft team
[2]LEMO SWH.00.250.NTMV
[3]Two Component Epoxy UHU Endfest
[4]2617837 - Thermal pad from Tru Components
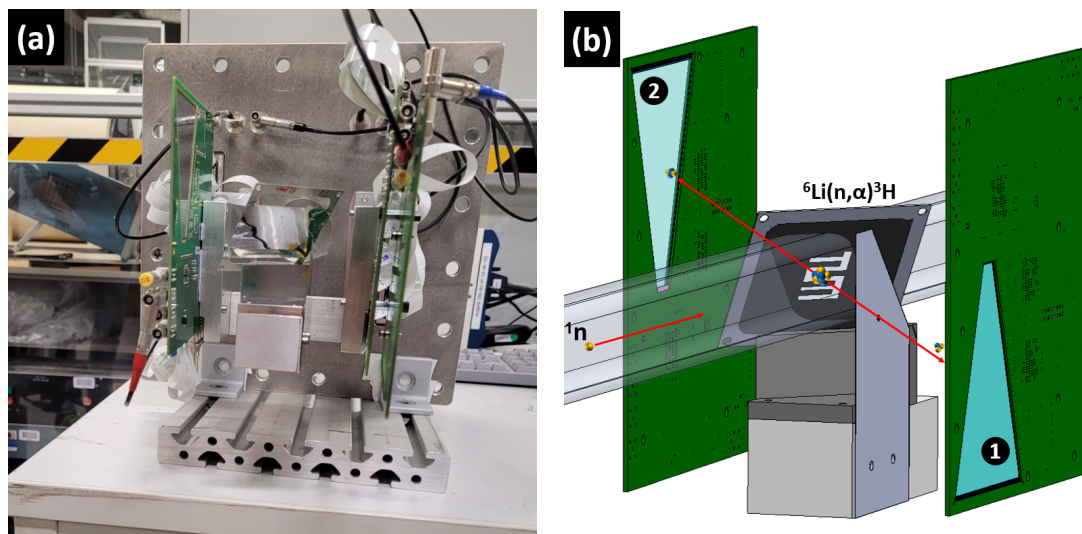
Figure 6.3.: (a) Front view of the setup. In the center of the setup, one can see the tilted sample fixed on an aluminum support arm. On the right-hand side (looking in the beam direction), the DSSSD number 1 is mounted in front of another unsegmented detector. For the camera obscura measurement, we placed a pinhole aperture between the sample and detector 1. On the left side, DSSSD number 2 is mounted on the aluminum support, also spaced by a thin thermal pad. **(b)** CAD drawing of the setup. The neutron beam is denoted as ^{1}n, hitting the ^{6}Li target.

The detector 2 can be seen on the left in Figs. 6.3a,b. Due to spatial constraints, it was placed in the chamber mirrored around the target center. No aperture was used for this detector. Due to the mirroring, the coordinate systems on the detectors are different. For the coincidence method, no aperture was installed between the detectors.

Samples

For the samples, we vapor deposited highly enriched lithium fluoride ($\sim 99\,\%$ ^{6}LiF) evaporated by an electron gun from a point source onto Mylar foils with the thickness of $5\,\mu$m through different masks[5] (shown in Fig. 6.4a). These were attached to aluminum frames, as shown in Fig. 6.4b). We used one of the four masks with different mass layers (measured with a detector during the deposition process) on either side of two Mylar foils, as listed in Tab. 6.1.

We mounted the sample frame at the center of the aluminum support. It is tilted at an angle of $45°$ w.r.t. the neutron beam and $56°$ around the beam axis to face the detectors. This increased the effective target thickness by a factor of $\sqrt{2}$. For the camera obscura method, we added a pinhole on one side of the sample at a distance of $g \approx 19\,$mm. The distance from the aperture to the detector was $b \approx 37\,$mm, giving a total distance from the center of the target to the detector of $z = g + b \approx 56.0\,$mm. The sample size is abbreviated with G, and the image size is B. The average geometric ratio for the

---

[5]$100\,\mu$m stainless steel laser cut by Becktronic GmbH
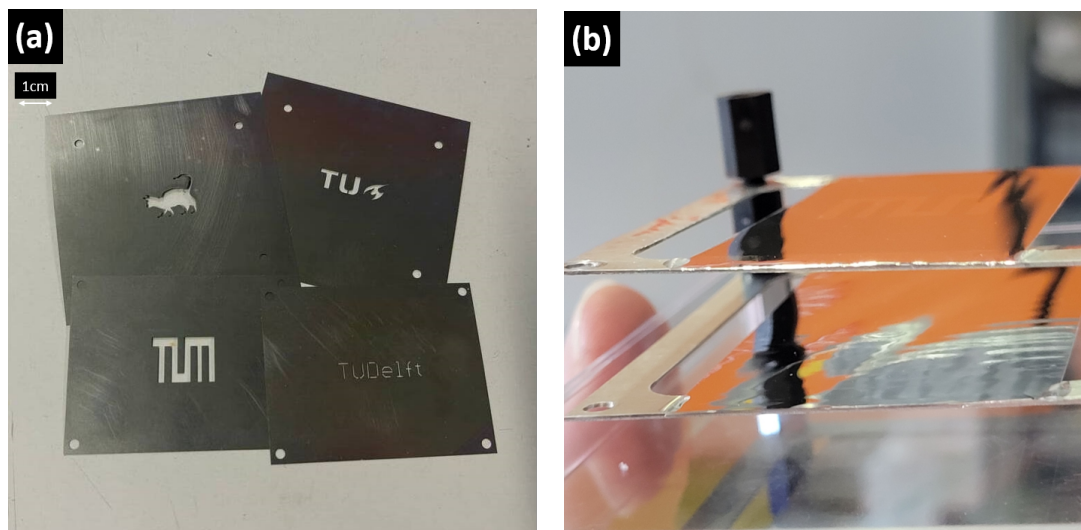
Figure 6.4.: (a) 100-μm-thick laser cut masks with different patterns. **(b)** 5-μm-thick Mylar films glued on aluminum frames. On the top sample, a TUM pattern is barely visible.

Table 6.1.: List of ^{6}LiF samples. Both samples are 5-μm-thick Mylar foils with different patterns.

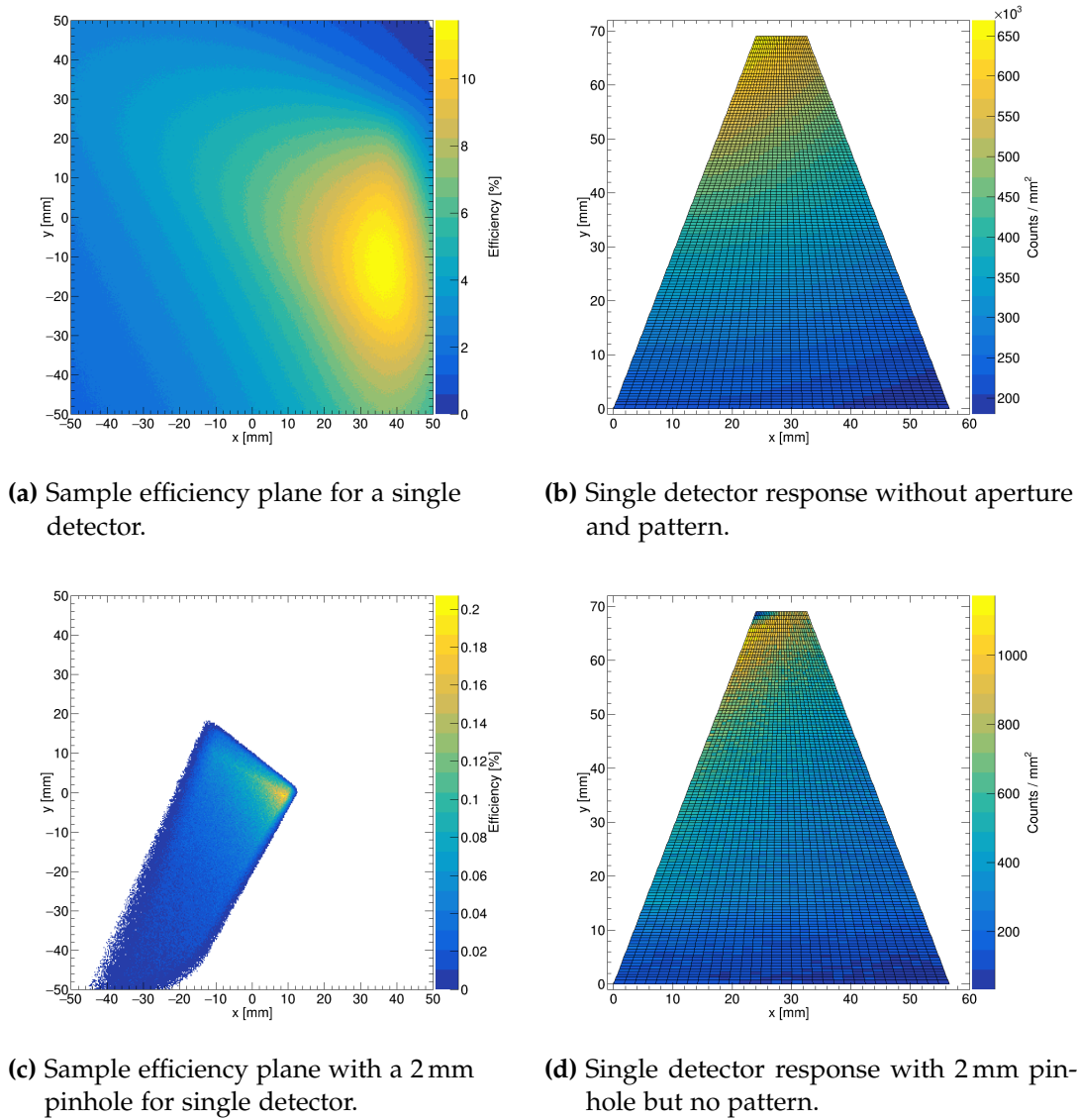| Sample Number	Sample Side 1	Mass Thickness Side 1 $\left[\frac{\mu g}{cm^2}\right]$	Sample Side 2	Mass Thickness Side 2 $\left[\frac{\mu g}{cm^2}\right]$
1	TUM	15.0	TUDelft	10.3
2	Cat	19.7	TU Flame	20.9

camera obscura method is $V = \frac{b}{g} \approx 2$, which means $B = 2 \cdot G$ on average. This value varies over the surface of the detector due to the sample tilting.

6.2 Geometric Efficiency Simulations

To obtain the geometric efficiency for each detector pixel for this setup, Monte-Carlo (MC) simulations were performed. For this, if not stated otherwise, 10^5 vectors were generated randomly in 4π solid angle from the sample plane. This plane equation is defined by $Ax + By + Cz + D = 0$, taking the x, y, z coordinates of three sample corners from the CAD model. An efficiency map of the sample plane without an aperture is shown in Fig. 6.5a. For these simulations, elements with sizes of $0.25 \times 0.25\,\text{mm}^2$ in the sample plane were assumed, ranging from $-50\,\text{mm}$ to $+50\,\text{mm}$ in both directions. The ratio of the number of vectors intersecting the detector area divided by all the generated vectors gives us the geometric efficiency for each sample element. To check if any generated vector intersects the detector area, the Möller-Trumbore algorithm [139] is used, which is an algorithm commonly applied for ray tracing. Based on these simulations, we can determine the region with maximum efficiency. If we use a 2-mm-pinhole between the sample and detector, we obtain a different efficiency map shown

in Fig. 6.5c. Due to the tilt of the sample, the efficiency is different for each point.

(a) Sample efficiency plane for a single detector.

(b) Single detector response without aperture and pattern.

(c) Sample efficiency plane with a 2 mm pinhole for single detector.

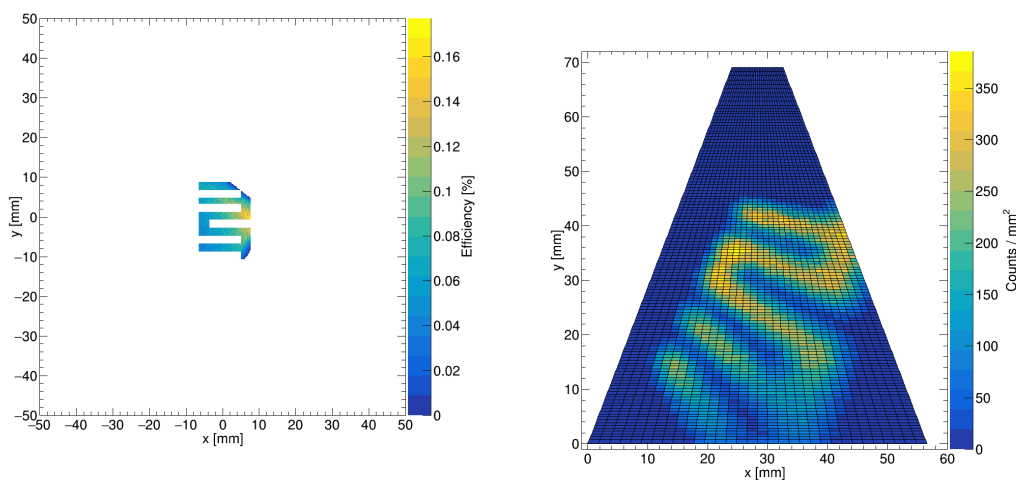**(d)** Single detector response with 2 mm pinhole but no pattern.

Figure 6.5.: Simulated efficiency maps for the sample plane and corresponding detector responses. 10^5 vectors per sample element, with sizes of $0.25 \times 0.25 \, \text{mm}^2$, were generated. The efficiency is calculated as the ratio of the number of vectors intersecting the detector to the total number of vectors generated. Note the differences in the scales with and without the aperture.

As a last step, we simulate the image of the sample with the TUM pattern (as used in the experiment). We obtain a cut of the efficiency map with the same pinhole, as shown in Fig. 6.6a. We observe the maximum efficiency of $\epsilon_{\text{geom}} \approx 12\%$ on the sample plane at $x \approx 36 \, \text{mm}$ and $y \approx -12 \, \text{mm}$ if no aperture is used. When using an aperture of 2 mm, then this point is at $x \approx 7 \, \text{mm}$ and $y \approx -1 \, \text{mm}$ with an efficiency of $\epsilon_{\text{geom}} \approx 0.18\%$. Furthermore, when using an aperture, we can see the region of the sample plane, which

is still visible on the detector.

The detector response for the simulations without pinhole and without a geometric cut on the sample plane with the TUM pattern (we denote this as TUM cut), with pinhole and without TUM cut, and with pinhole and TUM cut are shown in Figs. 6.5b,d and Fig. 6.6b respectively. For the detector responses, the count numbers have been normalized to pixel areas since the very first and last 9 p strips (first on the bottom and last 9 on the top of the detector) cover a larger area (3 strips bonded together as explained in Chap. 3), and therefore the efficiency would be overestimated. The efficiency values are important for normalizing the rate of each pixel and showing any non-uniformity of the neutron beam.

**(a)** Sample efficiency plane with 2 mm pinhole and TUM cut.

(b) Detector response with 2 mm aperture and TUM cut.

Figure 6.6.: Simulated sample plane efficiency map and expected detector response when using a TUM pattern cut and a 2 mm pinhole. In **(a)**, the efficiency is calculated as the ratio of vectors intersecting the detector to the total number of vectors generated. In **(b)**, the numbers of vectors in each pixel are given per area. The TUM cut was roughly placed as in the experiment. The pinhole mirrors the pattern upside down, but due to the point of view, it does not mirror it on the x axis. Due to the tilt of the sample, the magnification is position-dependent and changes the intensities on the detector significantly.
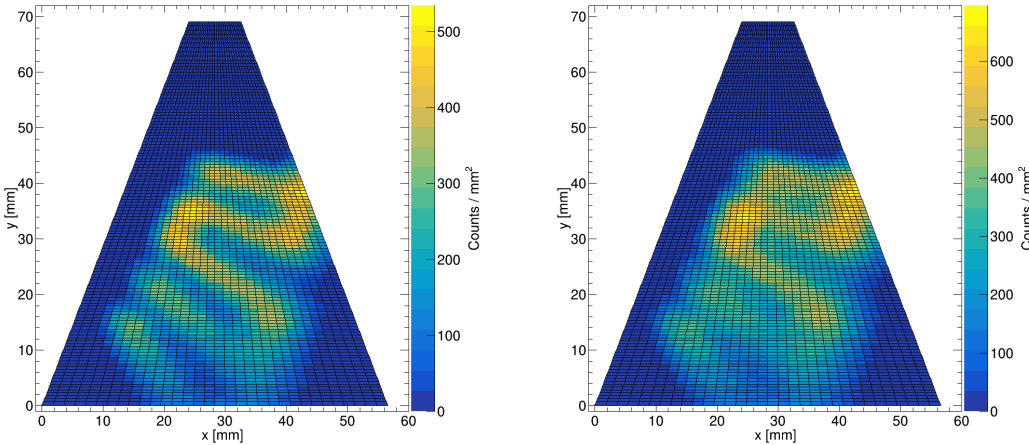
If we look at the simulated detector response for different pinhole diameters. We use Eq. 2.21 to determine the resolvable lateral distance on our detector. We use $p = 0.52$ mm for the pitch width, a magnification $M = 2$ from our geometry, and vary the pinhole diameter from 1 to 3 mm in 0.5 mm steps. We obtain for the lateral standard deviations $[0.7; 1.2; 1.6; 2.0; 2.5]$ mm, respectively. This is the standard deviation of the convolution of the pinhole and the pitch, as explained in Sec. 2.3. In the TUM pattern, the distance between vertical lines of the pattern is 2 mm. Therefore, we expect that

using a pinhole with a diameter of 2.5 mm limits the separation of structure in the pattern. Fig. 6.7 shows the simulations created for different pinholes. We can still identify the TUM pattern when using the 2.5 mm pinhole, but the situation worsens when using the 3 mm pinhole.
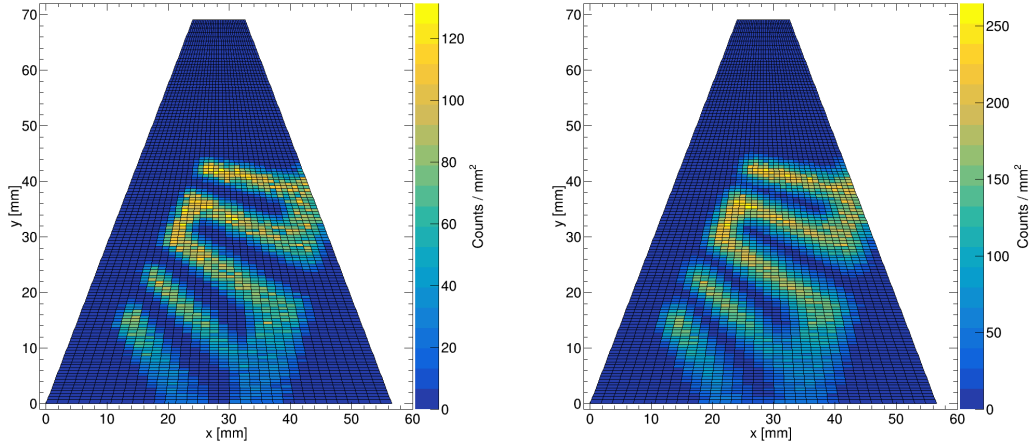
(a) Detector response with 1.0 mm aperture.   **(b)** Detector response with 1.5 mm aperture.

(c) Detector response with 2.5 mm aperture.   **(d)** Detector response with 3.0 mm aperture.

Figure 6.7.: Simulated detector responses for different pinholes. The response for 2-mm-aperture, as mainly used in the experiment, is given in Fig. 6.6b. Pinholes with diameters $d > 2.5$ mm can no longer separate the lines of the TUM pattern.

6.3 Experimental Results

First, we estimate the expected count rate for the first sample given in Tab. 6.1. We used the cross section of $\sigma_{\mathrm{th}} \approx 940$ barn. The areas were estimated to be $A_{\mathrm{TUM}} \approx 1.63$ cm^2 and $A_{\mathrm{TUDelft}} \approx 0.31$ cm^2 for the TUM and TUDelft patterns, respectively. For the

efficiency, we estimated from the MC simulations about $\epsilon \approx 9.2\,\%$ averaged over a $\approx 2 \times 3\,\mathrm{cm}^2$ area. Using Eq. 2.2, we estimate the count rate at either detector

$$R_{\text{Pattern,calc}} = \frac{\rho_{A,\text{Pattern}} \cdot N_A \cdot A_{\text{Pattern}} \cdot \Phi_{\text{th}} \cdot \epsilon \cdot \sigma_{\text{th}}}{M} \, ,$$

where N_A is the Avogadro constant, $M = 25.01\,\frac{\mathrm{g}}{\mathrm{mol}}$ is the molar mass of enriched ^{6}LiF, and $\rho_{A,\text{Pattern}}$ and A_{Pattern} are the areal density and surface area of the pattern. Using the areal densities given in Tab. 6.1, we calculate the count rates to be $R_{\text{TUM,calc}} \approx 511\mathrm{s}^{-1}$ and $R_{\text{TUDelft,calc}} \approx 67\mathrm{s}^{-1}$ for the TUM and TUDelft patterns, respectively. If we sum up all the events from the tritons and α particles on either detector from the respective side, we observe that the rates are $R_{\text{TUM,meas}} = 529\,\mathrm{s}^{-1}$ and $R_{\text{TUDelft,meas}} = 90\,\mathrm{s}^{-1}$, which are close to the expected values for uniform illumination of the sample.

### 6.3.1 Particles Identification

For any ADC-based DAQ system, a pedestal is characteristic and needs to be calibrated to obtain the correct relation between ADC values and energy deposited in the detector. As an example, Fig. 6.8 shows the pedestal from detector 2 for all p channels, where the DAQ system reads the strips without the hit information. All ADC values are plotted without the strip that triggered the readout. At channel numbers 63 and 64, we observe a decrease in the count rate (see Fig. 6.8). These are the last and first channels of the first and second SKIROC 2A ASICs, respectively, which account for neighboring strips on the detector surface.
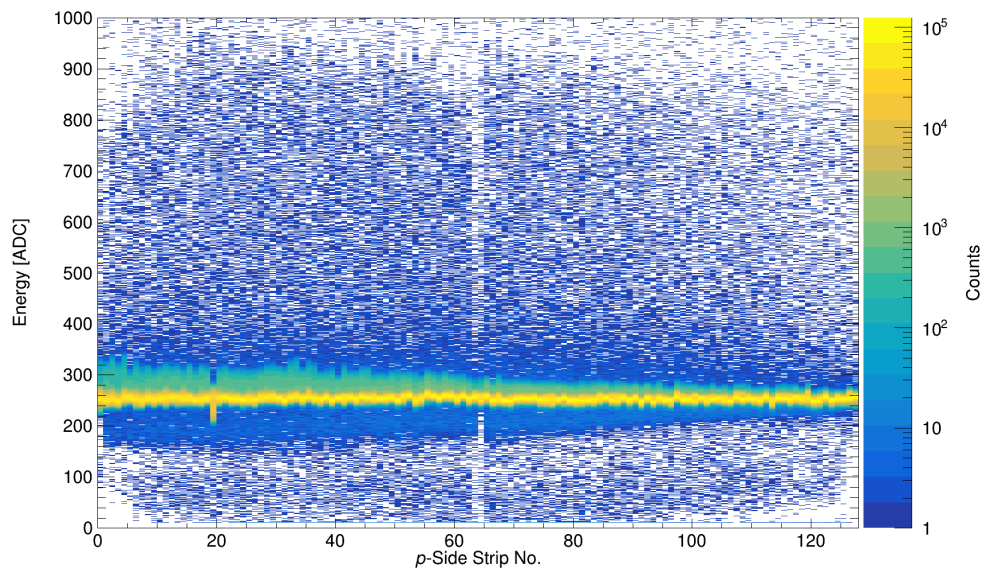
Figure 6.8.: Pedestal and noise in detector 2 for the p strips. We observe a rather constant electronic offset at $\sim 250\,\mathrm{ADC}$ for all the channels. A very similar figure (added to the Appendix C) can be obtained from the p side of the other detector and also from the n sides of both detectors.
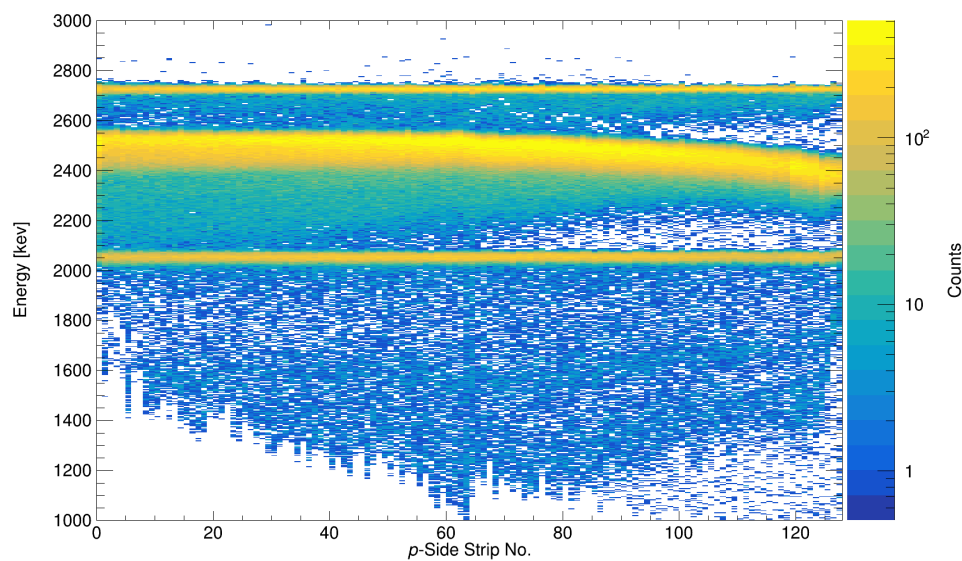
**(a)** *p* strips versus energy.
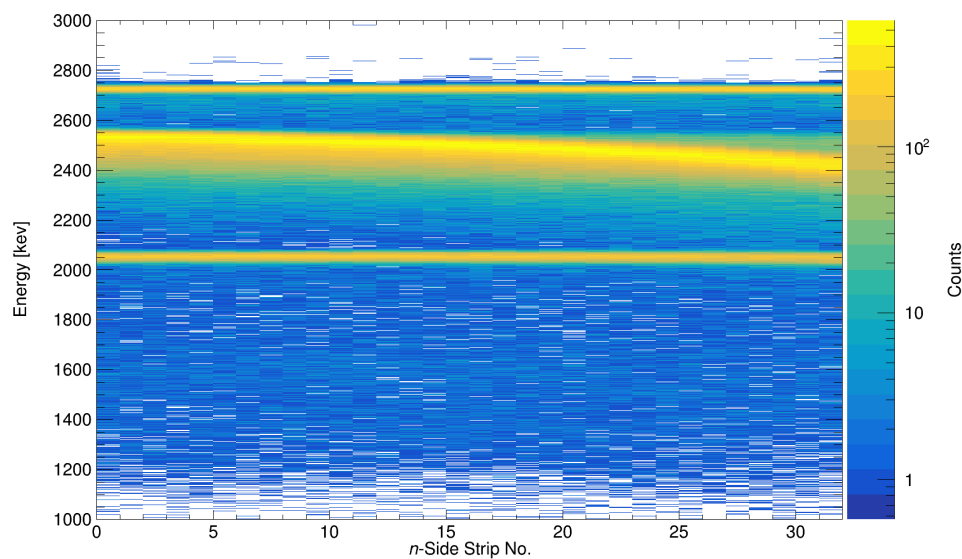
(b) *n* strips versus energy.

Figure 6.9.: Energy spectra on the *y* axis (*p* strips) and on the *x* axis (*n* strips) for detector 2. We observe tritons and α particles at 2.73 MeV and 2.05 MeV from the sample side facing the detector, and triton particles at ~ 2.50 MeV from the opposite side of the sample.

If we turn on the neutron beam and read out the hit from the DAQ on individual strips, we obtain the energy distributions across the *p* strips (shown in Fig. 6.9a) and across the *n*-strips (shown in Fig. 6.9b) of detector 2. For completeness, plots from detector 1

can be found in the Appendix C.

For these plots, we used no aperture. We calibrate all the channels with a linear fit by assuming that the triton and α particles originating from the side facing the detector deposit an energy of 2.7 MeV and 2.0 MeV (from the ^{6}Li$(n, \alpha)^3$H reaction listed in Tab. 2.1), respectively. For smaller energies, an additional linear calibration was applied to meet the pedestal offset points, which are at $\sim$ 250 ADC. Using the WebAtima tool [132], we calculated the energy loss of triton particles through the 5-μm-Mylar and confirmed the correctness of the calibration. We expect the tritons originating from the other side of the foil to lose about $\sim$ 181 keV. We observed these triton particles in the calibrated spectra, shifted to lower energies at the top of the detector. For the n side, this shift appears on the detector side, which is closer to the sample. Due to the mirrored setup, the shift is also mirrored. We can attribute these shifts to the tilting of the sample plane. The particles must travel $1/\cos\theta$ times longer distance through the Mylar, losing more energy before arriving at the detector. This factor also contributes to the broadening of the triton peak from the other side. From the geometry, we estimate the maximum angle to be $\theta \approx 48°$ from the bottom part of the sample to the top part of the detector. This maximum angle corresponds to an energy loss of about $\sim$ 275 keV, which can be observed on the right-hand side in Fig. 6.9a.
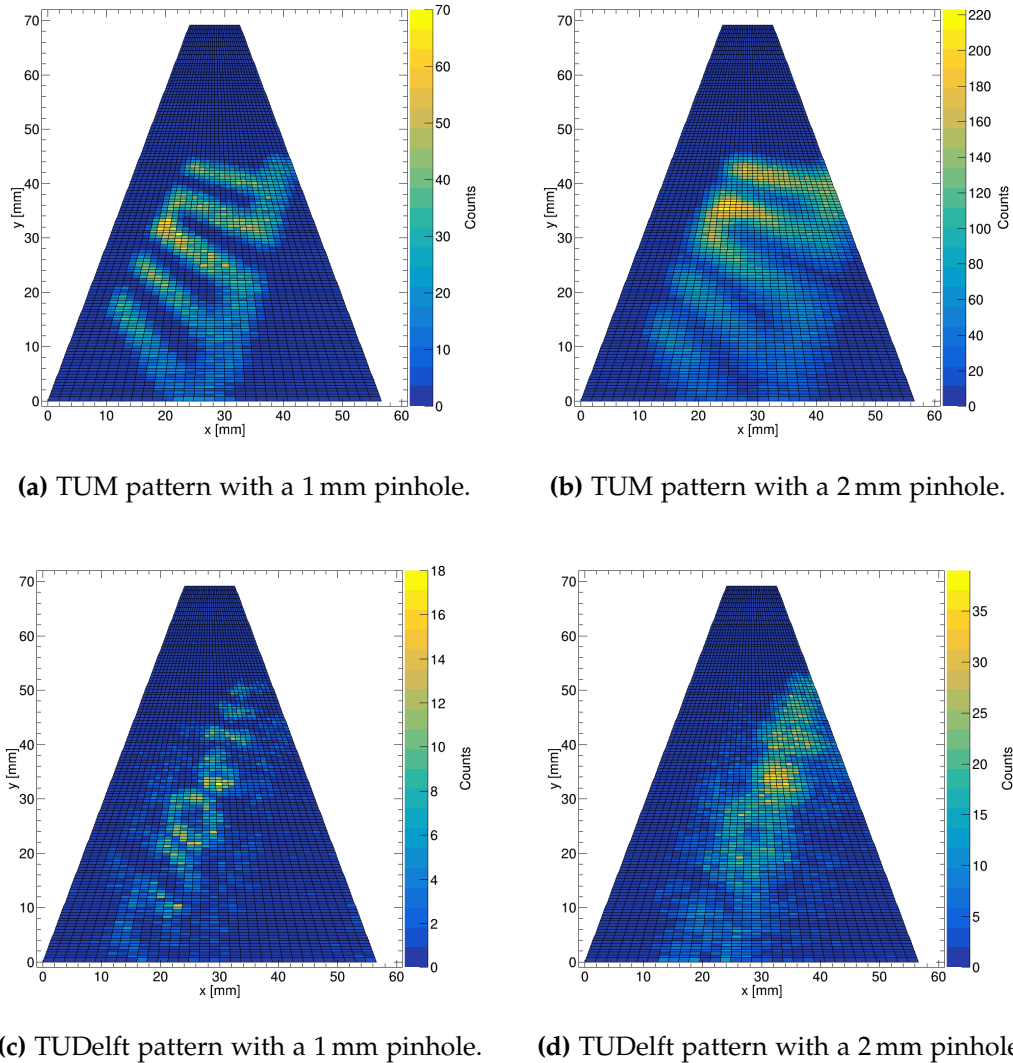
Since the energy resolution for the p strips is expected to be better than that for the n strips due to better ENC from the SKIROC 2A compared to the CMS chips, we use these energy values for the n side. The energy spectrum from detector 2 of one p channel and one SCA is shown in Fig. 6.10, which shows the resolution of the triton particles at 2.7 MeV.
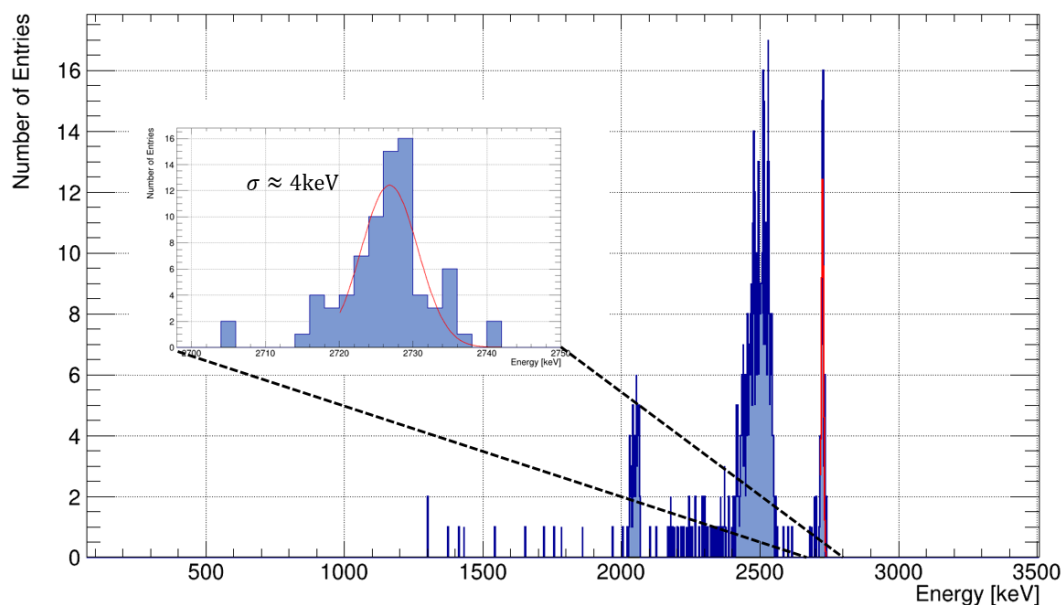
Figure 6.10.: Energy spectrum of detector 2, channel 47, SCA number 0. A zoom-in of the triton peak at 2.7 MeV is also shown. The triton peak was fit with a Gaussian distribution, giving a standard deviation of $\sigma \approx 4$ keV.
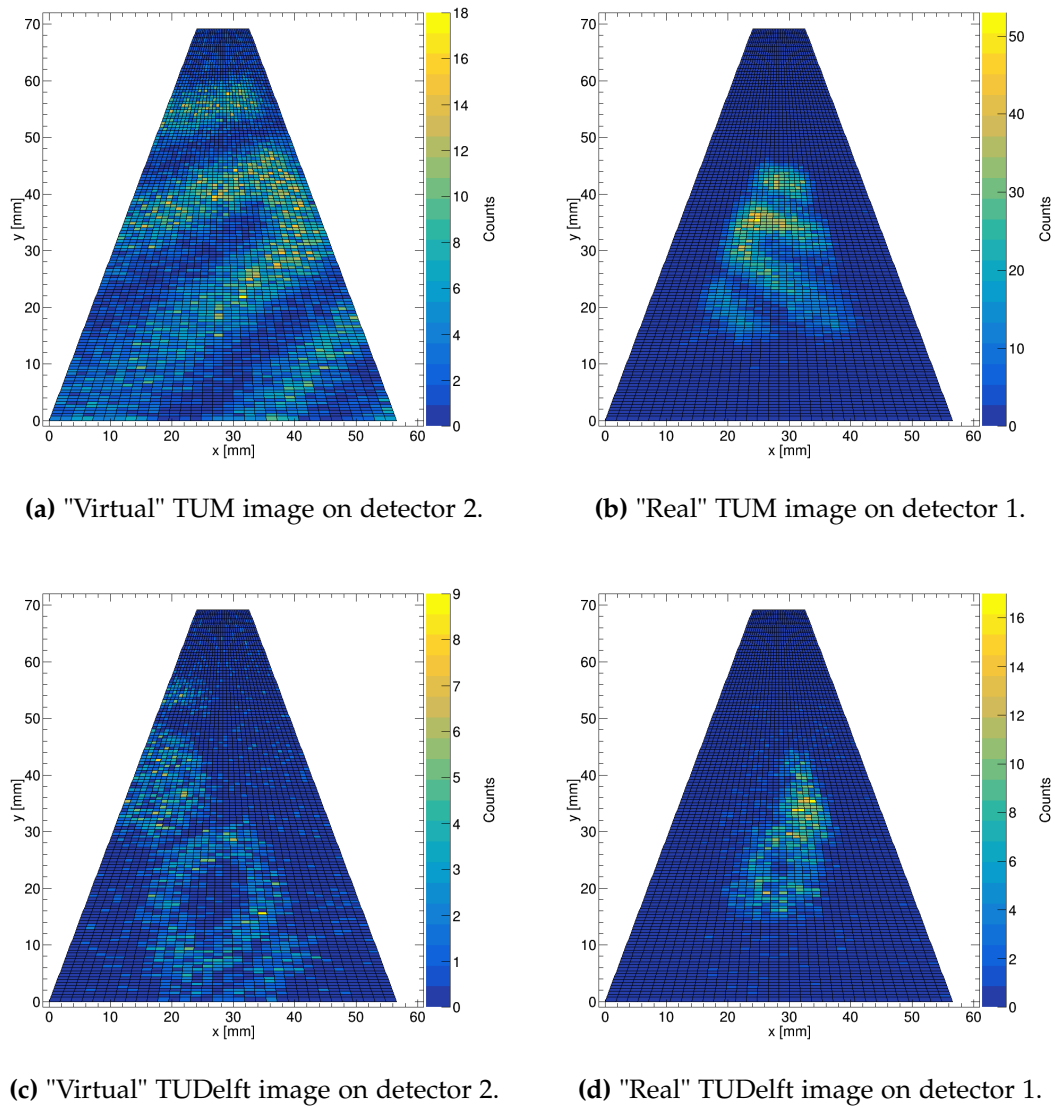
6.3.2 Lateral Mapping

In this measurement campaign, we were able to apply both imaging methods, the camera obscura and the coincidence method (as described in Chap. 2). For the camera obscura measurement, we used pinholes with diameters 1 mm, and 2 mm in front of detector 1. Since using the aperture lowers the count rate by a factor of 30 (for $d = 2\,$mm), for the coincidence method, no pinhole was used.

(a) TUM pattern with a 1 mm pinhole.

(b) TUM pattern with a 2 mm pinhole.

(c) TUDelft pattern with a 1 mm pinhole.

(d) TUDelft pattern with a 2 mm pinhole.

Figure 6.11.: Detector images from the camera obscura measurements with sample 1. The TUM patterns are well visible with both pinholes, as expected from the simulations shown in Sec. 6.2. The TUDelft pattern on the backside of the sample is slightly visible with the 1 mm aperture but cannot be resolved with the 2 mm aperture. Only the triton data from the TUDelft side was used, as the α particles were not observed due to the energy threshold set.

Camera Obscura Method

Camera obscura images of sample number 1 (see Tab. 6.1) obtained with pinholes of 1 mm and 2 mm are shown in Fig. 6.11. The measurement time for these images was approximately 2.5 h each. For the images, the energy threshold is 2.0 MeV to provide better image clarity.


(a) "Virtual" TUM image on detector 2.

(b) "Real" TUM image on detector 1.

(c) "Virtual" TUDelft image on detector 2.

(d) "Real" TUDelft image on detector 1.

Figure 6.12.: TUM and TUDelft pattern images from using coincident particles of the two detectors and the 2-mm-pinhole. In Figs. **(a)** and **(c)**, mirrored pictures of TUM and TUDelft patterns with a magnification of 4 are shown, while Figs. **(b)** and **(d)** show pictures of detector 1 with a magnification of 2.

The TUM pattern faced the pinhole, and on the other side of the sample, the TUDelft pattern faced detector 2 without a pinhole. If we correlate the events on the p and n strips, we obtain an image of the TUM logo. This image appears to be tilted on the

detector because of the varying distance from the pinhole. The triton particles from the other side also contributed to the picture. The signal of the α particles from the opposite side of the sample, which have a remaining energy of ~ 800 keV, are filtered out.

Selecting the energies between 2.4 MeV $< E < 2.6$ MeV, corresponding to the triton particles only from the opposite side of the sample, gives the images in Figs. 6.11c,d. For the TUDelft pattern, the mass thickness and the area are smaller than for the TUM pattern, resulting in a lower overall reaction rate. Note that the TUDelft pattern is too fine (distance between the letters is ≈ 0.7 mm) to be resolved with the 2 mm pinhole and is, as expected from the standard deviation, barely visible with the 1 mm. If we use the second detector and look at coincident events that went through the aperture, we observe a so-called virtual image, as shown in Figs. 6.12a,c. Due to the distance ratio of 4 : 1 (*i.e.*, 4 units from detector 2 to aperture and 1 unit from aperture to sample), the TUM pattern has a magnification of four and does not fully match the detector field of view. Last, since the α and triton particles are emitted back-to-back, with the coincident detection, we obtain similar images on both detectors, as shown in Fig. 6.12. The magnifications are 2 and 4 for detectors 1 and 2, respectively, as discussed above.
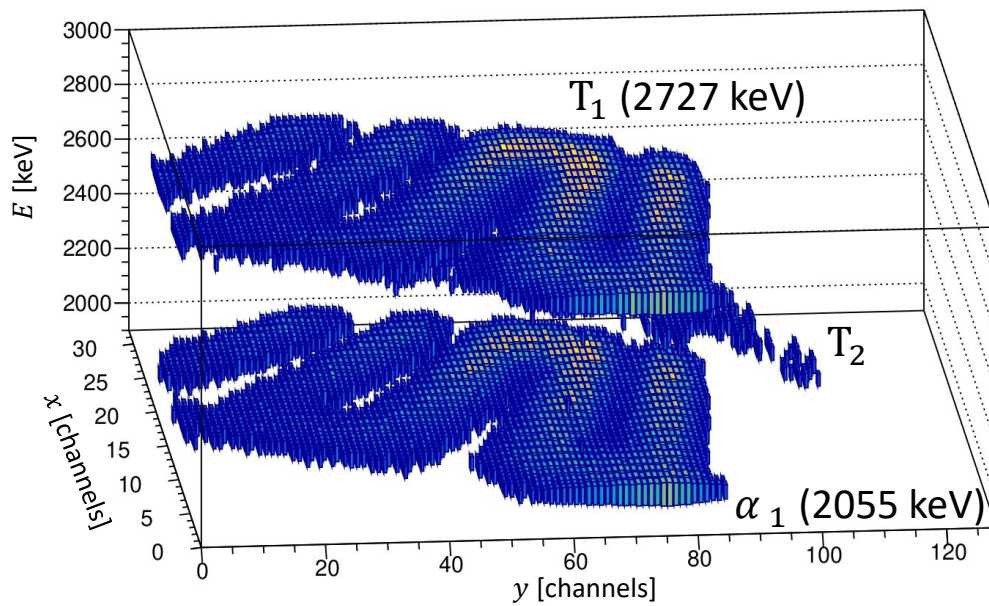
Figure 6.13.: 3D picture of the sample on detector 1. A 2-mm-pinhole was used. We observe the two energies from the α (at 2.0 MeV) and triton (at 2.7 MeV) particles from the TUM logo side facing the detector and an intermediate energy (at ~ 2.5 MeV) from the tritons from the other side of the sample. Image taken from [90].

Finally, we want to showcase a energy-resolved image in three dimensions (shown in Fig. 6.13) taken using the 2-mm-pinhole. A binning of 50 keV was used on the energy axis. This image corresponds to the one in Fig. 6.11b, plotting the energy on the z axis.

We observe two energy layers (at 2.7 MeV and 2.5 MeV) of tritons of both sides of the sample (T_1 and T_2) and one energy layer of α particles (α_1) at 2.0 MeV. The second triton layer comes from the second side of the sample, bending towards lower energies at the top of the detector (as explained in Sec. 6.3.1). The TUM pattern is visible at both energies, whereas the TUDelft is barely resolved because of the fine pattern.

Coincidence Method

The coincidence imaging method uses two detectors to observe particles emitted under $180°$, as described in Chap. 2. By matching the trigger times of the two detectors, we can reconstruct the trajectory of the emitted particles. From the known geometry of the setup, we can then reconstruct the reaction location on the sample plane. The reconstructed images of both samples from Tab. 6.1 are shown in Fig. 6.14. For these images, we used events with energies in the range of $1.9 - 2.1$ MeV for the α particles from the sample side facing the detector and those in the range of $2.4 - 2.6$ MeV for the tritons on the other detector from the same layer.
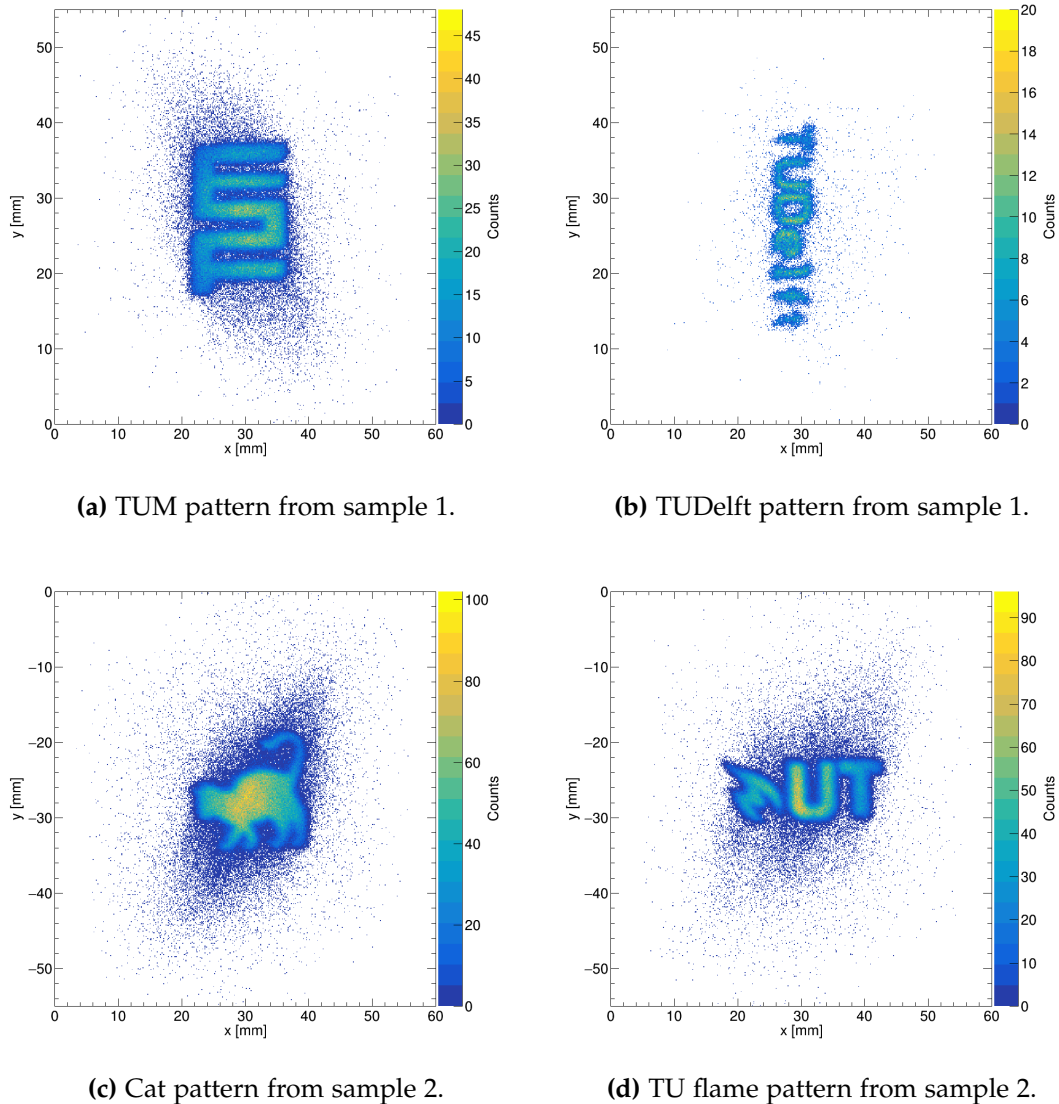
To reduce the appearance of artificial patterns, we used the following corrections: Since each pixel has a certain size, instead of plotting all hits in the center, they are uniformly distributed over the whole pixel area. The detector modules were placed on thin heat-conducting foam elements, causing the detectors to further tilt towards the sample. A correction tilt of $1.5°$ for each detector was assumed as a small geometry correction.

Methods Comparison

As a final conclusion for this chapter, we determine the resolution of both methods. In Chap. 2, we described the position resolution as the standard deviation of a trapezoidal distribution, which describes the convolution of two uniform distributions (from the pinhole and the pitch widths). Using Eq. 2.21, we calculated the standard deviation for both methods. Here, different values were determined due to different pitch widths for either side of the detector. Furthermore, as explained in Chap. 3, due to the detector's shape, the width of an n strip will be wider on the long side of the detector than on the short side, resulting in a position-dependent resolution. For the p side, it should be mentioned that on the minor side, we have 9 channels, and on the major side, 1 channels, which are bonded in groups of 3, unlike all others that are grouped in 2 to match the maximum number of 128 channels of the ASICs. This also gives us larger pitch widths and, therefore, different values for the standard deviation on the p side. With a magnification factor of 2 and a pinhole diameter of $d = 2$ mm, we obtain the values given in Tab. 6.2.

Unlike the coincidence method, the position resolution is tuneable for the camera obscura method by tuning the diameter of the pinhole. To achieve a similar position resolution for the camera obscura method in this setup, a pinhole with a diameter of $d \approx 0.25$ mm has to be used. However, lowering the diameter also reduces the geometric efficiency, thus drastically decreasing the count rate (in this case, by a factor of about 64).

(a) TUM pattern from sample 1.

(b) TUDelft pattern from sample 1.

(c) Cat pattern from sample 2.

(d) TU flame pattern from sample 2.

Figure 6.14.: Reconstructed images from the two samples given in Tab. 6.1. Pixel binning on the sample plane of $0.12 \times 0.12\,\mathrm{mm}^2$ are used. Sample 2 was upside down in the setup, so the images have been mirrored to highlight the reconstructed patterns. The background may result from coincident events where the tritons are scattered in the sample through Coulomb interaction with the carbon atoms. Its elongated form on the diagonal could be a result of the trapezoidal shape of the detector.

In the Delft experiment, the segmented thin detectors showed their capability in resolving 3 dimensional profiles with individual time stamping. We obtained an almost background-free signal by optimizing the settings of the low-noise electronics and carefully filtering the acquired data. It must be mentioned that calculated and simulated data are in full agreement with the experimental data. The missing component for the upgrade towards high-resolution four-dimensional profiling using the N4DP instrument was successfully tested.

Table 6.2.: Position resolutions for both methods. The uncertainties are calculated using the error propagation of Eq. 2.21. The following uncertainties were assumed: $\Delta d = 50\,\mu$m, $\Delta p = 40\,\mu$m, and 1 mm accuracy for the distances between the sample, aperture, and detector.

Method	Detector Face	$\sigma_{\mathbf{min}}$ [mm]	$\sigma_{\mathbf{max}}$ [mm]
Camera Obscura	p Side	1.524 ± 0.081	1.589 ± 0.082
	n Side	1.324 ± 0.076	1.657 ± 0.082
Coincidence	p Side	0.212 ± 0.016	0.318 ± 0.016
	n Side	0.108 ± 0.016	0.721 ± 0.016

Conclusion and Future Work

The project "Time Resolved Isotope Analysis with Cold Neutrons (N4DP)" was funded by the German Federal Ministry of Education and Research (BMBF) under project numbers 05K16WO1 and 05K19WO8. The primary goal of the project was to establish an NDP instrument at the FRM II to provide a complementary analytical method to the already existing instruments. Initial feasibility tests of the new instrument were done in collaboration with the NIST group, taking advantage of their expertise in the field of NDP. This led to the development of the N4DP setup, which allows for *operando* measurements with the best possible depth resolution using silicon surface-barrier detectors. To extend the capabilities of the system to 4D measurements, we successfully developed segmented 2D silicon strip detectors in collaboration with the TREX group under project number 05P21WOCI1. These developments are based on the work of M. Trunk [123], L. Werner. [113], and were implemented and tested in the frame of this work. In Sec. 7.1, the main developments and results of this work are listed, while in Sec. 7.2, important characteristics of the new system are highlighted. Finally, in Sec. 7.3, some perspectives for further improvement of the system are described.

7.1 Methodological Developments

In the frame of this thesis, developments have been made towards four-dimensional neutron depth profiling with the N4DP instrument at the Heinz Maier-Leibnitz Zentrum. For the first time, an NDP instrument is equipped with a detector that allows for position-sensitive measurements. The new double-sided silicon strip detector system enables not only high-precision depth profiling (resolution is $\sim 50\,\mathrm{nm}$) of NDP-specific nuclei, but also the investigation of their lateral distribution with an accuracy down to $\sim 100\,\mu\mathrm{m}$, as well as the monitoring of their temporal variation with a time integral of $\sim 5\,\mathrm{s}$. In several measurement campaigns, it was possible to fully characterize the system. The most important results of the upgrade of the N4DP instrument, achieved within this work, are summarized in the following:

1. In collaboration with the silicon development team of CiS, we defined a set of parameters for the production of position-sensitive detectors and initiated their series production. Detectors treated with different RTA parameters for various implantation profiles were produced and tested. We found an optimum for these parameters at an annealing temperature 950°C and an annealing time of 15 s by testing these detectors with α particles from a calibration source. With these parameters, a very thin ($\sim 150\,\mathrm{nm}$) and homogeneous dead layer can be established. The detectors showed energy resolutions of $\Delta E_{\mathrm{FWHM}} \approx 17\,\mathrm{keV}$ for

the α source measurement, and $\Delta E_{\text{FWHM}} \approx 10\,\text{keV}$ for tritons from the ^{6}Li(n,α) reaction used in the Delft experiment. This energy resolution is comparable to that of silicon surface-barrier detectors typically used in NDP experiments at FRM II, which is the highest achievable resolution currently available worldwide for such applications.

2. The silicon detectors, designed for on-chip AC signal coupling of each individual strip, were systematically tested and several strips on each detector were found to have leakage currents well above the specified limits. Several attempts were made to improve the insulating layer, which consisted of a combination of thermal oxide and epitaxially grown layers of either SiO_2 or Si_3N_4. Looking at the leakage current going through these layers, we found out that due to their small thickness ($\sim 20\,\text{nm}$), which is needed for a large coupling capacitance, they introduced so-called pinholes, causing the reverse bias to break for several strips. We therefore integrated the new detectors with external AC-coupling to the low noise ($ENC \approx 6\,\text{keV}$) SKIROC front-end ASIC via SMD capacitors on custom-made PCBs. Other key electronic components, such as temperature sensors and high voltage input and output connectors, were also implemented on this board. The detectors on the boards showed stable IV behavior up to $200\,\text{V}$ vias voltage.

3. The characterization of the detector modules was carried out in several measurement campaigns, including a laboratory setup with a weak α-emitter, beamtime with a proton beam at the Cyclotron Centre Bronowice in Krakow, Poland, as well as two different beamtimes with neutrons at the Research Reactor in Delft, The Netherlands.

   a) First, in our laboratory, we made the first two-dimensional images of a patterned mask in front of the DSSSD illuminated by a point-like α source. We developed calibration software to simultaneously determine the response of 15×128 memory cells of both ASICs. In an improved setup, we determined the thickness of the dead layer, which limits the energy resolution.

   b) After this proof of principle of a single DSSSD, we tested the coincidence detection using (p,2p) reactions on a fixed polypropylene string target at the Cyclotron in Krakow. We manufactured a board to synchronize the clocks of the different FPGAs. We also found that lowering the threshold in some channels of the detectors created unwanted triggers, artificially increasing the rate and, consequently, the total dead time.

   c) These unwanted triggers motivated the improvements of electronic parameters, which were successfully investigated in an experiment at RID. These new settings significantly reduced random coincidences, and the desired reaction events could be selected almost without background. Furthermore, we obtained the first laterally resolved NDP results, using the ^{6}Li(n, α)^{3}H reaction of different ^{6}LiF patterns with the camera obscura and the coincidence methods. The expected patterns were accurately reconstructed for both methods, with positional resolutions down to $\sim 100\,\text{nm}$. The results of this experiment have been published in [90].

4. The N4DP chamber was modified to accommodate two feedthroughs for the new electronics. This allows for the full integration of the segmented 2D detectors, enabling high-precision, high-rate *operando* measurements at the FRM II.

5. As a part of a bachelor thesis, a chopper was developed for the neutron beam at the PGAA facility. This chopper allows for estimating the delayed β and γ background during the measurement of the signal. By subtracting this background from the signal during the measurement, it is possible to increase the signal-to-background ratio.

As the system is fully developed and characterized, its capabilities to resolve the four dimensions are discussed below.

7.2   Capability

Although the camera obscura and the coincidence methods have been successfully tested, each has unique advantages and disadvantages, as described below and listed in Tab. 7.1. In any case, both methods require knowledge of the geometry in order to correctly reconstruct the target and its 3D profile.

The **camera obscura** method allows for the analysis of thicker samples since only one of the emitted particles, the lighter one, needs to be detected. Therefore, the method requires only one detector and the use of an aperture. By tuning the aperture size, one can vary the resolution and count rate. However, this resolution is typically lower than that of a dual-detector setup used in coincidence. Certainly, the count rate scales with the pinhole size ($R \propto \epsilon \propto d^2$, *i.e.* a 10 times smaller pinhole would give a 100 lower rate).

The **coincidence** method requires two detectors symmetrically mirrored around the target to detect both particles produced by any NDP reaction (listed in Tab. 2.1). This method uses the solid angle covered by the detectors' active areas, therefore the reaction rate is typically not an issue. The position resolution is typically better with this method by roughly an order of magnitude, as the pixel size is typically smaller than a pinhole. However, because of the need to detect both particles, the thickness of the sample is limited to the penetration depth of the recoil (heavier) particle. Therefore, the coincidence measurement is only possible for very thin samples.

Table 7.1.: Main characteristics of the two scanning methods. The values are only rough estimates since they depend on various factors, *e.g.*, the rate depends on the neutron flux, the geometric efficiency (given by the geometry of the setup), and for the camera obscura it also depends on the size of the pinhole.

Method:	Camera Obscura	Coincidence
Sample Thickness[1]	$\mathcal{O}(< 50\,\mu\text{m})$	$\mathcal{O}(< 10\,\mu\text{m})$
Rate	$\mathcal{O}(100\,\text{s}^{-1})$	$\mathcal{O}(1000\,\text{s}^{-1})$
Position Resolution[2]	$\mathcal{O}(1\,\text{mm})$	$\mathcal{O}(100\,\mu\text{m})$
# Detectors	single	dual[3]

Rate and Temporal Limits

As described in Chap. 3, the SKIROC ASICs only allow a bunched data stream, which results in a dead time while reading out the chips. The usual readout scheme requires the system to be in an idle state after recording 13 events. For a fast-evolving signal, it is necessary to measure its change at least once in a time interval similar to the dead time t_d to still be able to measure the change of the signal. An analogous effect is the aliasing for any periodic signal (described by the Nyquist-Shannon sampling theorem [140, 141]).

Since the dead time t_d of our electronics is roughly $7\,\text{ms}$[4] for a single readout, we can estimate a maximum count rate by dividing 13 with the dead time, thus resulting in $R_{\text{max}} \approx 1850\,\text{s}^{-1}$ for the slow readout scheme ($R_{\text{max}} \approx 13000\,\text{s}^{-1}$ for the fast readout). For *operando* measurements, we can then use this maximum achievable rate to estimate a lower integration time limit ΔT_{min} for significant depth (1D) and volume (3D) profiles. For a total number of events N, let us define the proper statistics as 10% uncertainty in each channel assuming Poisson statistics [142]. Then, we need $N = 100$ events per channel. To calculate the time needed for a proper profile, we need to take into consideration the total dead time, which is given by $T_d = t_d \cdot n_{\text{pixel}} \cdot N/13$, where n_{pixel} is the number of pixels. For depth profiling (1D), the whole detector can be seen as one pixel, thus $n_{\text{pixel}} = 1$, and therefore $\Delta T_{\text{min,1D}} \approx 100\,\text{ms}$ for the slow readout (and $\sim 15\,\text{ms}$ for the fast readout). To estimate the time needed for a proper 3D profile, we need to assume the sample size that will be projected on the detector. The effective area per detector pixel is $A_{\text{eff}}/4096 \approx 1.82\,\frac{\text{pixel}}{\text{mm}^2}$ (this is an average value and it varies for different parts of the detector). If we now assume a typical NDP sample with a size of $\approx 1 \times 1\,\text{cm}^2$ and a magnification of $M = 2$ in the camera obscura setup, the image will appear over ~ 360 pixels. Again, assuming the maximum rate for all the pixels, for a 3D profile, we need about $\Delta T_{\text{min,3D}} \approx 0.5\,\text{min}$, or two frames per minute. This gives us an idea of approximate limits for *operando* measurements.

Finally, let us summarize these time limitations. The following assumptions are made to obtain the values:

1. The maximum achievable rate $R_{\text{max}} = 1850\,\text{s}^{-1}$ is used;

2. A total number of events per pixel $N = 100$ is used;

3. A $1\,\text{cm} \times 1\,\text{cm}$ sample size is used;

4. A magnification $M = 2$ is used.

Using these, we obtain $\Delta T_{\text{min,1D}} \approx 100\,\text{ms}$ and $\Delta T_{\text{min,3D}} \approx 30\,\text{s}$.

---

[1]The depth achievable is highly dependent on the sample density and the NDP reaction used.

[2]For the camera obscura method, this value depends on the pinhole size, whereas for the coincidence method, this value is rather fixed.

[3]At least two. In principle, one can use a multiple of two detectors symmetrically mirrored around a target to detect both particles.

[4]This only applies to the slow readout time mentioned in Chap. 3. A faster readout is possible with the 40 MHz internal clock, reducing the $t_d \approx 1\,\text{ms}$.

7.3   Outlook and Future Work

During the time of this thesis, unfortunately, the reactor FRM II was shut down for various reasons, such as the Covid pandemic [143], radioactive ^{14}C leakage [144] and reactor maintenance. Although the N4DP instrument has been well-prepared as a user facility, no user measurements have been carried out during this period, but are planned for 2025. The high user demand is reflected in the many open proposals from collaborators working on materials science applications. For these, further developments are planned and presented here.

7.3.1   Standard 4D Neutron Depth Profiling with the N4DP Instrument

The scientific relevance of the N4DP instrument at the FRM II has been demonstrated in several publications [25, 33, 47, 53]. Its use as a neutron depth profiling instrument can be significantly improved by the new detectors, which have a higher geometric acceptance while keeping the energy resolution at similar levels compared to monolithic surface barrier detectors. The whole setup was upgraded to standard 4-dimensional NDP, where users can choose either 1D depth profiling or 3D volume profiling. The latter comes at the cost of a lower rate in each pixel generated on the detector and, therefore, longer measurement times. It still requires the acquisition and analysis software for the new electronics to be integrated into the MLZ control system.

7.3.2   N4DP Sample Environment

The current adjustable sample holder enables not only different sample geometries but also *operando* measurements and the application of a gas atmosphere in the chamber. For future experiments, a temperature control system[5] is available in the -20°C to $+80^\circ$C temperature range. In these applications, care must be taken to avoid any thermal contact between the heated sample and the chamber, which could increase the thermally induced leakage current into the electronics and degrade the energy resolution. This can be achieved by thermally insulating the sample holder and using temperature-resistant plastic connectors.

7.3.3   Radiation Tolerance of the Detectors

Radiation damage to semiconductor detectors and front-end electronics occurs through two basic mechanisms [68], increasing the leakage current and, ultimately, the required operating voltage [145, 146].
As for the detectors used in the N4DP instrument, they are not operated in the neutron beam, and most of the time, only the particles generated by the NDP reactions and the neutrons scattered from the surroundings hit the detectors and the associated electronics. Nevertheless, it is very important to calculate the lifetime of these detectors. Tomandl *et al.* [28] operated so-called timepix detectors [147] in the beam, and a high distortion of the signal is expected after a long irradiation. In our case, neutrons can scatter (although unlikely) from all parts of the vacuum chamber and hit the sensor and electronics, but the rate is typically several orders of magnitude lower than when

---

[5]From JULABO GmbH

the detectors are operating in the neutron beam. Nevertheless, it is important to systematically evaluate such an effect in order to estimate the lifetime of such a system. The detectors and electronics can be evaluated for their radiation resistance as is done for high luminosity experiments at CERN [148, 149].

7.3.4 Coded Masks

As discussed, the camera obscura is limited in both rate and resolution by the size of the pinhole. A method to overcome these limitations, could be the coded aperture imaging technique, first introduced by Dicke [150] and Ables [151] in 1968. Since then, the technique has been further developed by many others [152–154], mainly for X-ray and gamma-ray astronomy applications [155, 156]. More recently, however, the coded mask method has gained popularity in other applications such as fast neutron-induced elemental analysis [157, 158], inertial confinement fusion neutron imaging [159], and imaging of alpha source spatial distribution imaging [160]. This method has the potential to overcome low-rate problems while still having good position resolution, as the number of pinholes could compensate for the reduction in the diameter of the pinhole.

OBJECT APERTURE RECORDED DECODING RECONSTRUCTION
                   IMAGE   PROCEDURE
S   A   D   G   S
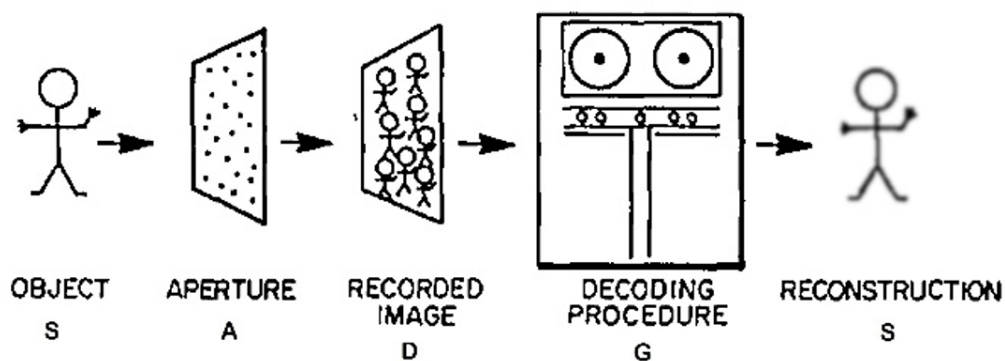
Figure 7.1.: Principle of the coded mask technique. The sample S appears on the detector as a convolved image D of many holes from the coded mask A. By using a deconvolution algorithm G, the original image can be recovered. Modified figure from [153].

The principle of coded mask imaging is based on multiple pinhole imaging. The overlap of the many pinhole images is the result on the detector. We define this convoluted picture as $(S \circledast A) = D$, where S is the sample image, A is the coded mask function, $\circledast$ is the convolution operator, and D is the detected image. This basic principle is shown schematically in Fig. 7.1.

To recover the original image S, a deconvolution algorithm G is required. This decoding pattern must satisfy $A \circledast G = \delta$ [158], with δ being the identity matrix. The reconstruction is given by following $D \circledast G = (S \circledast A) \circledast G = S \circledast (A \circledast G) = S \circledast \delta = S$. There are many different deconvolution algorithms [161] that can be used to process images from coded mask systems, each individually more applicable to different coded

mask patterns [162]. Depending on the noise and accurate knowledge of S, one can then use linear or nonlinear algorithms to co-optimize the imaging performance of such deconvolution processes [163].

Towards the end of this work, we used the coded mask method to get an idea of its applicability in NDP experiments. We used a coded mask in the Delft experiment, with some preliminary results shown below.

Simulation and Experiments

For the experimental setup described in Chap. 6 a coded mask with a random pattern (shown in Fig. 7.2) was used in a measurement. The coded aperture has a $10 \times 10\,\text{mm}^2$ grid of $1 \times 1\,\text{mm}^2$ cells. The pinholes[6] were cut to $0.8 \times 0.8\,\text{mm}^2$ sizes with spacers of 0.1 mm thickness between neighbouring pinholes. There were 34 open holes, accounting for 1/3 of the total surface. For the measurement, we used the sample 1 from Tab. 6.1 with the TUM and TUDelft patterns.
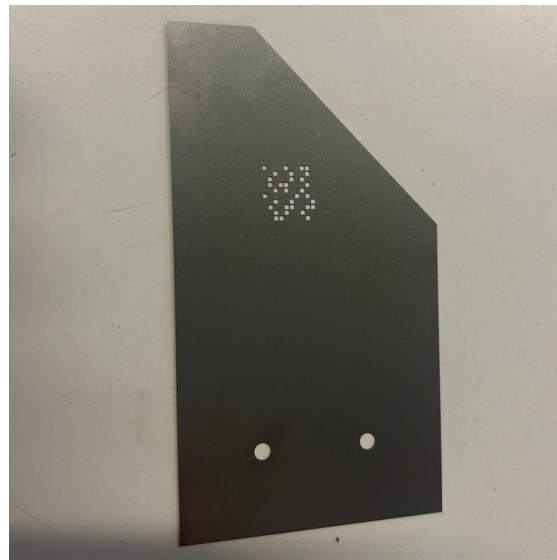
Figure 7.2.: Coded mask aperture used in the Delft experiment. Instead of a pinhole aperture, we placed the coded mask in front of the first detector. A randomized pattern in a $10 \times 10\,\text{mm}^2$ grid with an open fraction of 1/3 was used.

As in Sec. 6.2, we ran some Monte Carlo simulations using the coded mask. The simulations show that the entire TUM pattern is visible through the coded mask, and the efficiency of each pixel on the sample plane can be determined. For the simulated detector image, we observe a multiplexed picture of the pinholes (Fig. 7.3a). It shows a similar stripe pattern for the real measurement (shown in Fig. 7.3b). It should be possible to reconstruct the pattern on the sample plane using different approaches: deterministic method, statistical modeling (such as Bayesian method or maximum likelihood), and convolutional neural networks (CNN) [164]. The analysis of this method is still ongoing, and could be the topic for further research in this area.

---

[6]Laser cut by Becktronic GmbH
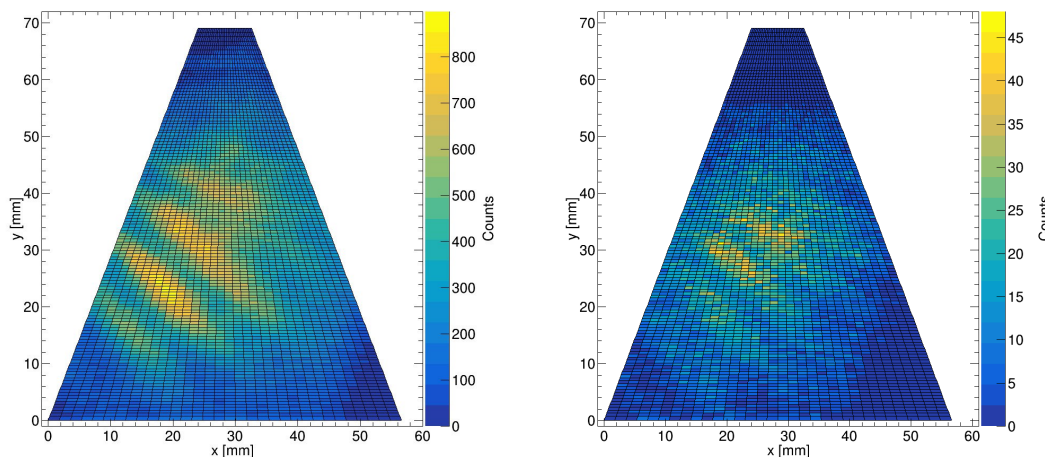
(a) Simulated detector response with TUM cut. **(b)** Detector data from the Delft experiment.

Figure 7.3.: Simulated and acquired data with the coded mask aperture. The simulated detector response of the TUM pattern is now a convolution of multiple pinhole responses, showing a stripe pattern on the detector. The real data shows a very similar pattern. For this data, an energy filter was used for the α and triton particles from the TUM pattern at $2.0\,\text{MeV}$ and $2.7\,\text{MeV}$, respectively.

7.3.5   Battery Research
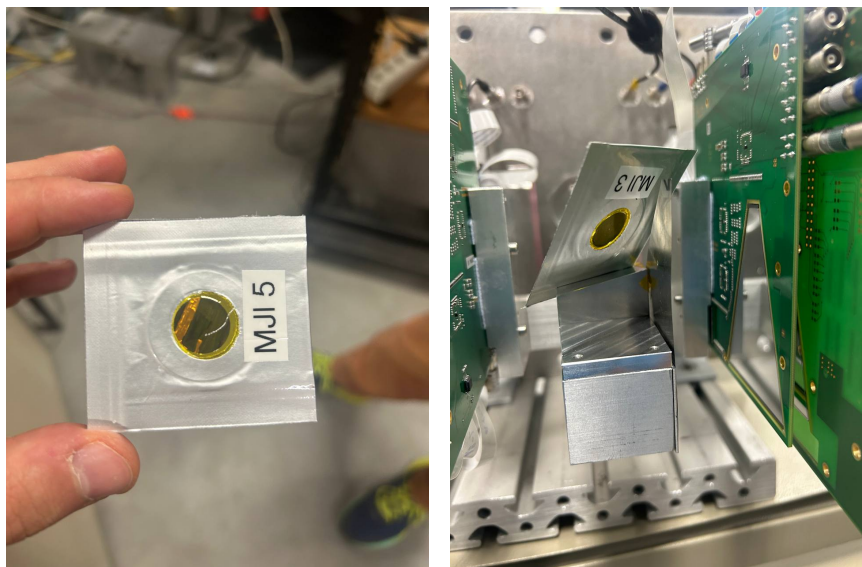
(a) Sealed thin battery.   **(b)** Battery mounted in the setup.

Figure 7.4.: Thin battery cells probed with the setup shown in Chap. 6. Unfortunately, the sealed cells opened up during the vacuuming process.

For the beam time in Delft, a collaboration partner from the TUM chemistry department provided us with different thin battery samples, as shown in Fig. 7.4a,b. These samples corresponded to different types of batteries and were to be tested for homogeneity of the Li filling over the surface and in-depth (3D). We measured these samples with the new detector system. These batteries were vacuum sealed at a pressure two orders of magnitude higher than the vacuum we used in the Delft experiment ($\sim 10^{-3}$ mbar). As a result, unfortunately, most of the batteries opened up during the measurements. Therefore, most of the data serves only to demonstrate that it is indeed possible to measure batteries *in-situ* using this method. This enables future battery research with the N4DP instrument using the DSSSD setup.

APPENDIX A

Detector PCB Design
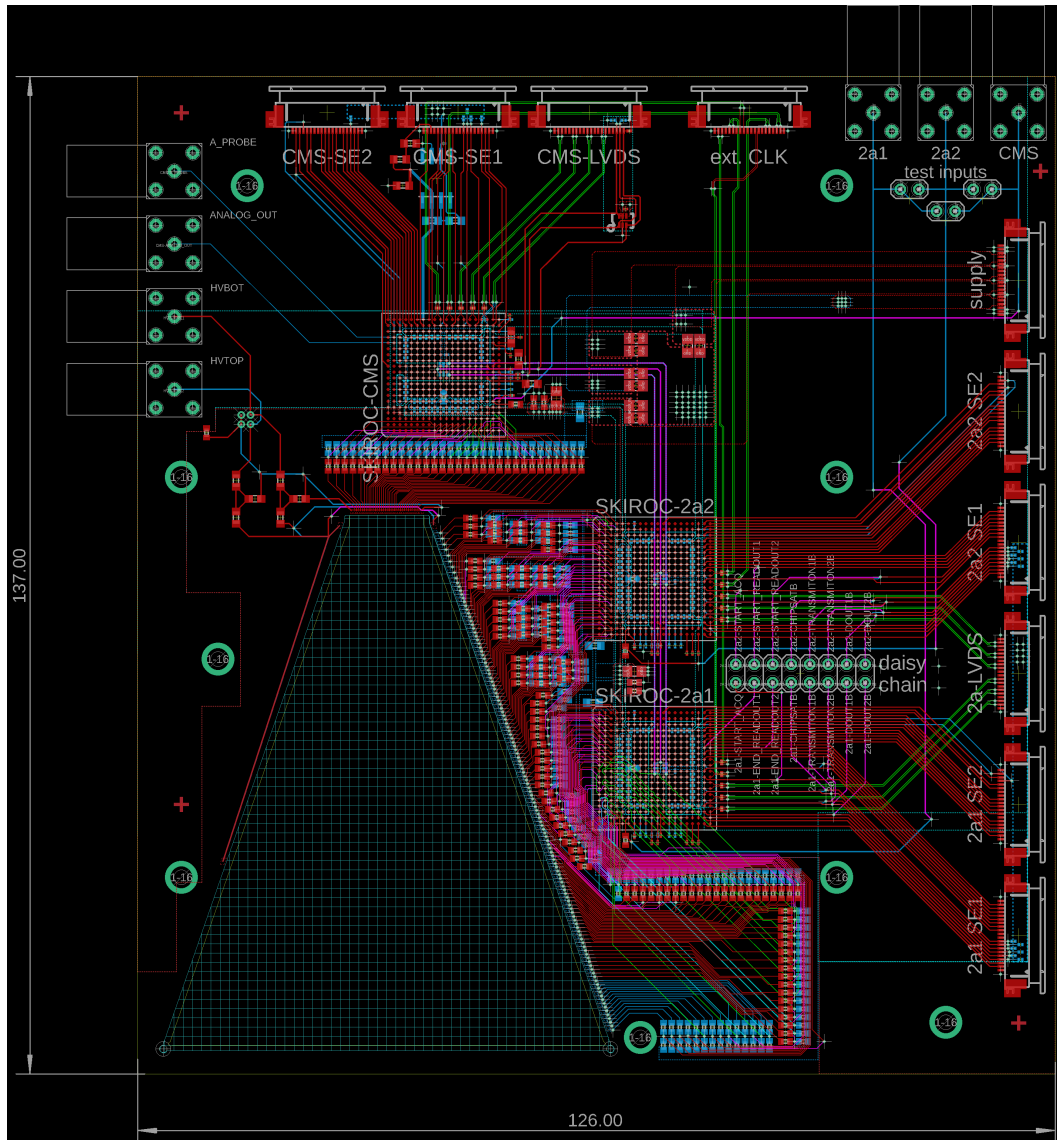
Figure A.1.: 6-layer detector board layout. The blue trapezoidal grid marks the detector area. The SKIROC ASICs in BGA400 packages are shown in the red top layer. Most line widths, such as signal lines, and their spacings are 100 μm. Some signal lines, such as the ones for the HV, are 200-μm-thick. The circles in green are the vias with 300 μm diameter, used not only for grounding but also for fixing the board to support structures. Some (white) labels can be seen on the board, such as test inputs for all the chips, supplies, HV, and a pin header for a daisy chain. This chain can be used to couple the SKIROC chips to external chips.

Data structures of the ASICs

The two figures Fig. B.1 and Fig. B.2 show the memory mapping of the two chips used for the electronics. After the readout, these structures are contained in so-called dabc files and deciphered with custom-programmed software.
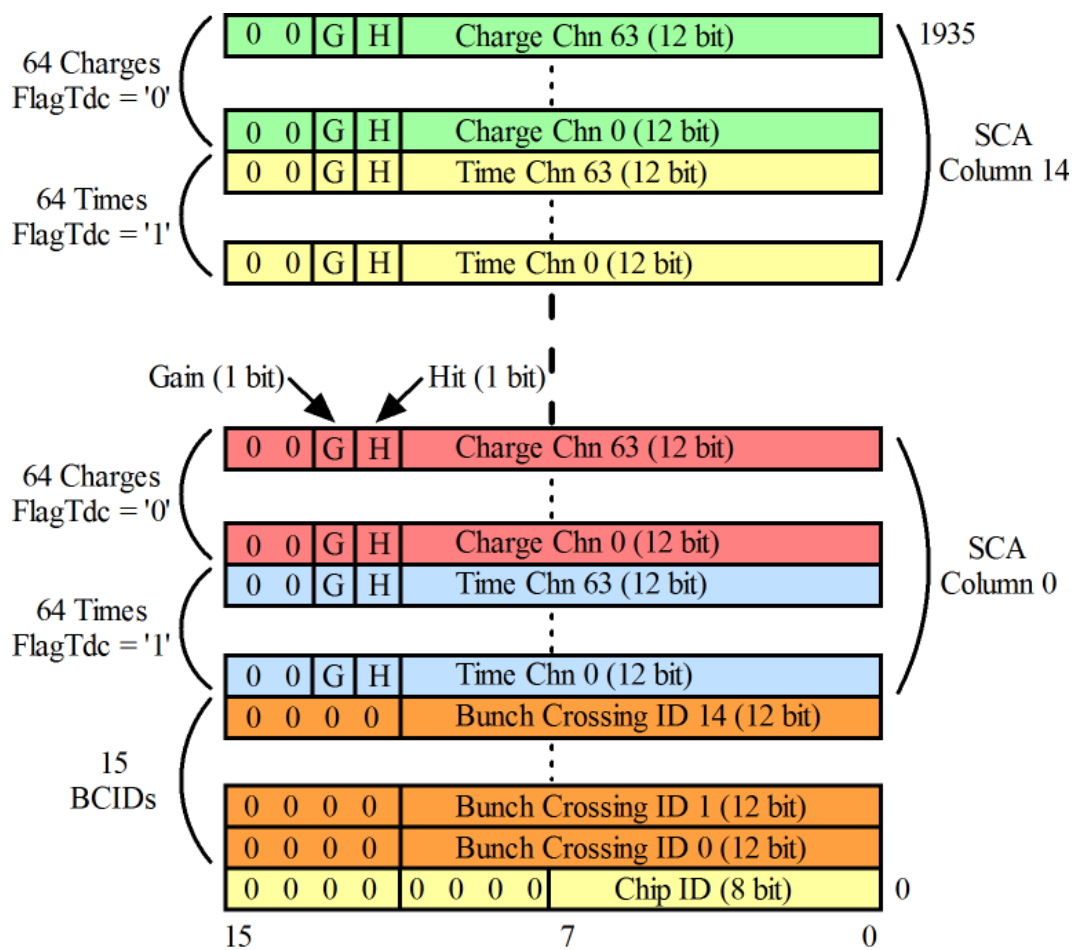
**Figure B.1.:** SKIROC 2A data structure.
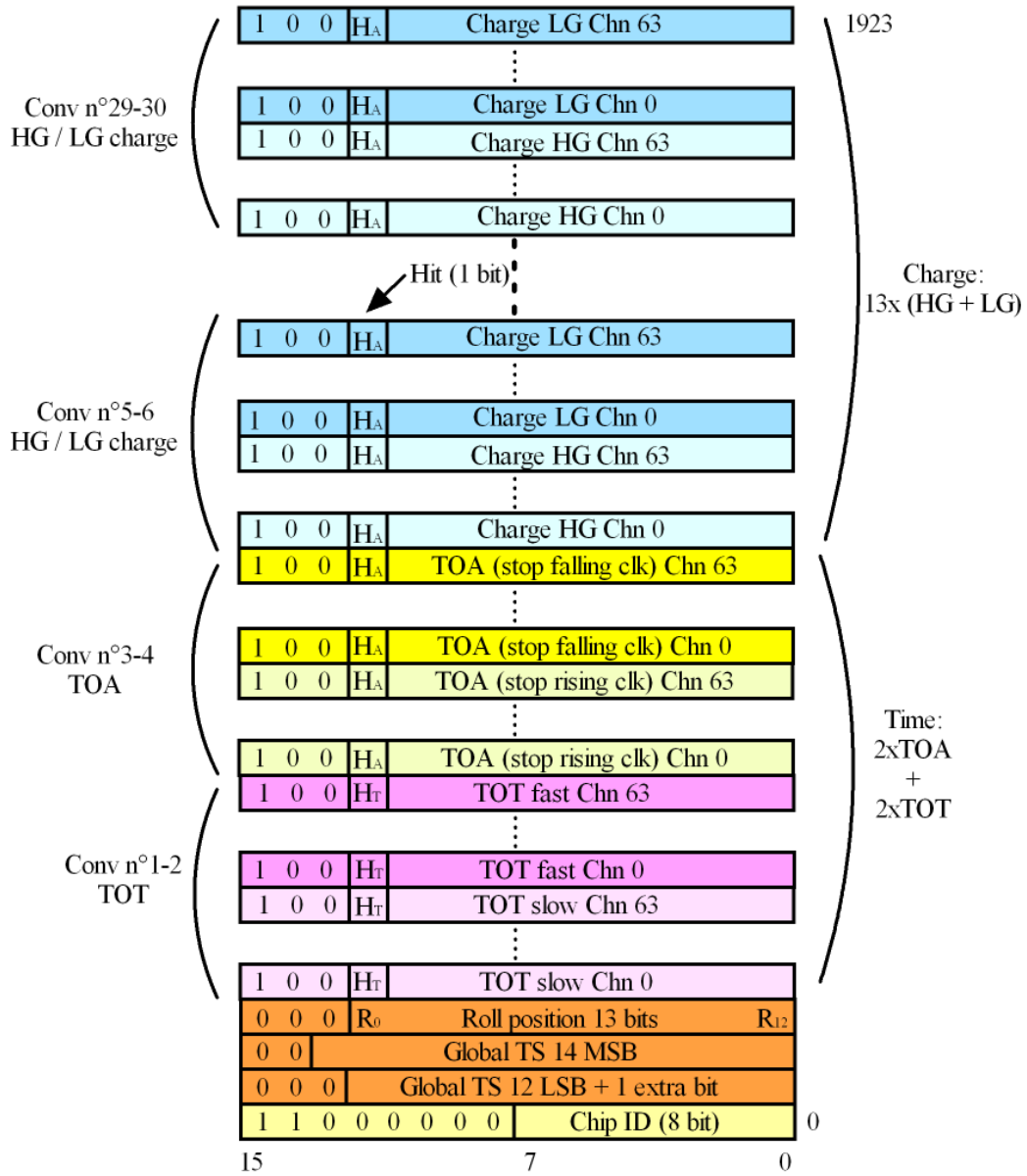
Figure B.2.: SKIROC CMS data structure.

Data

C.1 Laboratory Data
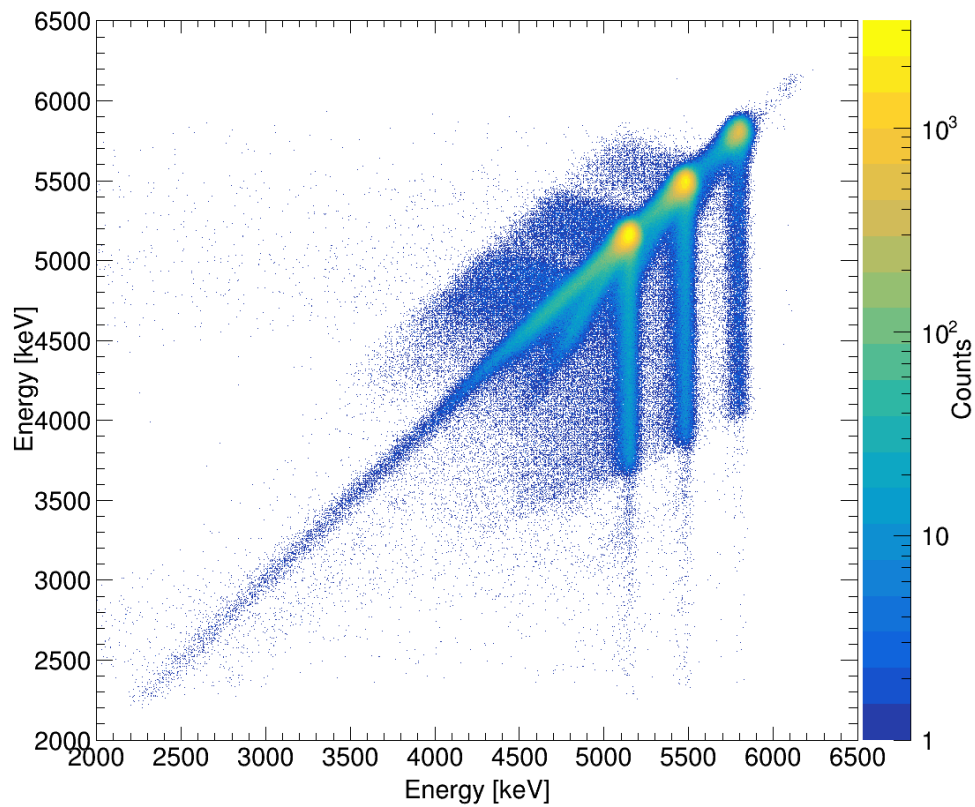
Figure C.1.: Front versus back side calibrated energy with the α emitter. A long tail is observed, corresponding to particles losing energy before entering the detector's active volume. The straight vertical and horizontal lines correspond to some remaining charge sharing between p and n strips.

C.2   Krakow Data

(a) Non-filtered.   **(b)** Filtered.
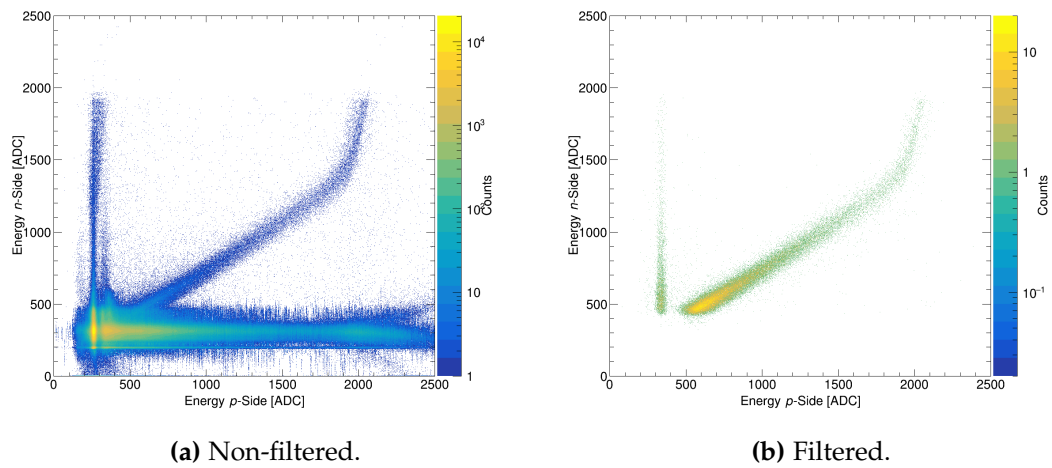
Figure C.2.: Events from the 120 MeV proton beam in detector 3 correlated within its
p and *n* sides. Only data from one SKIROC 2A chip was used here. The
x axis represents the energy on the *p* side, while the *y* axis represents the
n side. On the diagonal, we observe the Landau distribution from the
proton's energy loss on both sides of the detector. The energy loss in the
detector is low in this case; therefore, the preamplifiers were tuned up.
Thus, we observe the non-linearity of the ASICs above ~ 2000 ADC.

(a) Non-filtered.   **(b)** Filtered.
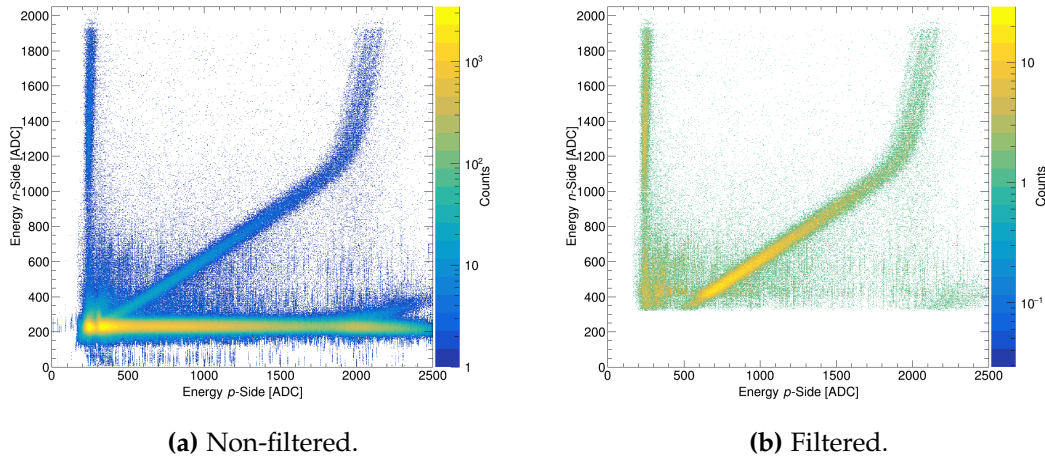
Figure C.3.: Events from the 200 MeV proton beam in detector 3 correlated within its
 p and *n* sides. Only data from one SKIROC 2A chip was used here. The
 x axis represents the energy on the *p* side, while the *y* axis represents the
 n side. On the diagonal, we observe the Landau distribution from the
 proton's energy loss on both sides of the detector. The energy loss in the
 detector is low in this case; therefore, the preamplifiers were tuned up.
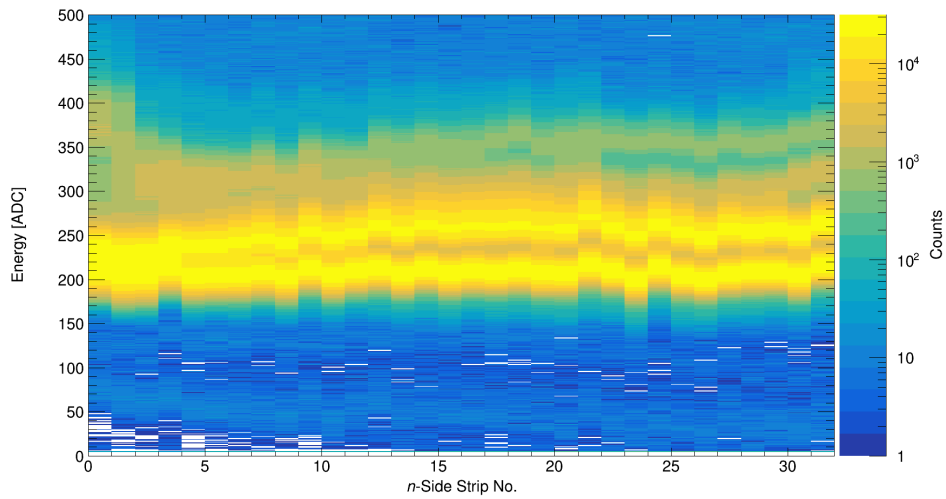 Thus, we observe the non-linearity of the ASICs above ~ 2000 ADC.

C.3 Delft Data
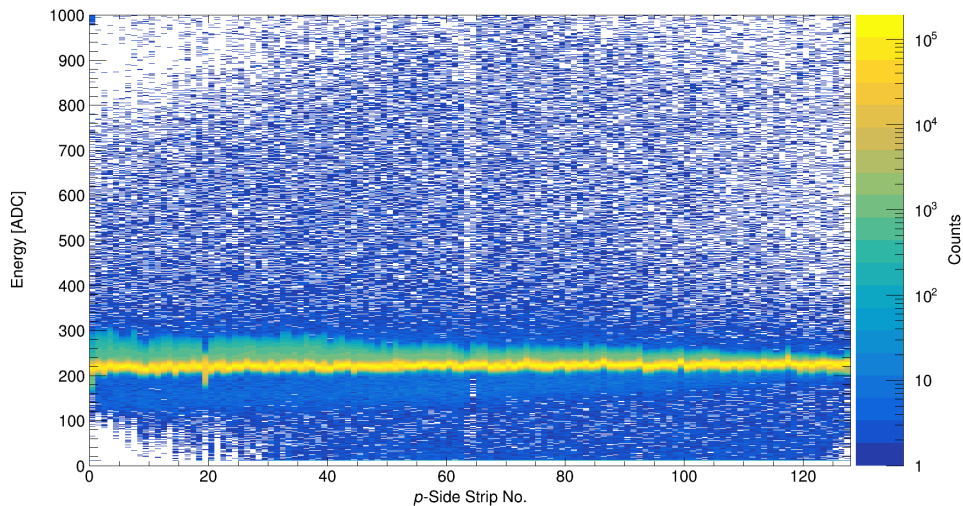
Figure C.4.: Baseline in detector 1 for the *p* strips. We observe a constant electronic
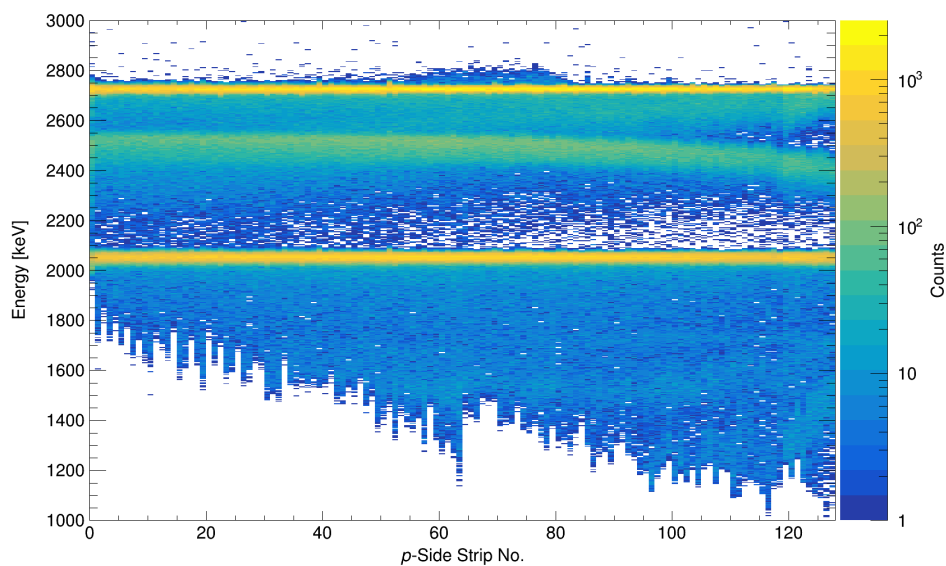 noise at ~ 230 ADC for all the channels.
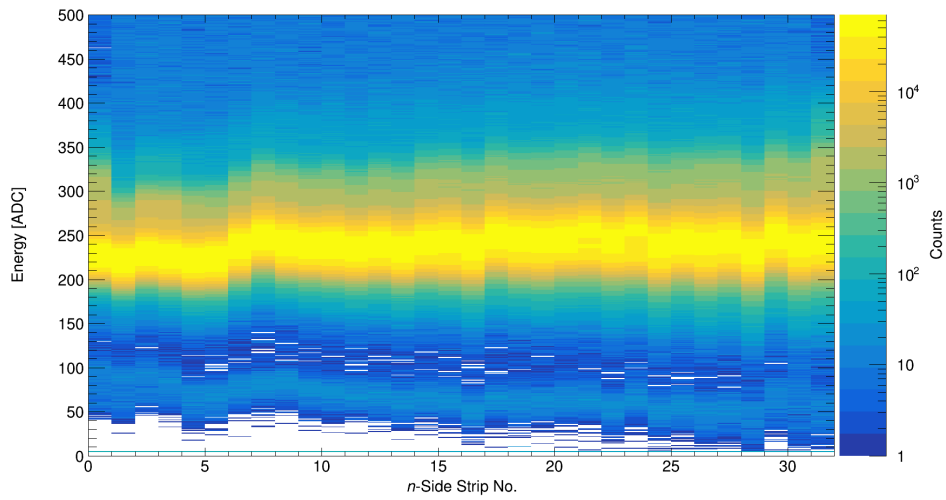
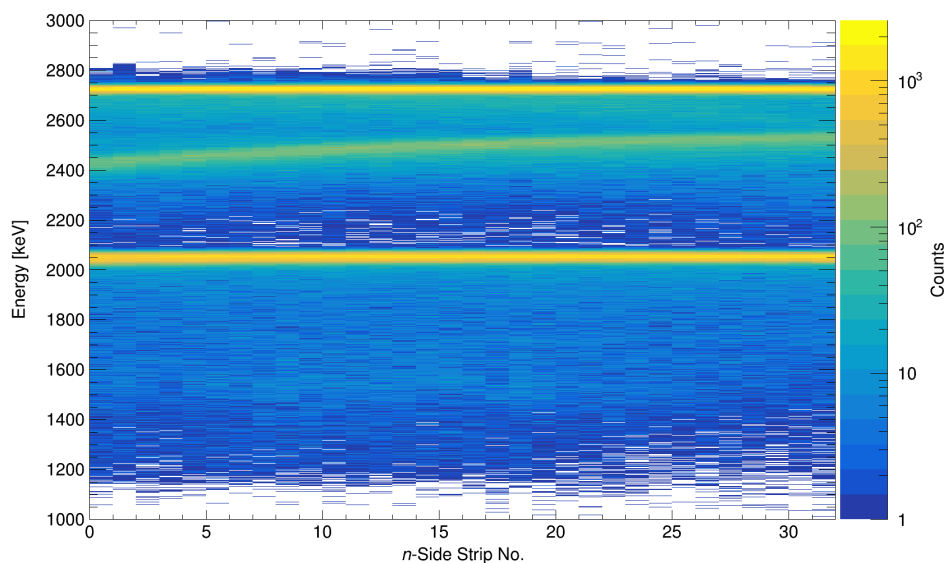**(a)** *n* channels versus energy detector 1.

(b) *n* channels versus energy detector 2.

Figure C.5.: Baseline in both detectors on the *x* axis (*n* strips). We observe a rather constant baseline at ~ 230 ADC for all the channels.

(a) *p* channels versus energy.

(b) *n* channels versus energy.

Figure C.6.: Energy spectra on the *y* axis (*p* strips) and on the *x* axis (*n* strips) for detector 1. We observe tritons and α particles at 2.73 MeV and 2.05 MeV from the sample side facing the detector, and triton particles at ~ 2.50 MeV from the second side of the sample.

Bibliography

[1]   J. M. Tarascon, "The Li-Ion Battery: 25 Years of Exciting and Enriching Experiences", in: *Interface magazine*, vol. 25, no. 3, Jan. 2016, pp. 79–83. [DOI].

[2]   R. Korthauer and M. Wuest, *Lithium-ion batteries: basics and applications*. Springer, 2018. ISBN: 978-3-662-53071-9.

[3]   G. Pasini, G. Lutzemberger, and L. Ferrari, "Renewable Electricity for Decarbonisation of Road Transport: Batteries or E-Fuels?", in: *Batteries*, vol. 9, no. 2, Feb. 2023, p. 135. [DOI].

[4]   F. Ueckerdt, C. Bauer, A. Dirnaichner, J. Everall, R. Sacchi, and G. Luderer, "Potential and risks of hydrogen-based e-fuels in climate change mitigation", in: *Nature Climate Change*, vol. 11, no. 5, May 2021, pp. 384–393. [DOI].

[5]   H. Hesse, M. Schimpe, D. Kucevic, and A. Jossen, "Lithium-Ion Battery Storage for the Grid—A Review of Stationary Battery Storage System Design Tailored for Applications in Modern Power Grids", in: *Energies*, vol. 10, no. 12, Dec. 2017, p. 2107. [DOI].

[6]   J. W. Choi and D. Aurbach, "Promise and reality of post-lithium-ion batteries with high energy densities", in: *Nature Reviews Materials*, vol. 1, no. 4, Mar. 2016, p. 16013. [DOI].

[7]   M. T. McDowell, S. W. Lee, W. D. Nix, and Y. Cui, "25th Anniversary Article: Understanding the Lithiation of Silicon and Other Alloying Anodes for Lithium-Ion Batteries", in: *Advanced Materials*, vol. 25, no. 36, Sept. 2013, pp. 4966–4985. [DOI].

[8]   S. J. An, J. Li, C. Daniel, D. Mohanty, S. Nagpure, and D. L. Wood, "The state of understanding of the lithium-ion-battery graphite solid electrolyte interphase (SEI) and its relationship to formation cycling", in: *Carbon*, vol. 105, Aug. 2016, pp. 52–76. [DOI].

[9]   E. Rutherford, "Bakerian Lecture: Nuclear constitution of atoms", in: *Proceedings of the Royal Society of London. Series A, Containing Papers of a Mathematical and Physical Character*, vol. 97, no. 686, July 1920, pp. 374–400. [DOI].

[10]   J. Chadwick, "Possible Existence of a Neutron", in: *Nature*, vol. 129, no. 3252, Feb. 1932, pp. 312–312. [DOI].

[11]   A. Ali, Y. W. Chiang, and R. M. Santos, "X-ray Diffraction Techniques for Mineral Characterization: A Review for Engineers of the Fundamentals, Applications, and Research Directions", in: *Minerals*, vol. 12, no. 2, Feb. 2022, p. 205. [DOI].

[12]   M. Magdy, "X-Ray Techniques Dedicated to Materials Characterization in Cultural Heritage", in: *ChemistrySelect*, vol. 8, no. 33, Sept. 2023, e202301306. [DOI].

[13]   A. V. Walker, "Secondary Ion Mass Spectrometry", in: *Encyclopedia of Spectroscopy and Spectrometry*. Elsevier, 2017, pp. 44–49. [DOI].

[14] K. Schaepe, H. Jungnickel, T. Heinrich, J. Tentschert, A. Luch, and W. E. Unger, "Secondary ion mass spectrometry", in: *Characterization of Nanoparticles*. Elsevier, 2020, pp. 481–509. [DOI].

[15] E. H. Kisi and C. J. Howard, *Applications of neutron powder diffraction*. Oxford series on neutron scattering in condensed matter 15. Oxford University Press, 2008. 486 pp. ISBN: 978-0-19-851594-4.

[16] G. Zaccai and B. Jacrot, "Small Angle Neutron Scattering", in: *Annual Review of Biophysics and Bioengineering*, vol. 12, no. 1, June 1983, pp. 139–157. [DOI].

[17] X.-L. Zhou and S.-H. Chen, "Theoretical foundation of X-ray and neutron reflectometry", in: *Physics Reports*, vol. 257, no. 4, June 1995, pp. 223–348. [DOI].

[18] J. Daillant, A. Gibaud, and A. Gibaud, eds., *X-ray and neutron reflectivity: principles and applications*. 2. ed. Lecture notes in physics 770. Springer, 2009. 348 pp.

[19] G. L. Squires, *Introduction to the theory of thermal neutron scattering*. Dover Publications, 1996. 260 pp. ISBN: 978-0-486-69447-4.

[20] B. Winkler, "Applications of Neutron Radiography and Neutron Tomography", in: *Reviews in Mineralogy and Geochemistry*, vol. 63, no. 1, Jan. 2006, pp. 459–471. [DOI].

[21] E. Witkowska, K. Szczepaniak, and M. Biziuk, "Some applications of neutron activation analysis: A review", in: *Journal of Radioanalytical and Nuclear Chemistry*, vol. 265, no. 1, June 2005, pp. 141–150. [DOI].

[22] R. Downing, G. Lamaze, J. Langland, and S. Hwang, "Neutron depth profiling: Overview and description of NIST facilities", in: *Journal of Research of the National Institute of Standards and Technology*, vol. 98, no. 1, Jan. 1993, p. 109. [DOI].

[23] S. Whitney, S. R. Biegalski, Y. H. Huang, and J. B. Goodenough, "Neutron Depth Profiling Applications to Lithium-Ion Cell Research", in: *Journal of The Electrochemical Society*, vol. 156, no. 11, 2009, A886. [DOI].

[24] M. Wetjen, M. Trunk, L. Werner, H. A. Gasteiger, R. Gernhäuser, R. Gilles, B. Märkisch, and Z. Révay, "Monitoring the Lithium Concentration across the Thickness of Silicon-Graphite Electrodes during the First (De-)Lithiation", in: *Journal of The Electrochemical Society*, vol. 166, no. 8, 2019, A1408–A1411. [DOI].

[25] E. Moyassari, L. Streck, N. Paul, M. Trunk, R. Neagu, C.-C. Chang, S.-C. Hou, B. Märkisch, R. Gilles, and A. Jossen, "Impact of Silicon Content within Silicon-Graphite Anodes on Performance and Li Concentration Profiles of Li-Ion Cells using Neutron Depth Profiling", in: *Journal of The Electrochemical Society*, vol. 168, no. 2, Feb. 2021, p. 020519. [DOI].

[26] T. W. Verhallen, S. Lv, and M. Wagemaker, "Operando Neutron Depth Profiling to Determine the Spatial Distribution of Li in Li-ion Batteries", in: *Frontiers in Energy Research*, vol. 6, July 2018, p. 62. [DOI].

[27] Y. He, R. G. Downing, and H. Wang, "3D mapping of lithium in battery electrodes using neutron activation", in: *Journal of Power Sources*, vol. 287, Aug. 2015, pp. 226–230. [DOI].

[28] I. Tomandl, J. Vacík, Y. Mora Sierra, C. Granja, and V. Kraus, "High resolution imaging of 2D distribution of lithium in thin samples measured with multipixel detectors in sandwich geometry", in: *Review of Scientific Instruments*, vol. 88, no. 2, Feb. 2017, p. 023706. [DOI].

[29] J. Lichtinger, R. Gernhäuser, A. Bauer, M. Bendel, L. Canella, M. Graw, R. Krücken, P. Kudejova, E. Mützel, S. Ring, D. Seiler, S. Winkler, K. Zeitelhack, and J. Schöpfer, "Position sensitive measurement of lithium traces in brain tissue with neutrons: Position sensitive measurement of lithium traces in brain tissue with neutrons", in: *Medical Physics*, vol. 40, no. 2, Jan. 2013, p. 023501. [DOI].

[30] E. Portenkirchner, G. Neri, J. Lichtinger, J. Brumbarov, C. Rüdiger, R. Gernhäuser, and J. Kunze-Liebhäuser, "Tracking areal lithium densities from neutron activation – quantitative Li determination in self-organized TiO_2 nanotube anode materials for Li-ion batteries", in: *Physical Chemistry Chemical Physics*, vol. 19, no. 12, 2017, pp. 8602–8611. [DOI].

[31] J. Schoepfer, R. Gernhäuser, S. Lichtinger, A. Stöver, M. Bendel, C. Delbridge, T. Widmann, S. Winkler, and M. Graw, "Position sensitive measurement of trace lithium in the brain with NIK (neutron-induced coincidence method) in suicide", in: *Scientific Reports*, vol. 11, no. 1, Mar. 2021, p. 6823. [DOI].

[32] M. Lindroos and Ö. Skeppstedt, "A position sensitive photon detector used as a charged particle detector", in: *Nuclear Instruments and Methods in Physics Research Section A: Accelerators, Spectrometers, Detectors and Associated Equipment*, vol. 306, no. 1, Aug. 1991, pp. 225–228. [DOI].

[33] F. Linsenmann, M. Trunk, P. Rapp, L. Werner, R. Gernhäuser, R. Gilles, B. Märkisch, Z. Révay, and H. A. Gasteiger, "A Liquid Electrolyte-Based Lithium-Ion Battery Cell Design for Operando Neutron Depth Profiling", in: *Journal of The Electrochemical Society*, vol. 167, no. 10, Jan. 2020, p. 100554. [DOI].

[34] C. W. Fabjan and H. Schopper, eds., *Particle Physics Reference Library: Volume 2: Detectors for Particles and Radiation*. Springer International Publishing, 2020. [DOI].

[35] W. d. Physik, *Die neue Beschleunigeranlage von FAIR*. [online] (visited on 10/14/2024).

[36] L. Werner, M. Trunk, R. Gernhäuser, R. Gilles, B. Märkisch, and Z. Révay, "The new neutron depth profiling instrument N4DP at the Heinz Maier-Leibnitz Zentrum", in: *Nuclear Instruments and Methods in Physics Research Section A: Accelerators, Spectrometers, Detectors and Associated Equipment*, vol. 911, Dec. 2018, pp. 30–36. [DOI].

[37] J. Biersack, D. Fink, J. Lauch, R. Henkelmann, and K. Müller, "An instrument for lattice location studies of light impurity atoms by means of (n, α)-reactions", in: *Nuclear Instruments and Methods in Physics Research*, vol. 188, no. 2, Sept. 1981, pp. 411–419. [DOI].

[38] C. Berner, L. Werner, R. Gernhäuser, and T. Kröll, "HI-TREX—A highly integrated transfer setup at REX-(HIE)ISOLDE", in: *Nuclear Instruments and Methods in Physics Research Section A: Accelerators, Spectrometers, Detectors and Associated Equipment*, vol. 987, Jan. 2021, p. 164827. [DOI].

[39]   E. Vezhlev, A. Ioffe, S. Mattauch, S. Staringer, V. Ossovyi, C. Felder, E. Hüger, J. Vacik, I. Tomandl, V. Hnatowicz, C. Chen, P. Notten, and T. Brückel, "A new neutron depth profiling spectrometer at the JCNS for a focused neutron beam", in: *Radiation Effects and Defects in Solids*, vol. 175, no. 3, Mar. 2020, pp. 342–355. [DOI].

[40]   T. Chanjuan, X. Caijin, Y. Yonggang, S. Cong, J. Xiangchun, Y. Weixu, L. Xudong, N. Bangfa, and W. Pingsheng, "Neutron depth profiling system at CARR", in: *Applied Radiation and Isotopes*, vol. 148, June 2019, pp. 102–107. [DOI].

[41]   B. Park, G. Sun, and H. Choi, "Development of cold neutron depth profiling system at HANARO", in: *Nuclear Instruments and Methods in Physics Research Section A: Accelerators, Spectrometers, Detectors and Associated Equipment*, vol. 752, July 2014, pp. 20–26. [DOI].

[42]   H. Schmidt, "Kompakte schachbrett-detektor-elektronik für blocking-experimente", in: *Nuclear Instruments and Methods*, vol. 141, no. 1, Feb. 1977, pp. 165–172. [DOI].

[43]   J. F. Ziegler, G. W. Cole, and J. E. E. Baglin, "Technique for determining concentration profiles of boron impurities in substrates", in: *Journal of Applied Physics*, vol. 43, no. 9, Sept. 1972, pp. 3809–3815. [DOI].

[44]   J. Ziegler, B. Crowder, G. Cole, J. Baglin, and B. Masters, "Boron atom distributions in ion-implanted silicon by the $(n,{}^4\text{He})$ nuclear reaction", in: *Applied Physics Letters*, vol. 21, no. 1, July 1972, pp. 16–17. [DOI].

[45]   T. Kobayashi, T. Ohnishi, T. Osawa, A. Pratt, S. Tear, S. Shimoda, H. Baba, M. Laitinen, and T. Sajavaara, "In-Operando Lithium-Ion Transport Tracking in an All-Solid-State Battery", in: *Small*, vol. 18, no. 46, Nov. 2022, p. 2204455. [DOI].

[46]   M. Frankenberger, M. Trunk, S. Seidlmayer, A. Dinter, J. Dittloff, L. Werner, R. Gernhäuser, Z. Revay, B. Märkisch, R. Gilles, and K.-H. Pettinger, "SEI Growth Impacts of Lamination, Formation and Cycling in Lithium Ion Batteries", in: *Batteries*, vol. 6, no. 2, Mar. 2020, p. 21. [DOI].

[47]   F. Linsenmann, P. Rapp, M. Trunk, R. Gernhäuser, J. L. Weaver, B. Märkisch, and H. A. Gasteiger, "Spatially and Time-Resolved Investigation of Lithium Plating on a Graphite Electrode during Fast Charging Using Operando Neutron Depth Profiling (NDP)", in: *ECS Meeting Abstracts*, vol. MA2020-01, no. 2, May 2020, pp. 144–144. [DOI].

[48]   C. Chen, M. Jiang, T. Zhou, L. Raijmakers, E. Vezhlev, B. Wu, T. U. Schülli, D. L. Danilov, Y. Wei, R.-A. Eichel, and P. H. L. Notten, "Interface Aspects in All-Solid-State Li-Based Batteries Reviewed", in: *Advanced Energy Materials*, vol. 11, no. 13, Apr. 2021, p. 2003939. [DOI].

[49]   Z. Révay, "Determining Elemental Composition Using Prompt γ Activation Analysis", in: *Analytical Chemistry*, vol. 81, no. 16, Aug. 2009, pp. 6851–6859. [DOI].

[50]   V. McLane, *Neutron Cross Sections*. Neutron cross sections series. Elsevier Science, 2012. ISBN: 978-0-323-14222-9. [online].

[51]   *Neutron Depth Profiling - Reactions of Interest*. [online] (visited on 12/18/2023).

[52]   A. J. Dianoux and I. Laue-Langevin, eds., *Neutron data booklet*. 2. ed. Old City, 2003.

[53]   M. Trunk, M. Wetjen, L. Werner, R. Gernhäuser, B. Märkisch, Z. Révay, H. Gasteiger, and R. Gilles, "Materials science applications of Neutron Depth Profiling at the PGAA facility of Heinz Maier-Leibnitz Zentrum", in: *Materials Characterization*, vol. 146, Dec. 2018, pp. 127–134. [DOI].

[54]   C. Sheehan, W. J. Lennard, and J. B. A. Mitchell, "Measurement of the efficiency of a silicon surface barrier detector for medium energy ions using a Rutherford backscattering experiment", in: *Measurement Science and Technology*, vol. 11, no. 8, Aug. 2000, pp. L5–L7. [DOI].

[55]   W. R. Leo, *Techniques for Nuclear and Particle Physics Experiments*. Springer Berlin Heidelberg, 1994. ISBN: 978-3-540-57280-0. [DOI].

[56]   K. Nakamura, "Review of Particle Physics", in: *Journal of Physics G: Nuclear and Particle Physics*, vol. 37, no. 7, July 2010, p. 075021. [DOI].

[57]   H. Gümüş and F. Köksal, "Effective stopping charges and stopping power calculations for heavy ions", in: *Radiation Effects and Defects in Solids*, vol. 157, no. 5, Jan. 2002, pp. 445–458. [DOI].

[58]   H. Bethe, "Bremsformel für Elektronen relativistischer Geschwindigkeit", in: *Zeitschrift für Physik*, vol. 76, no. 5, May 1932, pp. 293–299. [DOI].

[59]   J. F. Ziegler, "Stopping of energetic light ions in elemental matter", in: *Journal of Applied Physics*, vol. 85, no. 3, Feb. 1999, pp. 1249–1272. [DOI].

[60]   M. A. Nastasi, J. W. Mayer, and J. K. Hirvonen, *Ion-solid interactions: fundamentals and applications*. Cambridge solid state science series. Cambridge University Press, 1996. 540 pp. ISBN: 978-0-521-37376-0.

[61]   N. I. of Standards {and} Technology, *CODATA Value: molar mass constant*. [online] (visited on 01/16/2024).

[62]   W. W. M. Allison and J. H. Cobb, "Relativistic Charged Particle Identification by Energy Loss", in: *Annual Review of Nuclear and Particle Science*, vol. 30, no. 1, Dec. 1980, pp. 253–298. [DOI].

[63]   H. Kolanoski and N. Wermes, *Particle detectors: fundamentals and applications*. Oxford University Press, 2020. 927 pp. ISBN: 978-0-19-885836-2.

[64]   J. Biersack, D. Fink, R. Henkelmann, and K. Müller, "The use of neutron induced reactions for light element profiling and lattice localization", in: *Nuclear Instruments and Methods*, vol. 149, no. 1, Feb. 1978, pp. 93–97. [DOI].

[65]   J. T. Maki, R. F. Fleming, and D. H. Vincent, "Deconvolution of neutron depth profiling spectra", in: *Nuclear Instruments and Methods in Physics Research Section B: Beam Interactions with Materials and Atoms*, vol. 17, no. 2, Sept. 1986, pp. 147–155. [DOI].

[66]   C. Grupen and B. A. Shwartz, *Particle detectors*. 2nd ed. Cambridge monographs on particle physics, nuclear physics and cosmology 26. Cambridge university press, 2011. ISBN: 978-0-521-18795-4.

[67] H. Spieler, *Semiconductor detector systems*. Series on semiconductor science and technology 12. Oxford University Press, 2005. 489 pp. ISBN: 978-0-19-852784-8.

[68] Particle Data Group, R. L. Workman, V. D. Burkert, et al., "Review of Particle Physics", in: *Progress of Theoretical and Experimental Physics*, vol. 2022, no. 8, Aug. 2022, p. 083C01. [DOI].

[69] CERN. Geneva. The LHC Experiments Committee, D. Contardo, M. Klute, J. Mans, L. Silvestris, and J. Butler, "Technical Proposal for the Phase-II Upgrade of the CMS Detector", in: 2015. In collab. with D. Contardo, M. Klute, J. Mans, L. Silvestris, and J. Butler. [DOI].

[70] ATLAS Collaboration and CERN. Geneva. LHC Experiments Committee, "ATLAS liquid-argon calorimeter: Technical Design Report", in: 1997. [DOI].

[71] K. Kleinknecht, *Detectors for particle radiation*. 2nd ed. Cambridge University Press, 1998. 246 pp. ISBN: 978-0-521-64032-9.

[72] F. Hartmann, "Silicon tracking detectors in high-energy physics", in: *Nuclear Instruments and Methods in Physics Research Section A: Accelerators, Spectrometers, Detectors and Associated Equipment*, vol. 666, Feb. 2012, pp. 25–46. [DOI].

[73] G. Lutz, *Semiconductor Radiation Detectors*. Springer Berlin Heidelberg, 2007. ISBN: 978-3-540-71678-5. [DOI].

[74] W. Shockley, "Currents to Conductors Induced by a Moving Point Charge", in: *Journal of Applied Physics*, vol. 9, no. 10, Oct. 1938, pp. 635–636. [DOI].

[75] S. Ramo, "Currents Induced by Electron Motion", in: *Proceedings of the IRE*, vol. 27, no. 9, Sept. 1939, pp. 584–585. [DOI].

[76] Collaboration: Authors and Editors of the LB Volumes III/17A-22A-41A1b, "1) Silicon (Si), electron mobility", in: *Group IV Elements, IV-IV and III-V Compounds. Part b - Electronic, Transport, Optical and Other Properties*. Ed. by O. Madelung, U. Rössler, and M. Schulz. Vol. b, Springer-Verlag, 2002, pp. 1–12. [DOI].

[77] Collaboration: Authors and Editors of the LB Volumes III/17A-22A-41A1b, "2) Silicon (Si), hole mobility", in: *Group IV Elements, IV-IV and III-V Compounds. Part b - Electronic, Transport, Optical and Other Properties*. Ed. by O. Madelung, U. Rössler, and M. Schulz. Vol. b, Springer-Verlag, 2002, pp. 1–11. [DOI].

[78] N. Demaria, S. Albergo, M. Angarano, et al., "New results on silicon microstrip detectors of CMS tracker", in: *Nuclear Instruments and Methods in Physics Research Section A: Accelerators, Spectrometers, Detectors and Associated Equipment*, vol. 447, no. 1, June 2000, pp. 142–150. [DOI].

[79] E. Barberis, N. Cartiglia, C. LeVier, J. Rahn, P. Rinaldi, H.-W. Sadrozinski, R. Wichmann, T. Ohsugi, Y. Unno, H. Miyata, N. Tamura, and K. Yamamoto, "Capacitances in silicon microstrip detectors", in: *Nuclear Instruments and Methods in Physics Research Section A: Accelerators, Spectrometers, Detectors and Associated Equipment*, vol. 342, no. 1, Mar. 1994, pp. 90–95. [DOI].

[80] "On the theory of quantum mechanics", in: *Proceedings of the Royal Society of London. Series A, Containing Papers of a Mathematical and Physical Character*, vol. 112, no. 762, Oct. 1926, pp. 661–677. [DOI].

[81] A. Zannoni, "On the Quantization of the Monoatomic Ideal Gas", in: 1999. [DOI].

[82] U. Fano, "Ionization Yield of Radiations. II. The Fluctuations of the Number of Ions", in: *Physical Review*, vol. 72, no. 1, July 1947, pp. 26–29. [DOI].

[83] R. C. Alig, S. Bloom, and C. W. Struck, "Scattering by ionization and phonon emission in semiconductors", in: *Physical Review B*, vol. 22, no. 12, Dec. 1980, pp. 5565–5582. [DOI].

[84] W. Van Roosbroeck, "Theory of the Yield and Fano Factor of Electron-Hole Pairs Generated in Semiconductors by High-Energy Particles", in: *Physical Review*, vol. 139, no. 5, Aug. 1965, A1702–A1716. [DOI].

[85] G. Alkhazov, A. Komar, and A. Vorob'ev, "Ionization fluctuations and resolution of ionization chambers and semiconductor detectors", in: *Nuclear Instruments and Methods*, vol. 48, no. 1, Feb. 1967, pp. 1–12. [DOI].

[86] A. Ebrahimi, F. Feind, E. Fretwurst, E. Garutti, M. Hajheidari, R. Klanner, D. Pitzl, J. Schwandt, G. Steinbrueck, and I. Zoi, "Position reconstruction for segmented detectors", in: *Nuclear Instruments and Methods in Physics Research Section A: Accelerators, Spectrometers, Detectors and Associated Equipment*, vol. 1014, Oct. 2021, p. 165744. [DOI].

[87] F. Wang, B. Nachman, and M. Garcia-Sciveres, "Ultimate position resolution of pixel clusters with binary readout for particle tracking", in: *Nuclear Instruments and Methods in Physics Research Section A: Accelerators, Spectrometers, Detectors and Associated Equipment*, vol. 899, Aug. 2018, pp. 10–15. [DOI].

[88] H. Kolanoski and N. Wermes, *Teilchendetektoren: Grundlagen und Anwendungen*. Springer Spektrum, 2016. 921 pp. ISBN: 978-3-662-45349-0. [DOI].

[89] W. Riegler and G. A. Rinella, "Time resolution of silicon pixel sensors", in: *Journal of Instrumentation*, vol. 12, no. 11, Nov. 2017, P11017–P11017. [DOI].

[90] R. Neagu, S. Golenev, L. Werner, C. Berner, R. Gilles, Z. Revay, L. Ziegele, J. Plomp, B. Märkisch, and R. Gernhäuser, "4D Tomography for neutron depth profiling applications", in: *Nuclear Instruments and Methods in Physics Research Section A: Accelerators, Spectrometers, Detectors and Associated Equipment*, June 2024, p. 169543. [DOI].

[91] I. Agricola and T. Friedrich, *Elementary Geometry*. Trans. by P. Spain. Vol. 43. The Student Mathematical Library. American Mathematical Society, Feb. 2008. ISBN: 978-0-8218-4347-5. [DOI].

[92] R. R. Yarlagadda, "Convolution and Correlation", in: *Analog and Digital Signals and Systems*. Springer US, 2010, pp. 39–69. [DOI].

[93] R. N. Kacker and J. F. Lawrence, "Trapezoidal and triangular distributions for Type B evaluation of standard uncertainty", in: *Metrologia*, vol. 44, no. 2, Apr. 2007, pp. 117–127. [DOI].

[94] P. R. Garvey, S. A. Book, and R. P. Covert, *Probability methods for cost uncertainty analysis: a systems engineering perspective*. Second Edition. CRC Press, 2016. 501 pp. ISBN: 978-1-4822-1975-3.

[95]   D. Mukherji, R. Gilles, L. Karge, P. Strunz, P. Beran, H. Eckerlebe, A. Stark, L. Szentmiklosi, Z. Mácsik, G. Schumacher, I. Zizak, M. Hofmann, M. Hoelzel, and J. Rösler, "Neutron and synchrotron probes in the development of Co–Re-based alloys for next generation gas turbines with an emphasis on the influence of boron additives", in: *Journal of Applied Crystallography*, vol. 47, no. 4, Aug. 2014, pp. 1417–1430. [DOI].

[96]   A. Larsen, G. Bortels, and B. Denecke, "Satellite peaks in high-resolution alpha-particle spectra of decay-chain members measured with silicon surface-barrier detectors", in: *Nuclear Instruments and Methods in Physics Research*, vol. 219, no. 2, Jan. 1984, pp. 339–346. [DOI].

[97]   C. Berner, "Development of the compact, high resolution particle detection system HI-TREX", Dissertation. TUM, Oct. 2020. [online].

[98]   M. Quirk and J. Serda, *Semiconductor manufacturing technology*. Prentice Hall, 2001. 666 pp. ISBN: 978-0-13-081520-0.

[99]   R. F. K. Herzog and F. P. Viehböck, "Ion Source for Mass Spectrography", in: *Physical Review*, vol. 76, no. 6, Sept. 1949, pp. 855–856. [DOI].

[100] *Alpha spectroscopy sources*. Eckert & Ziegler Strahlen- und Medizintechnik AG. Aug. 2022. [online] (visited on 02/05/2024).

[101] R. Dalal, A. Bhardwaj, K. Ranjan, M. Moll, and A. Elliott-Peisert, "Combined effect of bulk and surface damage on strip insulation properties of proton irradiated n $^+$ -p silicon strip sensors", in: *Journal of Instrumentation*, vol. 9, no. 4, Apr. 2014, P04007–P04007. [DOI].

[102] R. Eber, "Investigations of new sensor designs and development of an effective radiation damage model for the simulation of highly irradiated silicon particle detectors", PhD thesis. Nov. 2013.

[103] CERN, "CERN Yellow Reports: Monographs, Vol 4 (2017): High-Luminosity Large Hadron Collider (HL-LHC) Technical Design Report V. 0.1", in: Sept. 2017, 29.94 MB. [DOI].

[104] W. Adam, T. Bergauer, E. Brondolin, et al., "P-Type Silicon Strip Sensors for the new CMS Tracker at HL-LHC", in: *Journal of Instrumentation*, vol. 12, no. 6, June 2017, P06018–P06018. [DOI].

[105] J. Sedlmeir, "Untersuchungen über einseitig und zweiseitig auslesbare Silizium-streifendetektoren", Dissertation. TUM, 1985.

[106] G. Lutz, P. Holl, J. Kemmer, U. Prechtel, J. Sedlmeir, L. Strüder, and W. Welser, "Present and Future Semiconductor Tracking Detectors", in: *Vertex Detectors*. Ed. by F. Villa. Springer US, 1988, pp. 195–224. [DOI].

[107] R. Richter, L. Andricek, T. Gebhart, D. Hauff, J. Kemmer, G. Lutz, R. Weiß, and A. Rolf, "Strip detector design for ATLAS and HERA-B using two-dimensional device simulation", in: *Nuclear Instruments and Methods in Physics Research Section A: Accelerators, Spectrometers, Detectors and Associated Equipment*, vol. 377, no. 2, Aug. 1996, pp. 412–421. [DOI].

[108]   G. Yang, R. Gram, P. Procel, C. Han, Z. Yao, M. Singh, Y. Zhao, L. Mazzarella, M. Zeman, and O. Isabella, "Will SiO -pinholes for SiO /poly-Si passivating contact enhance the passivation quality?", in: *Solar Energy Materials and Solar Cells*, vol. 252, Apr. 2023, p. 112200. [DOI].

[109]   R. C. Dorf and J. A. Svoboda, *Introduction to electric circuits*. 8th ed. John Wiley & Sons, 2010. 886 pp. ɪꜱʙɴ: 978-0-470-52157-1.

[110]   T. I. Westgaard, B. S. Avset, N. N. Ahmed, and L. Evensen, "Radiation hardness of punch-through and FET biased silicon microstrip detectors", in: *Nuclear Instruments and Methods in Physics Research Section A: Accelerators, Spectrometers, Detectors and Associated Equipment*, vol. 377, no. 2, Aug. 1996, pp. 429–434. [DOI].

[111]   L. Andricek, D. Hauff, J. Kemmer, P. Lükewille, G. Lutz, H. Moser, R. Richter, T. Rohe, K. Stolze, and A. Viehl, "Radiation hard strip detectors for large-scale silicon trackers", in: *Nuclear Instruments and Methods in Physics Research Section A: Accelerators, Spectrometers, Detectors and Associated Equipment*, vol. 436, no. 1, Oct. 1999, pp. 262–271. [DOI].

[112]   M. Da Rold, N. Bacchetta, D. Bisello, A. Paccagnella, G.-F. Dalla Betta, G. Verzellesi, O. Militaru, R. Wheadon, P. Fuochi, C. Bozzi, R. Dell'Orso, A. Messineo, G. Tonelli, and P. Verdini, "Study of breakdown effects in silicon multiguard structures", in: *IEEE Transactions on Nuclear Science*, vol. 46, no. 4, Aug. 1999, pp. 1215–1223. [DOI].

[113]   L. Werner, "The N4DP Instrument", Dissertation. TUM, Aug. 2020. [online].

[114]   G. De Geronimo, D. Christian, C. Bebek, M. Garcia-Sciveres, H. Von der Lippe, G. Haller, A. A. Grillo, and M. Newcomer, *Integrated Circuit Design in US High-Energy Physics*. July 2013. [online].

[115]   T-REX Collaboration, V. Bildstein, R. Gernhäuser, T. Kröll, R. Krücken, K. Wimmer, P. Van Duppen, M. Huyse, N. Patronis, and R. Raabe, "T-REX: A new setup for transfer experiments at REX-ISOLDE", in: *The European Physical Journal A*, vol. 48, no. 6, June 2012, p. 85. [DOI].

[116]   S. Callier, F. Dulucq, C. D. L. Taille, G. Martin-Chassard, and N. Seguin-Moreau, "SKIROC2, front end chip designed to readout the Electromagnetic CALorimeter at the ILC", in: *Journal of Instrumentation*, vol. 6, no. 12, Dec. 2011, pp. C12040–C12040. [DOI].

[117]   T. Suehara, I. Sekiya, S. Callier, V. Balagura, V. Boudry, J.-C. Brient, C. de la Taille, K. Kawagoe, A. Irles, F. Magniette, J. Nanni, R. Poeschl, T. Yoshioka, and I. S. group, "Performance study of SKIROC2/A ASIC for ILD Si-W ECAL", in: 2018. [DOI].

[118]   J. Borg, S. Callier, D. Coko, F. Dulucq, C. D. L. Taille, L. Raux, T. Sculac, and D. Thienpont, "SKIROC2_CMS an ASIC for testing CMS HGCAL", in: *Journal of Instrumentation*, vol. 12, no. 2, Feb. 2017, pp. C02019–C02019. [DOI].

[119] W. Krzemien, I. Frohlich, M. Kajetanowicz, K. Korcyl, J. Michel, M. Palka, P. Salabura, C. Schrader, P. Skott, H. Strobele, J. Stroth, A. Tarantola, M. Traxler, and R. Trebacz, *The TRB for HADES and FAIR experiments at GSI*. Nov. 2008. [online].

[120] M. Böhmer, G. Korcyl, L. Maier, J. Michel, A. Neiser, M. Palka, P. Manuel, P. Strzempek, M. Traxler, and C. Ugur, *A Users Guide to the TRB3 and FPGA-TDC Based Platforms*. Nov. 2023. [online] (visited on 02/27/2024).

[121] J. Adamczewski, H. G. Essel, N. Kurz, and S. Linev, "Data Acquisition Backbone Core DABC", in: *IEEE Transactions on Nuclear Science*, vol. 55, no. 1, 2008, pp. 251–255. [DOI].

[122] R. Brun and F. Rademakers, "ROOT — An object oriented data analysis framework", in: *Nuclear Instruments and Methods in Physics Research Section A: Accelerators, Spectrometers, Detectors and Associated Equipment*, vol. 389, no. 1, Apr. 1997, pp. 81–86. [DOI].

[123] M. Trunk, "Determination of isotope concentration profiles in materials science applications using cold neutrons", Dissertation. TUM, Jan. 2021. [online].

[124] Z. Révay, P. Kudějová, K. Kleszcz, S. Söllradl, and C. Genreith, "In-beam activation analysis facility at MLZ, Garching", in: *Nuclear Instruments and Methods in Physics Research Section A: Accelerators, Spectrometers, Detectors and Associated Equipment*, vol. 799, Nov. 2015, pp. 114–123. [DOI].

[125] R. Lutter, O. Schaile, K. Schoeffel, K. Steinberger, and C. Broude, *MARaBOU Data Acquisition*. May 2019. [online] (visited on 02/27/2024).

[126] J. Schlegel, "Tiefenprofilmessung mit gepulsten Neutronen", Bachelor Thesis. TUM, 2022.

[127] N. Moss and L. Yaffe, "Determination of the Neutron Capture Cross Section for the $Co^{59}(n,\gamma)Co^{60m}$ Reaction", in: *Canadian Journal of Chemistry*, vol. 31, no. 4, Apr. 1953, pp. 391–395. [DOI].

[128] M. Mariscotti, "A method for automatic identification of peaks in the presence of background and its application to spectrum analysis", in: *Nuclear Instruments and Methods*, vol. 50, no. 2, May 1967, pp. 309–320. [DOI].

[129] M. Morháč, J. Kliman, V. Matoušek, M. Veselský, and I. Turzo, "Identification of peaks in multidimensional coincidence γ-ray spectra", in: *Nuclear Instruments and Methods in Physics Research Section A: Accelerators, Spectrometers, Detectors and Associated Equipment*, vol. 443, no. 1, Mar. 2000, pp. 108–125. [DOI].

[130] M. E. Wall, A. Rechtsteiner, and L. M. Rocha, "Singular Value Decomposition and Principal Component Analysis", in: *A Practical Approach to Microarray Data Analysis*. Ed. by D. P. Berrar, W. Dubitzky, and M. Granzow. Kluwer Academic Publishers, 2003, pp. 91–109. [DOI].

[131] *Introduction to the Camera Obscura*. National Science and Media Museum blog. Jan. 2011. [online] (visited on 03/15/2024).

[132] *WebAtima - Energy Loss Calculator*. [online] (visited on 10/15/2024).

[133] O. Chamberlain and E. Segrè, "Proton-Proton Collisions within Lithium Nuclei", in: *Physical Review*, vol. 87, no. 1, July 1952, pp. 81–83. [DOI].

[134] V. Panin, "Fully exclusive measurements of quasi-free single-nucleon knockout reactions in inverse kinematics." PhD thesis. TU Darmstadt, Nov. 2012. 121 pp. [online].

[135] V. Panin, T. Aumann, and C. A. Bertulani, "Quasi-free scattering in inverse kinematics as a tool to unveil the structure of nuclei: A tribute to Mahir S. Hussein", in: *The European Physical Journal A*, vol. 57, no. 3, Mar. 2021, p. 103. [DOI].

[136] D. Bertini, "R3BRoot, simulation and analysis framework for the R3B experiment at FAIR", in: *Journal of Physics: Conference Series*, vol. 331, no. 3, Dec. 2011, p. 032036. [DOI].

[137] L. D. Landau, "On the energy loss of fast particles by ionization", in: vol. 8, no. 4, 1944, pp. 201–205.

[138] L. Ziegele, "Silicon Detector Characterization for the HI-TREX Experiment", Bachelor Thesis. TUM, Sept. 2023.

[139] T. Möller and B. Trumbore, "Fast, minimum storage ray/triangle intersection", in: *ACM SIGGRAPH 2005 Courses on - SIGGRAPH '05*. ACM SIGGRAPH 2005 Courses. ACM Press, 2005, p. 7. [DOI].

[140] H. Nyquist, "Certain Topics in Telegraph Transmission Theory", in: *Transactions of the American Institute of Electrical Engineers*, vol. 47, no. 2, Apr. 1928, pp. 617–644. [DOI].

[141] C. Shannon, "Communication in the Presence of Noise", in: *Proceedings of the IRE*, vol. 37, no. 1, Jan. 1949, pp. 10–21. [DOI].

[142] F. Haight, *Handbook of the Poisson Distribution*. Operations Research Society of America. Publications in operations research. Wiley, 1967. ISBN: 978-83-910144-2-4. [online].

[143] *WHO Timeline - COVID-19*. Apr. 2020. [online] (visited on 05/29/2024).

[144] F. online, *Jahresgrenzwert überschritten: Radioaktives C-14 aus Forschungsreaktor ausgetreten*. FOCUS online. [online] (visited on 05/29/2024).

[145] M. Moll, "Displacement Damage in Silicon Detectors for High Energy Physics", in: *IEEE Transactions on Nuclear Science*, vol. 65, no. 8, Aug. 2018, pp. 1561–1582. [DOI].

[146] H. Schopper and C. W. Fabjan, eds., *Detectors for particles and radiation*. Particle physics reference library / Herwig Schopper (editor) volume 2. Springer Open, 2020. 1078 pp.

[147] X. Llopart, R. Ballabriga, M. Campbell, L. Tlustos, and W. Wong, "Erratum to "Timepix, a 65 k programmable pixel readout chip for arrival time, energy and/or photon counting measurements" [Nucl. Instr. and Meth. A. 581 (2007) 485–494]", in: *Nuclear Instruments and Methods in Physics Research Section A: Accelerators, Spectrometers, Detectors and Associated Equipment*, vol. 585, no. 1, Jan. 2008, pp. 106–108. [DOI].

[148] G. Aglieri Rinella, A. Andronic, M. Antonelli, M. Aresti, R. Baccomi, P. Becht, S. Beole, J. Braach, M. D. Buckland, E. Buschmann, P. Camerini, F. Carnesecchi, L. Cecconi, E. Charbon, G. Contin, D. Dannheim, J. De Melo, W. Deng, A. Di Mauro, J. Hasenbichler, H. Hillemanns, G. H. Hong, A. Isakov, A. Junique, A. Kluge, A. Kotliarov, F. Křížek, L. Lautner, M. Mager, D. Marras, P. Martinengo, S. Masciocchi, M. W. Menzel, M. Munker, F. Piro, A. Rachevski, K. Rebane, F. Reidt, R. Russo, I. Sanna, V. Sarritzu, S. Senyukov, W. Snoeys, J. Sonneveld, M. Šuljić, P. Svihra, N. Tiltmann, G. Usai, J. B. Van Beelen, M. D. Vassilev, C. Vernieri, and A. Villani, "Digital pixel test structures implemented in a 65 nm CMOS process", in: *Nuclear Instruments and Methods in Physics Research Section A: Accelerators, Spectrometers, Detectors and Associated Equipment*, vol. 1056, Nov. 2023, p. 168589. [DOI].

[149] G. A. Rinella, G. Alocco, M. Antonelli, R. Baccomi, S. M. Beole, M. B. Blidaru, B. B. Buttwill, E. Buschmann, P. Camerini, F. Carnesecchi, M. Chartier, Y. Choi, M. Colocci, G. Contin, D. Dannheim, D. De Gruttola, M. D. R. Viera, A. Dubla, A. di Mauro, M. C. Donner, G. H. Eberwein, J. Egger, L. Fabbietti, F. Feindt, K. Gautam, R. Gernhaeuser, J. J. Glover, L. Gonella, K. G. Grodaas, I.-M. Gregor, H. Hillemanns, L. Huth, A. Ilg, A. Isakov, D. M. Jones, A. Junique, J. Kaewjai, M. Keil, J. Kim, A. Kluge, C. Kobdaj, A. Kotliarov, K. Kittimanapun, F. Křížek, G. Kucharska, S. Kushpil, P. La Rocca, N. Laojamnongwong, L. Lautner, R. C. Lemmon, C. Lemoine, L. Li, F. Librizzi, J. Liu, A. Macchiolo, M. Mager, D. Marras, P. Martinengo, S. Masciocchi, S. Mattiazzo, M. W. Menzel, A. Mulliri, M. R. Mylne, F. Piro, A. Rachevski, M. Rasà, K. Rebane, F. Reidt, R. Ricci, S. R. Daza, G. Saccà, I. Sanna, V. Sarritzu, J. Schlaadt, D. Schledewitz, G. Scioli, S. Senyukov, A. Simancas, W. Snoeys, S. Spannagel, M. Šuljić, A. Sturniolo, N. Tiltmann, A. Trifirò, G. Usai, T. Vanat, J. B. Van Beelen, L. Varga, M. Verdoglia, G. Vignola, A. Villani, H. Wennloef, J. Witte, and R. B. Wittwer, *Characterisation of analogue Monolithic Active Pixel Sensor test structures implemented in a 65 nm CMOS imaging process*. Mar. 2024. [online].

[150] R. H. Dicke, "Scatter-Hole Cameras for X-Rays and Gamma Rays", in: *The Astrophysical Journal*, vol. 153, Aug. 1968, p. L101. [DOI].

[151] J. G. Ables, "Fourier Transform Photography: A New Method for X-Ray Astronomy", in: *Publications of the Astronomical Society of Australia*, vol. 1, no. 4, Dec. 1968, pp. 172–173. [DOI].

[152] E. E. Fenimore and T. M. Cannon, "Coded aperture imaging with uniformly redundant arrays", in: *Applied Optics*, vol. 17, no. 3, Feb. 1978, p. 337. [DOI].

[153] E. E. Fenimore, "Coded aperture imaging: predicted performance of uniformly redundant arrays", in: *Applied Optics*, vol. 17, no. 22, Nov. 1978, p. 3562. [DOI].

[154] S. R. Gottesman and E. E. Fenimore, "New family of binary arrays for coded aperture imaging", in: *Applied Optics*, vol. 28, no. 20, Oct. 1989, p. 4344. [DOI].

[155] E. Caroli, J. B. Stephen, G. Di Cocco, L. Natalucci, and A. Spizzichino, "Coded aperture imaging in X- and gamma-ray astronomy", in: *Space Science Reviews*, vol. 45, no. 3, Sept. 1987, pp. 349–403. [DOI].

[156] G. K. Skinner, *Coded-Mask Imaging in Gamma-Ray Astronomy - Separating the Real and Imaginary parts of a Complex subject*. Feb. 2003. [online].

[157] L. Zhang and R. Lanza, "CAFNA/sup (R)/, coded aperture fast neutron analysis for contraband detection: preliminary results", in: *IEEE Transactions on Nuclear Science*, vol. 46, no. 6, Dec. 1999, pp. 1913–1915. [DOI].

[158] R. Accorsi, "Coded aperture Fast Neutron Analysis: Latest design advances", in: *AIP Conference Proceedings*. The CAARI 2000: Sixteenth international conference on the application of accelerators in research and industry. Vol. 576, AIP, 2001, pp. 491–494. [DOI].

[159] C. A. Barrera, E. C. Morse, and M. J. Moran, "Image reconstruction algorithms for inertial confinement fusion neutron imaging", in: *Review of Scientific Instruments*, vol. 77, no. 10, Oct. 2006, 10E716. [DOI].

[160] A. Talebitaher, P. M. Shutler, S. V. Springham, R. S. Rawat, and P. Lee, "Coded aperture imaging of alpha source spatial distribution", in: *Radiation Measurements*, vol. 47, no. 10, Oct. 2012, pp. 992–999. [DOI].

[161] S. Bahmani and J. Romberg, "Compressive Deconvolution in Random Mask Imaging", in: *IEEE Transactions on Computational Imaging*, vol. 1, no. 4, Dec. 2015, pp. 236–246. [DOI].

[162] J. P. Roques, "Fast decoding algorithm for uniformly redundant arrays", in: *Applied Optics*, vol. 26, no. 18, Sept. 1987, p. 3862. [DOI].

[163] O. Lévêque, C. Kulcsár, and F. Goudail, "Comparison of linear and nonlinear deconvolution algorithms for co-optimization of depth-of-field enhancing binary phase masks", in: *OSA Continuum*, vol. 4, no. 2, Feb. 2021, p. 589. [DOI].

[164] S. Elmalem, R. Giryes, and E. Marom, "Learned phase coded aperture for the benefit of depth of field extension", in: *Optics Express*, vol. 26, no. 12, June 2018, p. 15316. [DOI].

Acknowledgments

In this very last part of my thesis, I would like to express my sincere gratitude to those who have helped and supported me throughout this work. For me, personally, gratitude is not the naive positivity often expected by society but rather the act of acknowledging what or who sustains us, no matter how difficult or hard the situation may seem to be. *Gratitude is the process of consciously and courageously attempting thankfulness in the face of the catastrophe of life.* - Dr. Jordan B. Peterson.

First and foremost, I would like to sincerely thank my doctoral supervisor, Prof. Dr. Bastian Märkisch, for giving me the opportunity to continue and complete the N4DP project in times of uncertainty. Bastian is not only an exceptional physicist and lecturer (I very much enjoyed being next to him as a moderator during his lectures), but also someone who deeply understands the importance of family. He supported me in difficult times and helped me with valuable ideas, while his confidence in my abilities led to the successful completion of this work.

To my supervisor, Dr. Roman Gernhäuser, I would like to thank him just as much for his amazing board drawings, great ideas, and remarkable expertise not only in electronics and physics but in general. His support at different times during my thesis was more than invaluable. Despite managing several groups at the same time, he made time for each to not only succeed but also learn as much as possible. I particularly remember our beamtime in the Netherlands when, even though he couldn't be there in person, he made the effort to call and guide us with his advice and ideas.

With at least as much importance, I would like to thank Sergei Golenev, a doctorate candidate for whom I am grateful to have as a working colleague and as a good friend. Throughout the years, not only did we form a complementary working team but also a good friendship based on belief in an almighty cat god. Sergei is a hardworking person that one can rely on. Whenever I got late-night (past midnight) pictures, I always knew he had some kind of breakthrough. Sergei was always helpful with coding ideas and always had great questions, which led to some sort of advancement. Together, we had a great time at different beam times, and I will never forget it.

I would like to thank the ENE group under my professor, with whom I had the pleasure of spending more time toward the end of my work. I very much enjoyed our grilling sessions and amazing discussions. Special thanks to Karina Bernert for proofreading parts of my thesis and for the conversations we had in the office.

Another group I had the privilege of being involved with throughout my thesis was that of Prof. Dr. Laura Fabbietti. She welcomed me into her amazing group and even allowed me to join a summer school in her hometown in Italy, where I learned about exciting and exotic physics topics. She and her group make valuable and positive contributions to the physics community, and I am very grateful for that. A special thanks goes to Berkin Ulukutlu, who helped me with the image on the cover, who was an amazing lab colleague, and someone with whom I had a nice time in Krakow.

Although their contributions preceded my work, Dr. Markus Trunk, Dr. Lukas Werner,